THE BELL SYSTEM
TECHNICAL JOURNAL

DEVOTED TO THE SCIENTIFIC AND ENGINEERING
ASPECTS OF ELECTRICAL COMMUNICATION

Volume 58 May–June 1979 Number 5

On the Independence Theory of Equalizer Convergence

By J. E. MAZO

(Manuscript received December 18, 1978)

High-speed pulse amplitude modulated (PAM) data transmission over telephone channels is only possible when adaptive equalization is used to mitigate the linear distortion found on the (initially unknown) channel. At the beginning of the equalization procedure, the tap weights are adjusted to minimize the intersymbol interference between pulses. The "stochastic gradient" algorithm is an iterative procedure commonly used for setting the coefficients in these and other adaptive filters, but a proper understanding of the convergence has never been obtained. It has been common analytical practice to invoke an assumption stating that a certain sequence of random vectors which direct the "hunting" of the equalizer are statistically independent. Everyone acknowledges this assumption to be far from true, just as everyone agrees that the final predictions made using it are in excellent agreement with experiments and simulations. We take the resolution of this question as our main problem. When one begins to analyze the performance of the algorithm, one sees that the average mean-square error after the nth iteration requires knowing, as an intermediate step, the mathematical expectation of the product of a sequence of statistically dependent matrices. We transform the latter problem to a space of sufficiently high dimension where the required average may be obtained from a canonical equation $\mathscr{V}_{n+1} = \mathscr{A}(\alpha)\mathscr{V}_n + \mathscr{F}$*. Here* $\mathscr{A}(\alpha)$ *is a square matrix, depending on the "step-size"* α *of the original algorithm, and* $\mathscr{V}_n$ *and* $\mathscr{F}$ *are vectors. The mean-square error is calculable from the solution* $\mathscr{V}_n$*.*

Information about the solution of our equation is obtained by doing *matrix perturbation theory on* $\mathscr{A}(\alpha)$ *for small values of* α*. We show that the first two terms of the perturbation solution contain, among their terms, the terms of the independence theory. Since the parameter* α *needs to be small even for independence theory to converge, agreement with an exact theory and experiment is obtained if, in some sense, the additional terms which appear in the perturbation solution may be disregarded. This will usually be the case.*

I. INTRODUCTION

Adaptive equalization of telephone channels in order to facilitate high-speed data transmission has been successful ever since its introduction by Lucky in the 1960s. This technique uses a linear filter (configured as a tapped delay line) to remove the harmful effects of the linear channel distortion. At the start of the equalization procedure, a set of parameters, the tap weights, are adjusted so that the final setting of these taps minimizes the intersymbol interference between pulses in the data train. Many theoretical studies have been made concerning steady-state equalization after the optimum tap weights have been achieved; little analysis has been done concerning the convergence of the equalizer tap weights to their final settings. Even in the best published study on this problem (Ungerboeck, Ref. 1), it is necessary to invoke an assumption stating that a sequence of random vectors which direct the operation of the equalizer are statistically independent.† This independence assumption will be explained more fully later; for the moment, we only indicate that it is not even approximately true. In fact, given the nth vector of the sequence, all but one component of the next vector will be exactly known. Yet if this assumption is made, surprising agreement with actual performance is obtained.[1] Clearly, because of its importance, this situation begs for clarification. Hopefully, what we learn in equalization can be used for other applications where similar adaptive algorithms are used. In particular, the areas of linear prediction and adaptive array processing, both electromagnetic and sonar, come to mind. We concentrate our presentation on equalization, however, for here the author is sure of the details.

We shall take as our performance criterion the expected value of the mean-square distortion, although the average error vector is also considered as a simpler problem. In particular, then, we are not concerned with the fluctuations which might occur in actual use.

---

† We are here concerned with convergence in random data, not with a known specially designed sequence. In usual startup operation, the data symbols are also assumed known, either by using a known sequence or by assuming that sufficiently accurate estimates are available.

Typically, the sample paths are close to the mean (see Ref. 1). In a nutshell, our contribution to this problem consists of two parts. We first establish a time-independent difference equation which governs the average in question. This step is accomplished in a space of much higher dimension than one would initially assume. Second, examining the solution of this equation in a perturbation sense (the small "step-size" of the algorithm being the essential perturbation parameter), we find the leading terms contain the independence theory solution.

Before delving into the abstract problem, we devote Section II to describing some more conventional aspects of data transmission and equalization and Section III to discussing the behavior of the mean-square error if the independence assumption is made.

II. DATA TRANSMISSION AND EQUALIZATION

For our own convenience, we confine the discussion to binary baseband transmission and neglect the effects of additive noise.

The equalizer, and in fact the entire detection procedure, operates on the samples of the baseband received signal $r(t)$, where

$$r(t) = \sum_m a_{m+K} h(t - mT).$$

If $1/T'$ is the sampling rate, $1/T$ the symbol rate, a_n the data symbols (iid, ± 1 with equal probability) and $h(t)$ the overall system impulse response, then these samples are†

$$r(nT') = \sum_{m=-\infty}^{\infty} a_{m+K} h(nT' - mT) \qquad n = 0, 1, 2 \cdots . \tag{1}$$

For a synchronous equalizer, $T' = T$ and for a fractionally spaced equalizer, typically $T' = T/2$. If the coefficients of the equalizer are denoted by c_i, $i = 1, \cdots, N$ (c_i being also the ith component of a vector $\mathbf{c}$) and the sequence of output samples of the equalizer are y_n, then

$$y_n = \sum_{s=1}^{N} c_s r[(s-1)T' + nT] \qquad n = 0, 1, 2, \cdots . \tag{2}$$

We call attention to the fact that, even when $T' \neq T$, the equalizer samples are only of interest at multiples of the signaling interval T, and the notation of (2) takes this into account. We define a sequence (in time) of vectors $\mathbf{X}^{(n)}$ such that the sth component of vector $\mathbf{X}^{(n)}$ is

$$X_s^{(n)} = r[(s-1)T' + nT] \qquad \begin{array}{l} s = 1, 2, \cdots, N \\ n = 0, 1, 2, \cdots , \end{array} \tag{3}$$

---

† We call the bit which "goes with" the mth pulse a_{m+K} (instead of the usual a_m) for later convenience.

and thus

$$y_n = \mathbf{c} \cdot \mathbf{X}^{(n)}. \tag{4}$$

The implementation of (2) to (4) is shown in Fig. 1.

Later, when we consider an adaptive equalizer, the taps will vary with time and $\mathbf{c}^{(n)}$ will be used for the sequence of tap-weight vectors. Ideally we would like (at least when n is large enough) the sequence of equalizer outputs to be the sequence of data symbols, except, perhaps, for a shift. For a finite equalizer (i.e., N finite) this ideal is not achievable, and instead the available taps are adjusted to minimize the average square error Ee_n^2, where

$$e_n = y_n - a_{n+K} \tag{5}$$

and E denotes the mathematical expectation with respect to the data symbols $\{a_n\}$. If one introduces the $N \times N$ channel autocorrelation matrix† (which is positive definite),

$$A = E\mathbf{X}^{(n)}\mathbf{X}^{(n)T}, \tag{6}$$

and the vector,

$$\mathbf{v} \doteq Ea_{n+K}\mathbf{X}^{(n)}, \tag{7}$$

both of which do not depend on the time index n, then, for fixed taps $\mathbf{c}$, the mean-squared error $\mathscr{E}$ is given by

$$\mathscr{E} \equiv E(y_n - a_{n+K})^2 = \mathbf{c}^T A\mathbf{c} - 2\mathbf{c}^T\mathbf{v} + 1. \tag{8}$$

Equation (8) shows $\mathscr{E}$ to be a convex quadratic function of $\mathbf{c}$. Any optimum choice of $\mathbf{c}$, say, $\mathbf{c}^*$, satisfies

$$A\mathbf{c}^* = \mathbf{v} \tag{9}$$

which has a unique solution if A^{-1} exists. We denote the minimum of $\mathscr{E}$ by $\mathscr{E}^*$.

It will make little difference physically, and it will be a great convenience mathematically, if we pretend that the impulse response $h(t)$ used in (1) has finite duration. Thus, assume

$$h(t) = 0 \quad \text{if} \quad |t| > HT.$$

Let N_1 and N_2 be the largest integers such that

$$N_1T \leq HT \tag{10a}$$

$$(N-1)T' - N_2T \geq -HT. \tag{10b}$$

Further, choose the integer K in (1) to be N_1 and set $M = N_1 + N_2 + 1$, and let $\mathbf{a}^{(n)}$ be an M-dimensional vector whose ith component is

---

† The superscript T always denotes transpose.

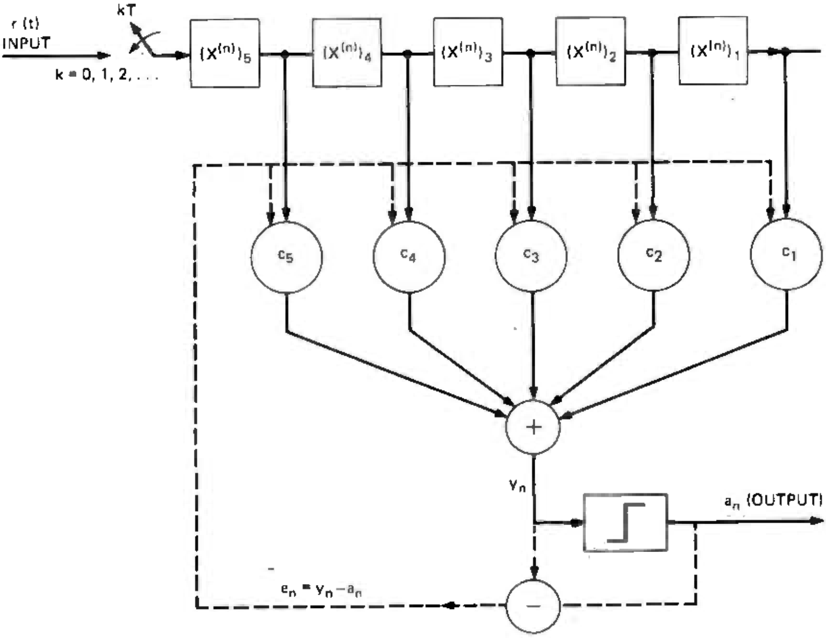

Fig. 1—Adaptive transversal equalizer, $N = 5$.

$\mathbf{a}_i^{(n)} = a_{n+i-1}$, $i = 1, \cdots, M$. Then using (3) and (1) we have

$$\mathbf{X}^{(n)} = B\mathbf{a}^{(n)}, \tag{11}$$

where in (11) B is an $N \times M$ matrix having elements

$$B_{ij} = h[(i-1)T' + (N_1 + 1 - j)T], \quad \begin{matrix} 1 \le i \le N, \\ \\ 1 \le j \le M. \end{matrix} \tag{12}$$

It follows from (10b) that $M \ge N$ if $T' = T$ and $M > (N+1)/2$ if $T' = T/2$.

The structure of the matrix B is illustrated below for the special case $T' = T$, $N = 3$, $M = 7$.

$$B = \begin{bmatrix} h_2 & h_1 & h_0 & h_{-1} & h_{-2} & 0 & 0 \\ 0 & h_2 & h_1 & h_0 & h_{-1} & h_{-2} & 0 \\ 0 & 0 & h_2 & h_1 & h_0 & h_{-1} & h_{-2} \end{bmatrix}.$$

This structure means that $\mathbf{X}^{(n)}$ has the same shifting property as $\mathbf{a}^{(n)}$. Thus, for example, in time sequence,

$$\begin{bmatrix} a \\ b \\ c \end{bmatrix} \rightarrow \begin{bmatrix} b \\ c \\ d \end{bmatrix} \rightarrow \begin{bmatrix} c \\ d \\ e \end{bmatrix}, \quad \text{etc.}$$

Since

$$E\mathbf{a}^{(n)}\mathbf{a}^{(n)T} = I, \tag{13}$$

it follows from (6), (11), and (13) that

$$A = E\mathbf{X}^{(n)}\mathbf{X}^{(n)T} = BB^T. \tag{14}$$

For the special case $T' = T$, $h(nT) = \delta_{n0}$, then $M = N$, $A = I$, and

$$\mathbf{X}^{(n)} = \mathbf{a}^{(n)} = \begin{bmatrix} a_n \\ \cdot \\ \cdot \\ \cdot \\ \cdot \\ a_{n+N-1} \end{bmatrix}. \tag{15}$$

We now begin to describe the stochastic gradient algorithm used for equalizer convergence. But first we describe a different problem, the *deterministic* gradient algorithm, which is a method for finding the minimum on the surface $\mathscr{S}$, where

$$\mathscr{S} = \mathbf{c}^T A\mathbf{c} - 2\mathbf{c}^T\mathbf{v} + 1. \tag{16}$$

This provides some heuristics for writing down the stochastic algorithm, but should not be confused with it. We take pains to point out some differences as we proceed, since many people substitute discussion of this algorithm for the actual one.

Taking the gradient of (16) gives

$$\nabla\mathscr{S} = 2[A\mathbf{c} - \mathbf{v}]. \tag{17}$$

Hence, if we were searching for a minimum of the function (16) by taking steps in the gradient direction, we would write the following equation for our position $\mathbf{c}^{(n)}$ at the nth stage

$$\mathbf{c}^{(n+1)} = \mathbf{c}^{(n)} - \Delta(A\mathbf{c}^{(n)} - \mathbf{v}), \tag{18}$$

Δ being a step-size parameter. Equation (18) coupled with (6) and (7) motivates the actual stochastic gradient algorithm used, namely,

$$\mathbf{c}^{(n+1)} = \mathbf{c}^{(n)} - \alpha[\mathbf{X}^{(n)}(\mathbf{X}^{(n)T}\mathbf{c}^{(n)}) - a_{n+K}\mathbf{X}^{(n)}] \tag{19}$$

$$= \mathbf{c}^{(n)} - \alpha e_n \mathbf{X}^n, \tag{20}$$

e_n being the scalar error (5), and α the step-size†. Thus in N-dimensional tap space we move in directions $\mathbf{X}^{(n)}$, where $\mathbf{X}^{(n)}$ is [see (4)] the vector of values stored in the equalizer at time nT. Clearly, the allowed

---

† It is, of course, meaningless to speak of the "size" of α unless one fixes the size or scaling of the terms which multiply it in (20). We shall take the scaling of the latter so that, in the binary case, the matrix A [see (6)] has largest eigenvalue unity.

set of directions along which we "step" is, as (15) will testify, quite random and cannot be thought of as being gradient directions. Nevertheless, tradition dominates, and (19) and (20) are still referred to as a stochastic gradient algorithm.

For our purposes, (19) may be rewritten slightly by introducing the error vector

$$\boldsymbol{\epsilon}^{(n)} = \mathbf{c}^{(n)} - \mathbf{c}^*. \tag{21}$$

Subtracting $\mathbf{c}^*$ from both sides of (19) allows us to write

$$\boldsymbol{\epsilon}^{(n+1)} = (I - \alpha \mathbf{X}^{(n)}\mathbf{X}^{(n)T})\boldsymbol{\epsilon}^{(n)} - \alpha(\mathbf{c}^{*T}\mathbf{X}^{(n)} - a_{n+K})\mathbf{X}^{(n)}. \tag{22}$$

Note the quantity $\mathbf{c}^{*T}\mathbf{X}^{(n)} - a_{n+K}$ is the instantaneous error if the optimum taps were used. This is normally quite small and would be zero if perfect equalization were possible.

In terms of the $\boldsymbol{\epsilon}^{(n)}$, the mean-square error is

$$\mathscr{E}^{(n)} = \mathscr{E}^* + \boldsymbol{\epsilon}^{(n)T}A\boldsymbol{\alpha}^{(n)} \equiv \mathscr{E}^* + \mathscr{E}_{ex}^{(n)}. \tag{23}$$

In (23) the symbol $\mathscr{E}_{ex}^{(n)}$ has been introduced for the excess mean-square error over $\mathscr{E}^*$.

In (22) and (23), $\boldsymbol{\epsilon}^{(n)}$ is random, and in fact depends on the entire sequence of data symbols since the adaptation began. Our measure of the progress of the algorithm will be $E\mathscr{E}^{(n)}$, the average of the error at time n over all data sequences.

III. THE INDEPENDENCE THEORY

In this section we describe "independence theory," an approximation used to mathematically treat the stochastic gradient algorithm described by (22). Use of the approximation allows one (as we shall see) to determine bounds on the step-size α which will ensure stability and allows calculations to be made on convergence rates.

Independence theory treats the stochastic algorithm by assuming that the sequence $\mathbf{X}^{(n)}$ are statistically independent vectors. Since, from (22), $\boldsymbol{\epsilon}^{(n)}$ depends only on the sequence $\mathbf{X}^{(1)}, \cdots, \mathbf{X}^{(n-1)}$ (assuming we start with $\mathbf{X}^{(1)}$), we conclude $\epsilon^{(n)}$ and $\mathbf{X}^{(n)}$ are independent. For an example as to how this is applied, we look at the average error vector $E\boldsymbol{\epsilon}^{(n)}$. We have, from (22), (6), (7), and (9),

$$E\boldsymbol{\epsilon}^{(n+1)} = (I - \alpha A)E\boldsymbol{\epsilon}^{(n)}. \tag{24}$$

If, for comparison, we introduce the error vector $\mathbf{c}_n - \mathbf{c}^*$ for the *deterministic* theory and call it $d^{(n)}$ so no confusion can arise, we would have, subtracting $\mathbf{c}^*$ from both sides of (18),

$$\mathbf{d}^{(n+1)} = (I - \Delta A)\mathbf{d}^{(n)}. \tag{25}$$

There is no question of an average in (25); $d^{(n)}$ is the error. In (24), $E\epsilon^{(n)}$ can be zero although the norm of $\epsilon^{(n)}$ can be quite large.

To emphasize the difference further, let us return to the simple model (15) which describes an undistorted channel, for which perfect equalization is possible. Only the initial setting of the taps is wrong. For this case, we have [note $A = I$ in (23)] using (22) and the independence assumption

$$\begin{aligned} E\epsilon^{(n+1)T}\epsilon^{(n+1)} &= \epsilon^{(n)T}(I - \alpha \mathbf{X}^{n}\mathbf{X}^{(n)T})(I - \alpha \mathbf{X}^{(n)}\mathbf{X}^{(n)T})\epsilon^{(n)} \\ &= (1 - 2\alpha + \alpha^2 N)\epsilon^{(n)T}\epsilon^{(n)}. \end{aligned} \tag{26}$$

Thus the error decays to zero as

$$(1 - 2\alpha + \alpha^2 N)^n \mathscr{E}^{(0)}, \tag{27}$$

which is optimized if $\alpha = 1/N$ to give

$$\left(1 - \frac{1}{N}\right)^n \mathscr{E}^{(0)}. \tag{28}$$

Note how convergence is slowed as the number of taps N of the problem increases. By contrast, if $A = I$ in (25), choosing $\Delta = 1$ gives convergence in one step, independent of dimension.

The convergence range of (24) for $A = I$ is $0 < \alpha < 2$, while for (27) it is $0 < \alpha < 2/N$. In practice, N ranges from about 7 to 64 and thus α is, by the requirement of convergence of the mean-square error, kept quite small.

In order to examine independence theory further, it will be convenient to discuss the (positive definite) error matrix

$$R^{(n)} = E\epsilon^{(n)}\epsilon^{(n)T}. \tag{29}$$

All the information we wish about $E\mathscr{E}_{ex}^{(n)}$, the average excess mean-square error, is contained in (29). Thus, from (23)

$$\begin{aligned} E\mathscr{E}_{ex}^{(n)} = E\epsilon^{(n)T}A\epsilon^{(n)} &= \sum_{i,j} (a)_{ij}(E\epsilon^{(n)}\epsilon^{(n)T})_{ji} \\ &= \operatorname{tr} AR^{(n)}. \end{aligned} \tag{30}$$

Similarly, the average norm $E\|\epsilon^{(n)}\|^2 = \operatorname{tr} R^{(n)}$.

Our procedure for writing an equation for the time evolution of $R^{(n)}$ is simply to write the definition of $R^{(n+1)}$ using (29), substitute (22) for $\epsilon^{(n+1)}$, and do the average using the independence assumption. Various cross terms arise, and the computations naturally fall into three steps:

Step 1:

$$\begin{aligned} &E[I - \alpha \mathbf{X}^{(n)}\mathbf{X}^{(n)T}]\epsilon^{(n)}\epsilon^{(n)T}[I - \alpha \mathbf{X}^{(n)}\mathbf{X}^{(n)T}] \\ &\quad = R^{(n)} - \alpha[AR^{(n)} + R^{(n)}A] + \alpha^2 E[\mathbf{X}^{(n)}\mathbf{X}^{(n)T}R^{(n)}\mathbf{X}^{(n)}\mathbf{X}^{(n)T}]. \end{aligned} \tag{31}$$

Appendix A discusses the evaluation of the last term. For simplicity, we approximate the exact evaluation by $\alpha^2 A \operatorname{tr} AR^{(n)}$. When $A = I$, we have $\operatorname{tr}[\alpha^2 A \operatorname{tr} AR^{(n)}] = \alpha^2 N \mathscr{E}_{ex}^{(n)}$, so in general this term plays the role of the $\alpha^2 N$ term in (26).

Step 2:

$$E\alpha[I - \alpha \mathbf{X}^{(n)}\mathbf{X}^{(n)T}]\boldsymbol{\epsilon}^{(n)}\mathbf{X}^{(n)T}(\mathbf{c}^{*T}\mathbf{X}^{(n)} - a_{n+K}). \tag{32}$$

This is considered further in Appendix A and, for reasons given there, is approximated by zero.

Step 3: As discussed in Appendix A,

$$E\alpha^2(\mathbf{c}^{*T}\mathbf{X}^{(n)} - a_{n+K})\mathbf{X}^{(n)}\mathbf{X}^{(n)T}(\mathbf{c}^{*T}\mathbf{X}^{(n)} - a_{n+K}) \approx \alpha^2 \mathscr{E}^* A. \tag{33}$$

Putting together these three steps, we have the following accurate approximation from independence theory:

$$R^{(n+1)} = R^{(n)} - \alpha[AR^{(n)} + R^{(n)}A] + \alpha^2 A \operatorname{tr} AR_n^{(n)} + \alpha^2 \mathscr{E}^* A. \tag{34}$$

Note that the last term prevents $R^{(n)} = 0$ from being a solution. Thus, $R^{(n)}$ is prevented from going to zero by the small forcing term. Thus, in particular, $\boldsymbol{\epsilon}^{(n)}$ only approaches zero but then executes small fluctuations about zero.

Since (34) is an approximation, we prove in Appendix B that the positive definite character of $R^{(n)}$ is preserved in (34).

We now introduce a more useful form of (34) when the mean-square error is of primary interest. Since A is hermitian, let U be the unitary transformation which diagonalizes A,

$$U^+ A U = D, \tag{35}$$

where we call the elements of the diagonal matrix D, by d_i. Further, let

$$U^+ R^{(n)} U = T^{(n)}. \tag{36}$$

In general, $T^{(n)}$ is not diagonal, but set $T_{ii}^{(n)} = t_i^{(n)}$. Further, note

$$\mathscr{E}_{ex}^{(n)} = \operatorname{tr} AR^{(n)} = \operatorname{tr} DT^{(n)} = \sum_{i=1}^{N} d_i t_i^{(n)}. \tag{37}$$

It follows from (34), (35), and (36) that

$$T^{(n+1)} = T^{(n)} - \alpha[DT^{(n)} + T^{(n)}D] + \alpha^2 D \operatorname{tr} DT^{(n)} + \alpha^2 \mathscr{E}^* D. \tag{38}$$

Noting from (37) that the mean-square error depends only on the $t_i^{(n)}$, we are motivated to look at the diagonal terms of (38). Happily, they decouple from the off-diagonal terms and we have

$$t_i^{(n+1)} = t_i^{(n)} - 2\alpha d_i t_i^{(n)} + \alpha^2 d_i \sum_{j=1}^{n} d_j t_j^{(n)} + \alpha^2 \mathscr{E}^* d_i. \tag{39}$$

If we introduce *vectors* $\mathbf{t}^{(n)}$ and $\mathbf{d}$ in the obvious way, (39) itself can be rewritten in matrix notation as

$$\mathbf{t}^{(n+1)} = M\mathbf{t}^{(n)} + \alpha^2\mathcal{E}^*\mathbf{d}, \tag{40}$$

where the $N \times N$ matrix M has elements

$$M_{ij} = (1 - 2\alpha d_i)\delta_{ij} + \alpha^2 d_i d_j. \tag{41}$$

From (41) we note M is real and symmetric and thus has real eigenvalues.

The solutions to (40) will be stable if and only if the matrix M has all eigenvalues λ_i such that $-1 \le \lambda_i \le 1$. Let g be an eigenvector of M with eigenvalue λ. Then

$$M\mathbf{g} = \lambda\mathbf{g} \tag{42}$$

reads

$$g_i - 2\alpha d_i g_i + \alpha^2\Big(\sum_j d_j g_j\Big) d_i = \lambda g_i$$

or

$$g_i = -\alpha^2\Big(\sum d_i g_j\Big)\frac{d_i}{1 - \lambda - 2\alpha d_i}, \tag{43}$$

g_i denoting the components of $\mathbf{g}$.

In (41) we see that, whenever $d_i = 0$, there is a $\lambda = 1$ for all α. The eigenvector has $g_i = 1$ and $g_j = 0$, $j \ne i$. These eigenvalues do not change with α and are not of interest here. Set $\tilde{d}_i = d_i$ if $d_i \ne 0$. Then we are concerned with

$$\tilde{M}_{ij} = (1 - 2\alpha\tilde{d}_i)\delta_{ij} + \alpha^2\tilde{d}_i\tilde{d}_j \tag{44}$$

in a space of appropriately reduced dimension $\tilde{N}$. For α small enough, the eigenvalues are approximately $1 - 2\alpha\tilde{d}_i < 1$ ($\alpha > 0$, of course). Now increase α until possibly one of the eigenvalues becomes ±1. What is the critical value of α? Since all elements of (44) are strictly positive (except at most $\tilde{N}$ values of α), the magnitude of the largest eigenvalue may be taken to be associated with a positive eigenvalue.[2] Thus, in (43) [reinterpreted to match (44)], set $\lambda = 1$, multiply by d_i, and sum on i. We then obtain

$$\alpha_{crit} = \frac{2}{\sum \tilde{d}_i} = \frac{2}{\sum d_i}. \tag{45}$$

Thus, independence theory predicts a stable algorithm if

$$0 < \alpha < \frac{2}{\sum d_i} = \frac{2}{N\bar{d}}, \tag{46}$$

$\bar{d}$ being the average eigenvalue of the channel correlation matrix A.

The excess error $\mathscr{E}_{ex}^{(\infty)}$ after adaptation may be derived from (39) using (37). We get

$$\mathscr{E}_{ex}^{(\infty)} = \alpha \mathscr{E}^{*} \frac{\sum d_i}{2 - \alpha \sum d_i}. \tag{47}$$

The above discussion should provide the reader with an idea of what we hope to justify and why. The independence assumption, if it leads to valid results, provides a very workable theory for gaining insights about, and doing calculations on, the convergence procedure.

IV. AN EXACT DESCRIPTION

In this section, we put forth an exact description of how, in principle, the average mean-square error may be obtained. We begin, however, with the average error vector $E\boldsymbol{\epsilon}^{(n)}$, a simpler quantity, but one which requires essentially the same treatment. The exact dynamics of $\boldsymbol{\epsilon}^{(n)}$ is given in (22), and the independence theory for $E\boldsymbol{\epsilon}^{(n)}$ is given by (24).

For simplicity, we rename the terms in (22)

$$(I - \alpha \mathbf{X}^{(n)} \mathbf{X}^{(n)T}) \boldsymbol{\epsilon}^{(n)} \equiv P_n \boldsymbol{\epsilon}^{(n)} \tag{48}$$

and

$$-\alpha(\mathbf{c}^{*T} \mathbf{X}^{(n)} - a_{n+K}) \mathbf{X}^{(n)} \equiv \mathbf{f}^{(n)}, \tag{49}$$

so (22) reads

$$\epsilon^{(n+1)} = P_n \boldsymbol{\epsilon}^{(n)} + f^{(n)}, \tag{50}$$

which, by iteration starting with a fixed error vector $\boldsymbol{\epsilon}^{(0)}$, has the solution

$$\boldsymbol{\epsilon}^{(n+1)} = \prod_{i=0}^{n} P_i \boldsymbol{\epsilon}^{(0)} + \sum_{s=0}^{n-1} \left(\prod_{i=s+1}^{n} P_i \right) \mathbf{f}^{(s)} + \mathbf{f}^{(n)}. \tag{51}$$

Note in (51) the matrices P_i do not commute so that a product $\prod_1^n P_i$ means in the order $P_n \cdots P_2 P_1$.

We proceed to examine (51) in more detail. We remark first that, by their very definition, P_n and $\mathbf{f}^{(n)}$ depend on the data variables $\{a_n, a_{n+1}, \cdots, a_{n+M-1}\}$ [see (11), (15), (48), (45)], and thus $\boldsymbol{\epsilon}^{(n+1)}$ depends on the entire sequence $\{a_i\}_{i=0}^{n+M-1}$. If we formally average (51) making use of the stationarity of the basic Bernoulli sequence $\{a_i\}$, we have

$$E\boldsymbol{\epsilon}^{(n+1)} = \left(E \prod_{i=0}^{n} P_i \right) \boldsymbol{\epsilon}^{(0)} + \sum_{s=1}^{n} \left(E \prod_{i=1}^{s} P_i \mathbf{f}^{(0)} \right), \tag{52}$$

the expectation being taken over all binary variables which enter (52), namely, $a_0, a_1, \cdots, a_{n+M-1}$. The first term of (52) represents the decay of the initial error to zero (the transient); the second term is the forced response, causing a small but nonzero steady state error as $n \to \infty$.

We have not been able to work with (52) directly, and at this point our analysis takes a crucial turn. We average (51) again, only this time we do not average over all the binary variables which enter but only over the sequence $a_0, a_1, \cdots, a_n$. Call this conditioned average E_n. Then

$$E_n\epsilon^{(n+1)} = \left(E_n \prod_{i=0}^{n} P_i\right)\epsilon^{(0)} + \sum_{s=0}^{n-1}\left(E_n \prod_{i=s+1}^{n} P_i f^{(s)}\right) + E_n\mathbf{f}^{(n)}. \tag{53}$$

Now, however, (53) is not one vector equation but 2^{M-1} of them, since it is valid for any sequence of values of $\{a_{n+1}, \cdots, a_{n+M-1}\}$; these variables appear in (53) for arbitrary values. Thus the set of values just mentioned form a "super-index" which we may collectively call J, J taking 2^{M-1} values. For example, we might choose to call (for $M = 3$) the values $\{+1, +1\}$ to be $J = 1$, $\{+1, -1\}$ to be $J = 2$, $\{-1, +1\}$ to be $J = 3$, and $\{-1, -1\}$ to be $J = 4$. For the moment, however, the precise mapping from the $(M - 1)$ binary variables to the integer J is unimportant.

We also want to consider the matrix

$$P_n = I - \alpha\mathbf{X}^{(n)}\mathbf{X}^{(n)T} \tag{54}$$

not as a $N \times N$ matrix, but as one consisting of $2^{M-1} \times 2^{M-1}$ blocks of $N \times N$ matrices so that it may act in (53) as a transition matrix between vector blocks.

Thus in (54) P_n is determined by $\mathbf{X}^{(n)}$, i.e., from (1), by

$$\mathbf{X}^{(n)} = B\begin{pmatrix} a_n \\ a_{n+1} \\ \cdot \\ \cdot \\ \cdot \\ a_{n+M-1} \end{pmatrix}. \tag{55}$$

Hence the "super-index" J corresponding to the vector result of an operation by P_n would be the last $M - 1$ components of $\mathbf{a}^{(n)}$, namely $(a_{n+1}, a_{n+2}, \cdots, a_{n+m-1})$. On the other hand, P_n acts on a quantity determined by

$$\mathbf{X}^{(n-1)} = B\begin{pmatrix} a_{n-1} \\ a_n \\ \cdot \\ \cdot \\ \cdot \\ a_{n+m-2} \end{pmatrix}; \tag{56}$$

that is, something with vector index $J' = (a_n, \cdots, a_{n+m-2})$. Thus if we call

$$I - \alpha\mathbf{X}^{(n)}\mathbf{X}^{(n)T} \equiv K(J, J'), \tag{57}$$

$K(J, J')$ can only act between index pairs (J, J'), which are "shift-compatible." Thus if

$$\begin{aligned} J &\leftrightarrow (s_1, \cdots, s_{m-1}) \\ J' &\leftrightarrow (t_1, \cdots, t_{m-1}), \end{aligned} \tag{58}$$

where the s_i and t_i are binary variables, then

$$K(J, J') = 0 \quad \text{unless} \quad s_i = t_{i+1}, \qquad i = 1, \cdots, M-2. \tag{59}$$

On the other hand, if (J, J') are shift-compatible, this is enough to determine the appropriate $\mathbf{X}^{(n)}$. Thus with (58), (59),

$$\mathbf{X}^{(n)} = B \begin{pmatrix} t_1 \\ s_1 \\ \cdot \\ \cdot \\ \cdot \\ s_{m-1} \end{pmatrix}, \tag{60}$$

and we use (57) to define the appropriate $K(J, J')$. Having, in the manner thus described, achieved the block structure (57), we define the $N \times 2^{M-1}$ dimensional square matrix

$$A(\alpha) = \frac{1}{2} \begin{bmatrix} K(1,1) & K(1,2) & \cdots & K(1, 2^{M-1}) \\ \cdot & & & \cdot \\ \cdot & & & \cdot \\ \cdot & & & \cdot \\ K(2^{M-1}, 1) & \cdots & & \end{bmatrix}. \tag{61}$$

There are, in fact, in any row of (61) only two nonvanishing blocks. Summing over the row thus corresponds, because of the factor of ½ in front, to averaging over the first component a_n of $\mathbf{A}^{(n)}$.

We write any N vector which is further labeled by our block index J [$\mathbf{v}(J)$, say] as an $N \times 2^{M-1}$ vector $\mathbf{V}$

$$\mathbf{V} = \begin{pmatrix} \mathbf{v}(1) \\ \mathbf{v}(2) \\ \cdot \\ \cdot \\ \cdot \\ \mathbf{v}(2^{M-1}) \end{pmatrix}. \tag{62}$$

To tie this all together, it is now easy to convince oneself that, if we let V_{n+1} correspond to $E_n \epsilon^{(n+1)}$ as in (62) and, similarly, let F correspond to $E_n \mathbf{f}^{(n)}$, then, by making use of the stationarity of the averages which appear, (53) represents the solution of the equation

$$V_{n+1} = A(\alpha)\mathbf{V}_n + \mathbf{F} \tag{63}$$

with initial condition

$$V_0 = \begin{pmatrix} \epsilon^{(0)} \\ \epsilon^{(0)} \\ \cdot \\ \cdot \\ \cdot \\ \epsilon^{(0)} \end{pmatrix} \equiv [\epsilon^{(0)}]. \tag{64}$$

In (64), the notation [**v**] has been introduced to represent an n-vector "stacked" 2^{M-1} times.

The solution to (63) and (64) contains all the information we want. In fact, once $\mathbf{V}_n$ is known we, by definition, know $E_{n-1}\epsilon^{(n)}(J)$, where we have modified the notation slightly to make explicit the dependence on $J \leftrightarrow (a_{n+1}, \cdots, a_{n+M-1})$. To regain $\epsilon^{(n)}$, we simply average:

$$\epsilon^{(n)} = E[E_{n-1}\epsilon^{(n)}(J)] = \frac{1}{2^{M-1}} \sum_{J=1}^{2^{M-1}} E_{n-1}\epsilon^{(n)}(J). \tag{65}$$

The average in (65) can be put in another form if we introduce the matrix†

$$P_1 = \frac{1}{2^{M-1}} \begin{bmatrix} I & I & I & \cdots \\ I & I & I & \cdots \\ \cdot & & & \\ \cdot & & & \\ \cdot & & & \\ I & I & I & \cdots \end{bmatrix}, \tag{66}$$

having each $N \times N$ block equal to the identity matrix. Then

$$[\epsilon^{(n)}] = P_1\mathbf{V}_n. \tag{67}$$

We may already note that P_1 is an orthogonal projection operator ($P_1^2 = P_1$, $P_1^T = P_1$) and (67) thus states that $[\epsilon^{(n)}]$ is a projection of $\mathbf{V}_n$ into an appropriate subspace. Further, note that

$$[Ef^{(n)}] = [0] = P_1\mathbf{F} \tag{68}$$

and thus **F** belongs to the orthogonal subspace.

The formal solution of (63) (including the final projection) is

$$P_1\mathbf{V}_n = P_1A^n(\alpha)[\epsilon^{(0)}] + P_1 \sum_{s=0}^{n-1} A^s(\alpha)\mathbf{F} \tag{69}$$

having the limit

$$P_1\mathbf{V}_\infty = P_1[I - A(\alpha)]^{-1}\mathbf{F}. \tag{70}$$

---

† We hope a warning that the symbol P_1 is being used for different things in (66) and (48) will eliminate confusion.

Both (69) and (70) can be computed using the spectral decomposition for functions of a matrix A. If A has all its eigenvalues λ_i of index one, that is, if its eigenvectors U_i span the space (all Jordan blocks one-dimensional) and if W_i are corresponding eigenvectors of A^T, chosen so that

$$W_i^T U_j = \delta_{ij}, \tag{71}$$

then for (almost) any function $h(\cdot)$,

$$h(A) = \sum_i h(\lambda_i)\mathbf{U}_i\mathbf{W}_i^T. \tag{72}$$

Roughly, $h(\cdot)$ is restricted so that $h(\lambda_i)$ is defined. A similar but more complicated theorem holds if the U_i do not span the space. If $\alpha \neq 0$, it may be reasonable to assume that the U_i do indeed span the space, but for $\alpha = 0$ they do not.

We may already note that asymptotic stability of the full-fledged algorithm is guaranteed if all eigenvalues of $A(\alpha)$ are less than unity in magnitude. In fact, only those eigenvalues which are associated with a U_i such that $PU_i \neq 0$ need have magnitude less than unity.

In general, because of the very large dimension ($N2^{M-1}$) encountered in practical use, the above theory would be more useful if workable approximations could be found. We present one such approach in Section VI which is based on a perturbation approach for small step-size α. Before doing that, we retreat a bit to demonstrate how the mean-square error may be brought into essentially the same form just developed for the average error vector.

We again find it more convenient to discuss the error matrix $R^{(n)}$ defined in (29). We substitute (50) directly into (29) and perform our trick of taking the average E_n (which involves averaging only over a_0, $a_1, \cdots, a_n$ leaving $a_{n+1}, \cdots, a_{n+M-1}$ fixed) to obtain

$$E_nR^{(n+1)} = \frac{1}{2}\sum_{a_n} P_n(E_{n-1}R^{(n)})P_n + \frac{1}{2}\sum_{a_n} \mathbf{f}^{(n)}\mathbf{f}^{(n)T}$$
$$+ \frac{1}{2}\sum_{a_n} (P_n(E_{n-1}\epsilon^{(n)})\mathbf{f}^{(n)} + \mathbf{f}^{(n)}(E_{n-1}\epsilon^{(n)})^T P_n). \tag{73}$$

In (73), $\sum_{a_n}$ refers to summing over $a_n = \pm 1$. Note that in (73) the sequence of quantities $E_{n-1}\epsilon^{(n)}$ may be regarded as known (or calculable) since they are the N dimensional subvectors which make up the $N \times 2^{M-1}$ dimensional solution V_n to (63) and (64).

We will rewrite (73), but first we need some notation. If R is any $N \times N$ matrix, we may make an N^2 dimensional vector out of it by writing the quantity

$$\xi(R) = \begin{bmatrix} R_{11} \\ R_{12} \\ \cdot \\ \cdot \\ \cdot \\ R_{1N} \\ R_{21} \\ R_{22} \\ \cdot \\ \cdot \\ \cdot \\ R_{2N} \\ \cdot \\ \cdot \\ \cdot \\ R_{N1} \\ \cdot \\ \cdot \\ \cdot \\ R_{NN} \end{bmatrix} . \tag{74}$$

We call $\xi(R)$ the vector made out of R.

In this trivial sense, we use $\xi(\cdot)$ as an operator. We use this to turn some of the terms in (73) into vectors. Introducing the "J-index" for emphasis (it is, of course, implicit when we use E_n) we define

$$\mathbf{w}^{(n+1)}(J) = \xi[E_n R^{(n+1)}(J)] \tag{75a}$$

$$\mathbf{g}(J) = \xi[E_n \mathbf{f}^{(n)} \mathbf{f}^{(n)T}] \tag{75b}$$

$$\mathbf{g}(V_n, J) = \xi[E_n \mathbf{f}^{(n)} \mathbf{f}^{(n)T} + E_n P_n \boldsymbol{\epsilon}^{(n)} \mathbf{f}^{(n)T} + E_n \mathbf{f}^{(n)} \boldsymbol{\epsilon}^{(n)T} P_n]. \tag{75c}$$

Next we note that if A, R, and B are $N \times N$ matrices, then

$$\xi(ARB) = C\xi(R), \tag{76}$$

where C is an $N^2 \times N^2$ matrix. In fact, C is the direct product $A \otimes B^T$ where $A \otimes B$ (not $A \otimes B^T$) is given by

$$A \otimes B = \begin{pmatrix} a_{11}B & a_{12}B & \cdots & a_{1N}B \\ a_{21}B & a_{22}B & \cdots & a_{2N}B \\ \cdot & & & \\ \cdot & & & \\ \cdot & & & \\ a_{N1}B & a_{N2}B & \cdots & a_{NN}B \end{pmatrix} . \tag{77}$$

In the notation (75) and (77), (73) may be rewritten as

$$\mathbf{w}^{(n+1)}(J) = \frac{1}{2}\sum_{\alpha_n} P_n \otimes P_n \mathbf{w}^{(n)}(J') + \mathbf{g}(V_n, J). \tag{78}$$

In (78) J' is the compatible pair of indices that are allowed with J. As in (63), we form $N^2 \times 2^{M-1}$ dimensional vectors $\mathbf{W}_n$, $\mathbf{G}$, and $\mathbf{G}(V_n)$ from $\mathbf{w}^{(n)}(J)$, $\mathbf{g}(J)$, and $\mathbf{g}(V_n, J)$, respectively. And finally, using the definition of $K(J, J')$ in (57) to (60) we write

$$B(\alpha) = \frac{1}{2}\begin{bmatrix} K(1,1)\otimes K(1,1) & K(1,2)\otimes K(1,2) & \cdots \\ \cdot & & \\ \cdot & & \\ \cdot & & \\ K(2^{M-1},1)\otimes K(2^{M-1},1) & \cdots & \end{bmatrix}. \tag{79}$$

The collection of equations (78) reads

$$\mathbf{W}_{n+1} = B(\alpha)\, W_n + G(V_n). \tag{80}$$

Equation (80) with (63), (64), and the initial condition

$$\mathbf{W}_0 = \begin{pmatrix} \xi(\boldsymbol{\epsilon}^{(0)}\boldsymbol{\epsilon}^{(0)T}) \\ \xi(\boldsymbol{\epsilon}^{0}\boldsymbol{\epsilon}^{(0)T}) \\ \cdot \\ \cdot \\ \cdot \\ \xi(\epsilon^{0}\epsilon^{(0)T}) \end{pmatrix} \tag{81a}$$

provide an exact description of the error matrix.

To simplify matters, we replace (80) by the approximate version

$$\mathbf{W}_{n+1} = B(\alpha)\mathbf{W}_n + \mathbf{G}, \tag{81b}$$

where $\mathbf{G}$, as already defined, is formed from (75b) as $\mathbf{G}(V_n)$ was formed from (75c). When more is understood about the solutions of our equations, we see that the replacement of (80) by (81b) is not a serious matter.†

Again, we are not interested so much in W_n as the projected version

$$[\xi(R^{(n)})] = P_1\mathbf{W}_n. \tag{82}$$

In (82) the bracket notation is the same as (64) except that $\xi(R^{(n)})$ is a vector of dimension N^2 instead of N. Also, in (32) P_i has the same meaning as in (66) except that the identity matrices are all in N^2 dimensions instead of N.

---

† In most situations, $\mathbf{G}(V_n)$ is small compared to the initial error and the associated transient. The main effect of the forcing term is to give a nonzero error as $n \to \infty$. But $V_n \to 0$, and $\mathbf{G}(V_n)$ reduces to $\mathbf{G}$.

In summary, we thus see that both eq. (63) for $\mathbf{V}_n$, which represents $E_{n-1}\epsilon^{(n)}$, and (81b) for $\mathbf{W}_n$, which represents $E_{n-1}R^{(n)}$, have the form

$$\mathscr{V}_{n+1} = \mathscr{A}(\alpha)\mathscr{V}_n + \mathscr{F}, \tag{83}$$

with

$$\mathscr{V}_0 = [\phi], \tag{84}$$

and the quantity of interest being

$$\mathscr{P}_1\mathscr{V}_n \tag{85}$$

for the appropriate dimension and projection $\mathscr{P}_1$.

V. THE CASE $\alpha = 0$

The equalization problem is uninteresting when the step-size is taken to be zero, i.e., nothing happens. However, since we soon intend to do a perturbation analysis about $\alpha = 0$ we must be familiar with our formalism when $\alpha = 0$. This is not trivial, and we devote this section to it.

To display matrices explicitly, we need a labeling procedure. We let the "super-index" **J** run from 0 to $(2^{M-1} - 1)$.† The **J** value which labels $(a_1, \cdots, a_{M-1})(a_i = \pm 1)$ is gotten as follows: Change +1 to 0, and −1 to 1, obtaining then binary representation of J. Thus, for $M = 3$, $J = 0, 1, 2, 3$ correspond respectively to $(+, +)$, $(+-)$, $(-+)$, and $(-, -)$. With this labeling we have

$$\mathscr{A}(0) = \frac{1}{2}\begin{bmatrix} 1 & & 1 & \\ 1 & & 1 & \\ 01 & 0 & 01 & 0 \\ 01 & & 01 & \\ 001 & & 001 & \\ 001 & & 001 & \\ \cdot & & \cdot & \\ \cdot & & \cdot & \\ \cdot & & \cdot & \\ 000 \cdots & 1 & 00 \quad \cdots & 1 \\ 000 \cdots & 1 & 00 \quad \cdots & 1 \end{bmatrix} \otimes I \equiv \Gamma \otimes I. \tag{86}$$

Let S be vector space of dimension N or N^2 accordingly as $\mathscr{V}_n$ in (83) refers to $\mathbf{V}_n$ or $\mathbf{W}_n$. Then in (86) I refers to the identity in S.

The matrix $\mathscr{A}(\alpha)$ has the same structure as (86), with each identity being replaced by the appropriate $I - \alpha XX^T$ or $(I - \alpha XX^T) \otimes (I - \alpha XX^T)$.

---

† This labeling is for descriptive convenience here. We hope the reader is forgiving if we later let $\mathbf{J} = 1, 2, \cdots, 2^{M-1}$. We will be explicit about the convention when it matters.

Table I—Zero eigenvalue structure of Γ

Index	# Blocks of This Index
$M-1$	1
$M-2$	1
$M-3$	2
$M-4$	4
$M-5$	8
$\vdots$	
$M-l$	$2^{l-2} (l \geq 3)$
$\vdots$	
$M-(M-2)=2$	2^{M-4}
1	2^{M-3}

The matrix Γ in (86) is basic to our study and we now concentrate on it; it has dimension 2^{M-1}. Clearly, the all-ones vector is an eigenvector of Γ having eigenvalue one. The reader may convince himself that Γ^{M-1} is proportional to the matrix consisting of all ones, which has $(2^{M-1}-1)$ eigenvectors perpendicular to the all-ones vector. These eigenvectors are associated with eigenvalue zero. Using the fact that the eigenvalues of a power of a matrix are the powers of the eigenvalues, we conclude that Γ has one unity eigenvalue and $(2^{M-1}-1)$ zero ones. The zero eigenvalues are not of index one however (index, recall, is the dimension of the Jordan block). Table I summarizes the structure of the zero eigenvalues of Γ.

While it is not crucial for the sequel, we also give the eigenvectors and generalized eigenvectors of Γ. These are the columns, albeit permuted, of Hadamard matrices H_n constructed according to $H_2 = 1$,

$$H_{2n} = \begin{bmatrix} H_n & H_n \\ H_n & -H_n \end{bmatrix} = H_{2n}^T. \tag{87}$$

Rows and columns of H_n are labeled from 0 to $n-1$. Our claim is that the columns of $H(2^M-1)$ are the (unnormalized) generalized eigenvectors of Γ. Recall that a sequence of vectors x_l, $l = 1, \cdots, k$ forms a chain of generalized eigenvectors corresponding to a k-dimensional Jordan block when

$$\Gamma X_l = X_{l+1} \qquad l = 1, \cdots, k-1$$

$$\Gamma X_k = \lambda X_k.$$

Clearly, the last 2^{M-2} columns of H satisfy $\Gamma X_k = 0$ and these are the only ones. If c_k is the kth column, $2^{M-2}+1 \leq k \leq 2^{M-1}$, then the chain that ends with it is, in reverse order,†

---

† For (88) to hold, it is essential that the first column be labeled c_0. Also, of course, the c_k of this section is different from c_k in Section II where it signified equalizer taps. No confusion should arise.

$$(c_k,\ c_{k/2},\ c_{k/4},\ \cdots). \tag{88}$$

These notions may be verified for

$$H_8 = \begin{bmatrix} 1 & 1 & 1 & 1 & 1 & 1 & 1 & 1 \\ 1 & -1 & 1 & -1 & 1 & -1 & 1 & -1 \\ 1 & 1 & -1 & -1 & 1 & 1 & -1 & -1 \\ 1 & -1 & -1 & 1 & 1 & -1 & -1 & 1 \\ 1 & 1 & 1 & 1 & -1 & -1 & -1 & -1 \\ 1 & -1 & 1 & -1 & -1 & 1 & -1 & 1 \\ 1 & 1 & -1 & -1 & -1 & -1 & 1 & 1 \\ 1 & -1 & -1 & 1 & -1 & 1 & 1 & -1 \end{bmatrix}. \tag{89}$$

The chains are (4, 2, 1), (5), (6, 3), (7). If we rearrange the columns of H_8 to give

$$\hat{H}_8 = (c_0,\ c_5,\ c_7,\ c_6,\ c_3,\ c_4,\ c_2,\ c_1), \tag{90}$$

then

$$\frac{1}{8}\hat{H}_8^T \Gamma \hat{H}_8 = \begin{bmatrix} 1 & & & & & & & \\ & 0 & & & & & & \\ & & 0 & & & & & \\ & & & 0 & 1 & & & \\ & & & 0 & 0 & & & \\ & & & & & 0 & 1 & 0 \\ & & & & & 0 & 0 & 1 \\ & & & & & 0 & 0 & 0 \end{bmatrix}. \tag{91}$$

From the direct product structure in (86) we conclude that if Φ_i are a complete o.n. set for S, then the generalized eigenvectors of $\mathscr{A}(0)$ are

$$\frac{1}{\sqrt{2^{M-1}}}\, c_k \otimes \Phi_i, \tag{92}$$

c_k being the columns of the Hadamard matrix just described. In particular, $\mathscr{A}(0)$ has N (or N^2) unity eigenvalues of index one, having eigenvectors

$$U_i = \frac{1}{\sqrt{2^{M-1}}} \begin{bmatrix} \Phi_i \\ \Phi_i \\ \cdot \\ \cdot \\ \cdot \\ \Phi_i \end{bmatrix}; \tag{93}$$

the remaining eigenvalues are zero. The projection operator onto the space spanned by the eigenvectors having $\lambda = 1$ is, using (93),

$$\sum_i U_i U_i^T = \mathscr{P}_1, \tag{94}$$

where $\mathscr{P}_1$ has already been introduced in (66), I being the identity of S. Since $\mathscr{P}_1 = \mathscr{P}_1^T$, the projection is orthogonal. We call the projection onto the "zero eigenvalue subspace" of $\mathscr{A}(0)$ by $\mathscr{P}_0$ and $\mathscr{P}_0 = I - \mathscr{P}_1$.

Thus, when we solve (83), we really desire, according to (85), not $\mathscr{V}_n$ but $\mathscr{P}_1\mathscr{V}_n$, its projection onto the unity eigenvalue subspace of $\mathscr{A}(0)$.

A standard spectral representation of $\mathscr{A}(0)$ is

$$\mathscr{A}(0) = \mathscr{P}_1 + \mathscr{D}_0, \tag{95}$$

where $\mathscr{D}_0^{M-1} = 0$. This defines (for us) $\mathscr{D}_0$. It may be shown that $\mathscr{P}_1\mathscr{D}_0 = 0$.

We remark here that our basic equalization problem is unchanged if any infinite sample sequence of data values $\{a_n\}$ is replaced by their negatives. This follows from the quadratic nature (in the a_n) of the algorithm (19). As a consequence, we have

$$E_n\epsilon^{(n)}(I \leftrightarrow s_1, \cdots, s_{m-1}) = E\epsilon^{(n)}(J \leftrightarrow -s_1, \cdots, -s_{m-1}) \tag{96}$$

and similarly for $\mathbf{w}^{(n)}(J)$. We have not exploited this symmetry, but if we had, the dimension of $\mathscr{A}(\alpha)$ could be reduced by a factor of 2. $\mathscr{A}(0)$ would then, in particular, have a different form, but would have many of the same properties discussed here.

Finally, we take this opportunity to get some notational problems out of the way. We introduce a convenient way of labeling matrices C with block structure as in (86). Label rows by μ, $\mu = 1, 2, \cdots, 2^{M-1}$ and likewise columns by ν. If we write

$$\begin{aligned} \mu &= (i-1)n + k \qquad && 1 \le i, j \le 2^{M-1} \\ \nu &= (j-1)n + l \qquad && 1 \le k, l \le N \text{ (or } N^2) \\ & && n = N \text{ (or } N^2), \end{aligned} \tag{97}$$

then the pair (i, j) specifies which block we are concerned with, while the pair (k, l) are the usual matrix indices for the $N \times N$ (or $N^2 \times N^2$) matrix in that block. Thus, for example, in (77),

$$(A \otimes B)_{\mu\gamma} = a_{ij}b_{kl}. \tag{98}$$

Likewise, in (92) the vector $c \otimes \mathbf{\Phi}$ has components

$$(\mathbf{c} \otimes \mathbf{\Phi})_\mu = c_i\, \mathbf{\Phi}_k. \tag{99}$$

The orthonormal basis for S where the kth basis vector has a one in the kth position and zeros elsewhere is denoted by $\{e_k\}$.

VI. THE PERTURBATION THEORY

We begin the next stage of analysis by writing our matrices in a new basis. Consider the orthogonal transformation matrix U which brings $\mathscr{A}(0)$ to Jordan form, namely, the matrix U whose columns are of the form

$$\frac{1}{\sqrt{2^{M-1}}}\,\mathbf{c}_i \otimes e_k, \tag{100}$$

where $\mathbf{c}_i$ are columns of the Hadamard matrix of appropriate dimension, and $\mathbf{e}_k$ are the basis vectors of S. In (100), i and k range over all possible values. The columns of U are assumed to be arranged so that the result on $\mathscr{A}(0)$ comes out "nice." We will not bother to be too explicit, except to say that the first N(or N^2) columns of U are

$$\frac{1}{\sqrt{2^{M-1}}}\,c_0 \otimes \mathbf{e}_k \qquad k = 1, \cdots, N(N^2). \tag{101}$$

Then[†]

$$U^T\mathscr{A}(\alpha)U = \begin{bmatrix} \beta & \nu \\ \gamma & \delta \end{bmatrix} = \tilde{\mathscr{A}}(\alpha). \tag{102}$$

In (102), β is an $N \times N$ matrix, ν is $N \times (2^{M-1} - N)$ matrix, etc. If $\alpha = 0$, (102) takes the form

$$\begin{bmatrix} I & 0 \\ 0 & \mathscr{J} \end{bmatrix}, \tag{103}$$

$\mathscr{J}$ being a Jordan block exemplified by (91), i.e., "nice." Note that $\mathscr{J}^l = 0$ if $l \geq M-1$.

In general, when $\alpha \neq 0$, all blocks in (103) have added terms which are linear in α, or linear and quadratic, depending on whether (61) or (79) applies.[‡]

We shall be especially concerned with the matrix β, for it is here that the germ of independence theory appears. To calculate it, we want

$$\beta_{kl} = \left[\frac{1}{\sqrt{2^{M-1}}}\,\mathbf{c}_0 \otimes \mathbf{e}_k\right] \mathscr{A}(\alpha) \left[\frac{1}{\sqrt{2^{M-1}}}\,\mathbf{c}_0 \otimes \mathbf{e}_l\right]. \tag{104}$$

Calling the (m, n) element of the (i, j) block of $\mathscr{A}(\alpha)$ by $\frac{1}{2}\theta^{ij}_{mn}$, (104) becomes

---

[†] Henceforth, we denote transformed quantities by a tilde.

[‡] The reader should note that the simple equations (27) and (28) suggest that the linear and quadratic α-terms are of equal importance for ranges of α of interest.

$$\beta_{kl} = \frac{1}{2^M} \sum_{\substack{ij\\ mn}} (\mathbf{c}_0)_i(\mathbf{e}_k)m\ \theta^{ij}_{mn}\ (\mathbf{c}_0)_j(\mathbf{e}_l)_{n}. \tag{105}$$

Now $\theta^{ij}_{mn} = 0$ whenever Γ_{ij} in (86) is. Thus, for fixed mn there are only 2^m possible θ^{ij}_{mn} which are nonzero. Denote the sum over these as $\sum_{\text{nonzero}}$. Then (105) becomes, using $(\mathbf{e}_k)_m = \delta_{km}$, $(\mathbf{c}_0)_i = 1$

$$\beta_{kl} = \frac{1}{2^M} \sum_{\text{nonzero}} \theta^{ij}_{kl}. \tag{106}$$

Equation (106) gives β_{kl} as the average of the (k, l) elements of all 2^M blocks in $\mathscr{A}(\alpha)$ which are not *a priori* zero. This, however, is nothing but

$$E(I - \alpha\mathbf{X}\mathbf{X}^T) = I - \alpha A, \tag{107}$$

precisely the matrix which enters in the independence theory! Likewise, if $\mathscr{A}(\alpha) = \mathrm{B}(\alpha)$

$$E(I - \alpha\, XX^T) \otimes (I - \alpha XX^T) \tag{108}$$

is the matrix by which we would solve independence theory had we rewritten (31) giving $R^{(n)}$ its vector form rather than its matrix form.

What do vectors look like with our new o.n. basis? If $\mathscr{V}$ is a column vector of numbers in the original basis, then in the new basis the numbers are $U_i^T\mathscr{V}$. Let $\mathscr{V}$ be considered as blocks of $N(N^2)$ vectors Φ^i; the kth component of each is Φ^i_k. Then the inner product of a particular row of U with $\mathscr{V}$, namely,

$$\sum_{\mu} (c_i \times \mathbf{e}_k)_\mu \mathscr{V}_\mu$$

is a generic term of $U^T\ \nu$ which evaluates to

$$\frac{1}{\sqrt{2^{M-1}}} \sum_{l=1}^{2^{M-1}} (\mathbf{C}_i)_l \Phi^l_k. \tag{109}$$

Thus the first $N(N^2)$ components (the first blocks) is simply $\sqrt{2^{M-1}}$ times the average of the blocks of $\mathscr{V}$. In other words,

$$\begin{bmatrix} \Phi \\ \Phi \\ \cdot \\ \cdot \\ \cdot \\ \Phi \end{bmatrix} \rightarrow \sqrt{2^{M-1}} \begin{bmatrix} \Phi \\ \\ 0 \end{bmatrix}. \tag{110}$$

The right member of (110) is, of course, written in a notation compatible with (102). Likewise, a vector with zero average transforms to a vector which may be written

$$\sqrt{2^{M-1}}\begin{bmatrix}0\\ \Phi\end{bmatrix}. \tag{111}$$

Thus the initial condition for (63) or (80) is of type (110) unlike the driving term for (63), which is of type (111). The driving term for (80) has both types.

Finally, we note that the projection operator onto the unity eigenspace of $\mathscr{A}(0)$ is

$$\mathscr{P}_1 = \begin{bmatrix} I & 0\\ 0 & 0\end{bmatrix} \tag{112}$$

while

$$\mathscr{P}_0 = \begin{bmatrix} 0 & 0\\ 0 & I\end{bmatrix}. \tag{113}$$

It will also be convenient to write

$$U^T\mathscr{V}_n = \tilde{\mathscr{V}}_n = \frac{1}{\sqrt{2^{M-1}}}\begin{bmatrix}x_n\\ y_n\end{bmatrix}. \tag{110b}$$

Putting together the pieces just described in this section, the contrast between the mathematics of the exact theory and independence theory is as follows. The former problem is the following: solve for x_n where

$$\begin{bmatrix}x_{n+1}\\ y_{n+1}\end{bmatrix} = \begin{bmatrix}\beta & \nu\\ \gamma & \delta\end{bmatrix}\begin{bmatrix}x_n\\ y_n\end{bmatrix} + \begin{bmatrix}\Phi\\ \Psi\end{bmatrix}, \tag{114}$$

where x_0 is given, $y_0 = 0$. The latter problem is: Solve for x_n where

$$x_{n+1} = \beta x_n + \Phi, \tag{115}$$

x_0 is given. Note if ν and γ in (114) were zero, the solution to the two problems would be identical. Since ν and γ vanish when $\alpha = 0$, we may hope a perturbation approach will be useful for small α. More specifically, we treat

$$\begin{bmatrix}\beta - I & \nu\\ \gamma & \delta - \mathscr{I}\end{bmatrix}$$

as a perturbation of (103), the matrix $\tilde{A}(\alpha)$ when $\alpha = 0$.

We begin by considering the eigenvalue problem for $\mathscr{A}(\alpha)$. When $\alpha = 0$, the eigenvalues of β are unity while these of δ are zero, and these eigenvalues vary continuously as α is increased. Consider solving for the large eigenvalues. In general, we have to solve

$$\begin{aligned} \beta x + \nu y &= \lambda x \\ \gamma x + \delta y &= \lambda y, \end{aligned} \tag{116}$$

where λ is one of these eigenvalues, presumed close to one. Since the eigenvalues of δ will be presumed smaller than λ, $(\lambda - \delta)^{-1}$ exists and we conclude from the second equation of (116) that

$$y = (\lambda - \delta)^{-1}\gamma x.$$

Substituting this into the first equation yields

$$\left[\beta + \nu \frac{1}{\lambda - \delta}\gamma\right] x = \lambda x. \tag{117}$$

Consistent with the perturbation spirit, we replace the λ (on the left) by 1 and δ by its value when $\alpha = 0$, namely, $\mathscr{J}$ [see (103)].

Thus the large λ's are (approximately) solutions to

$$\left[\beta + \nu \frac{1}{I - \mathscr{J}}\gamma\right] x = \lambda x \tag{118}$$

and the corresponding eigenvector to $\mathscr{A}(\alpha)$ is, approximately,†

$$\begin{bmatrix} x \\ \dfrac{1}{I - \mathscr{J}}\gamma x \end{bmatrix}. \tag{119}$$

Using these approximations and applying the spectral decomposition discussed in (72) to evaluate $\mathscr{A}^n(\alpha)$, it is now straightforward to show that the desired solution to (114) is, at least if we neglect the small eigenvalues.

$$x_n = \left[\beta + \nu \frac{1}{I - \mathscr{J}}\gamma\right]^n x_0 + \sum_{s=0}^{n-1} \left[\beta + \nu \frac{1}{I - \mathscr{J}}\gamma\right]^s \left[\Phi + \nu \frac{1}{I - \mathscr{J}}\Psi\right]. \tag{120}$$

---

† With the present representation, the perturbation theory has been painless. More formal and more thorough approaches to perturbation theory of matrices may be found in Refs. 2 and 3.

From (120) we conclude

$$\lim_{n\to\infty} \mathrm{x}_n = [\mathbf{I} - \beta - \nu \frac{1}{\mathbf{I} - \mathcal{J}} \gamma]^{-1}[\Phi + \nu \frac{1}{I - \mathcal{J}} \Psi]. \tag{121}$$

In fact, the steady-state error can also be computed exactly from (114) as

$$[I - \beta - \nu \frac{1}{I - \delta} \gamma]^{-1}[\Phi + \nu \frac{1}{1 - \delta} \Psi]. \tag{122}$$

Within the spirit of our approximations, (122) is consistent with (121). The neglect of the small eigenvalues is justified by the fact that their contribution will damp out quickly, and also that they operate in a subspace approximately orthogonal to the one we are interested in. Thus in (119) the "second half" of the large eigenvector is small because of the γ factor. The corresponding form for the "small" eigenvectors would have the first portion small.

We take (120) and (121) as our approximate solution. The terms

$$\nu \frac{1}{I - \mathcal{J}} \gamma \quad \text{and} \quad \nu \frac{1}{I - \mathcal{J}} \Psi \tag{123}$$

are higher order terms in the perturbation, and neglecting them we obtain†

$$x_n = \beta^n x_0 + \sum_{s=0}^{n-1} \beta^s \Phi \tag{124}$$

$$x_\infty = \frac{1}{I - \beta} \Phi, \tag{125}$$

exactly what independence theory would predict.

To examine further the key expression

$$\beta + \nu \frac{1}{I - \mathcal{J}} \gamma, \tag{126}$$

some more concrete expression for the $\nu\gamma$ type terms is needed. For example, consider an initial error matrix R_0. Then

$$R_1 = E[I - \alpha X_1 X_1^T] R_0 [I - \alpha X_1 X_1^T]. \tag{127}$$

This must correspond to β and so, as we already know,

$$\beta = E[I - \alpha \mathbf{X}_1 \mathbf{X}_1^T] \otimes [I - \alpha \mathbf{X}_1 \mathbf{X}_1^T]. \tag{128}$$

In general, then (neglecting the forcing terms), independence theory

---

† Noting that $(\lambda + \epsilon)^n \approx \lambda^n$ for $n = 0(1/\epsilon)$ but not for $n \to \infty$, we expect the approximation to break down after a while. This may very well happen only after the taps have, for practical purposes, converged to the desired solution.

can be written (letting $P_n = I - \alpha \mathbf{X}_n \mathbf{X}_n^T$)

$$R_{n+1} = EP_1R_nP_1. \tag{129}$$

If we consider two iterations

$$R_2 = E[I - \alpha X_2X_2^T][I - \alpha X_1X_1^T]R_0[I - \alpha X_1X_1^T][I - \alpha X_2X_2^T], \tag{130}$$

this corresponds, on squaring the matrix in (102), to $\beta^2 + \nu\gamma$. Thus $\nu\gamma$ corresponds to

$$E[P_2P_1R_0P_1P_2 - P_\infty P_1R_0P_1P_\infty], \tag{131}$$

where P_∞ is simply a notation denoting that it (P_∞) is to be treated independently of P_1. The matrix R_0 is not statistical. The proper way to write (131) is†

$$\nu\gamma = E[(P_2 \otimes P_2)(P_1 \otimes P_1) - \beta^2]. \tag{132}$$

In general, it can be shown

$$\nu \frac{1}{I - \mathscr{J}} \gamma = \sum_{s=0}^{M-2} \nu \mathscr{J}^s \gamma = \sum_{s=2}^{M} [E(P_s \otimes P_s)(P_1 \otimes P_1) - \beta^2]. \tag{133}$$

Using (133) in (126) provides us with the next correction to the eigenvalues by way of (118).

Furthermore, (133) suggests a simplified "dynamics" for R_n, namely,

$$R_{n+1} = EP_1R_nP_1 + E \sum_{s=1}^{M-1} [P_{1+s}P_1R_{n-s}P_1P_{1+s} - P_\infty P_1R_{n-s}P_1P_\infty]. \tag{134}$$

A general discussion of these correction terms seems out of the question. In fact, the expectations are not trivial to do. Instead, we resort again to the simple model of (15), where $A = I$, and $\mathscr{E}_{ex}^{(n)} = \operatorname{tr} R_n$, and set $N = 3$. For this case, we have been able to do the expectations and compute the eigenvalues of β and $\beta + \nu[1/(I - \mathscr{J})]\gamma$. The eigenvalues results are given in Table II. Certainly, in this case the perturbation philosophy seems well justified.

VII. CONCLUSIONS

We conclude (as explained above) that a perturbation analysis suggests that the difference between independence theory and one which takes into account the correlations between the "gradient"

---

† Using $(A \otimes B)(C \otimes D) = AC \otimes BD$, other forms are, of course, possible.

Table II—A comparison of the eigenvalues of β and its perturbation for a special situation

β	$\beta + \nu \frac{1}{I - \mathcal{J}} \gamma$
0.667	0.674
0.555	0.543
0.555	0.555
0.555	0.555
0.333	0.337
0.333	0.333
0.333	0.333
0.333	0.333
0.333	0.333

directions is slight. Our early worry was that the shifting property

$$\begin{bmatrix} x_1 \\ x_2 \\ \cdot \\ \cdot \\ \cdot \\ x_n \end{bmatrix} \rightarrow \begin{bmatrix} x_2 \\ x_3 \\ \cdot \\ \cdot \\ \cdot \\ x_{n+1} \end{bmatrix} \tag{135}$$

in going from one gradient direction to the next could cause trouble with independence theory. Any notion that this particular dependence must result in mathematics completely foreign to that of independence theory has been shown to be false. Independence theory is an inherent part of the exact description.

The situation in (135) does, however, have the rigorous property that the "new" component (x_{n+1}) is independent of the others. For real problems, this situation may well be violated in certain cases of severe intersymbol interference. Examining the $N = 1$ case leads us to propose the following criterion to measure this dependence. Namely, if, in the synchronous case, the received pulse $h(t)$ [see (1)] is normalized so that $\sum_{-\infty}^{\infty} h_n^2 = 1$, then we might expect

$$\sum_{s=1}^{\infty} \left(\sum_{l=-\infty}^{\infty} h_l h_{l+s} \right)^2 \ll 1$$

to be a good measure of independence for the new component.

Our effort has been a long and tedious one, and our attempts to pull insights from complicated equations have sometimes been nonrigorous and no doubt occasionally colored by the previous experimental results and simulation results of others.[1] Thus, while the ultimate justification of independence theory must remain empirical, we hope that our efforts at least make mathematically plausible the successes of independence theory.

Finally, it is a pleasure to say that the present work has benefited from discussions with J. Salz, L. A. Shepp, N. J. A. Sloane, and H. S. Witsenhausen.

APPENDIX A

Evaluation of Some Averages

For the purposes of this appendix, we drop the superscript in (11), labeling things as if $n = 1$. For application to (31) we consider the average

$$E\mathbf{X}\mathbf{X}^T R\mathbf{X}\mathbf{X}^T \tag{136}$$

for an arbitrary $N \times N$ matrix R. Here (11) holds, and we are averaging over the binary variables in $\mathbf{a}$. Expanding (136) using (11) we have to do the key average

$$Eaa^T Qaa^T \equiv EC, \tag{137}$$

where $Q = B^T RB$. Thus from (137),

$$\begin{aligned}(EC)_{ij} &= E\sum_{k,l} (\mathbf{a}\mathbf{a}^T)_{ik} Q_{kl} (\mathbf{a}\mathbf{a}^T)_{lj} \\ &= E\sum_{k,l} a_i a_k a_l a_j Q_{kl}.\end{aligned} \tag{138}$$

Using the fact that for independent binary variables

$$Ea_i a_k a_l a_j = \delta_{ik}\delta_{lj} + \delta_{il}\delta_{kj} + \delta_{ij}\delta_{kl} - 2\delta_{ik}\delta_{il}\delta_{ij} \tag{139}$$

we obtain, upon using (139) in (138)

$$(EC)_{ij} = Q_{ij} + Q_{ji} + (\text{tr } Q)\delta_{ij} - 2Q_{ii}\delta_{ij}. \tag{140}$$

In matrix notation, (140) becomes

$$EC = Q + Q^T + (\text{tr } Q)I - 2 \text{ diag } Q, \tag{141}$$

with the definition

$$(\text{diag } Q)_{ij} = (Q_{ii})\delta_{ij}. \tag{142}$$

Note that if the a_i were unit-variance Gaussian, the last term in (141) (diag Q) would not arise. It will be dropped because it is small in usual cases. Finally, multiplying (141) on the left by B and on the right by B^T we recover (136), obtaining (since Q is symmetric now)

$$E\mathbf{X}\mathbf{X}^T RXX^T = 2\,ARA + (\text{tr } RA)A - 2B(\text{diag } B^T RB)B^T. \tag{143}$$

Now we recall that all terms in (143) are multiplied by α^2. We would neglect them all unless one can be large. In fact, (tr $RA)A$ can be N times larger and hence this is the only term we need keep.

We move on to consider (32), rewritten as

$$-E\alpha(I - \alpha\boldsymbol{x}\boldsymbol{x}^T)\epsilon[\mathbf{c}^{*T}\boldsymbol{x}\boldsymbol{x}^T - a_{n+J}X^T]. \tag{144}$$

The term linear in α in (144) vanishes as a correspondence of (6), (7), and (9). One of the α^2 terms is

$$\alpha^2 EXX^T\boldsymbol{\epsilon}\mathbf{c}^{*T}XX^T. \tag{145}$$

Evaluating (145) using (143), we check to see if the dominant term can be large. It is given by

$$A \text{ tr } \boldsymbol{\epsilon}\mathbf{c}^{*T}A = A(\boldsymbol{\epsilon}^T A\mathbf{c}^*). \tag{146}$$

If we introduce the $(M - 1)$ vector $\mathbf{u}$, having all zeros except a one in the $(1 + J)$ place, then

$$a_{n+J} = \mathbf{u}\cdot\mathbf{a} = u^T\mathbf{a}, \tag{147}$$

and the other α^2 term is proportional to

$$\alpha^2 EXX^T\boldsymbol{\epsilon}\mathbf{u}^T\mathbf{a}X^T = \alpha^2 EB[\mathbf{a}\mathbf{a}^T(B^T\boldsymbol{\epsilon}\mathbf{u}^T)\mathbf{a}\mathbf{a}^T]B^T. \tag{148}$$

Evaluating (148) using (138) and (141), we get

$$A(\epsilon^T Bu). \tag{149}$$

However, using (7) we readily verify $B\mathbf{u} = \mathbf{v}$, and a final use of (9) shows that the two dominant α^2 terms (146) and (149) cancel. The other terms are truly α^2 terms (as opposed to $\alpha^2 N$) and are neglected, leading us to replace (32) by zero.

We have introduced enough tricks now so that the reader may easily reproduce (33).

APPENDIX B

Definiteness of Solution to (34)

We give here an explicit demonstration that the solution to (34) retains its positive definite character. By induction on n, it is sufficient to show that $R^{(n+1)}$ is positive definite (≥ 0) if $R^{(n)}$ is.

We make repeated use that $R \geq 0$ if R is hermitian and $\phi^T R\phi \geq 0$ for any vector ϕ.

We recall $A \geq 0$ (and therefore hermitian) and hence $R^{(n+1)}$ is hermitian.

Rewrite the right member of (34) as

$$(I - \alpha A)R(I - \alpha A) + \alpha^2[A \text{ tr } AR - ARA] + \alpha^2\mathscr{E}^*A. \tag{150}$$

Each term in (150) is positive definite; the only nonobvious one is the second. However, it may be rewritten as

$$\sqrt{A}\,[\mathrm{tr}\,\sqrt{A}\,R\,\sqrt{A} - \sqrt{A}\,R\,\sqrt{A}]\,\sqrt{A}, \tag{151}$$

since tr AB = tr BA. The matrix $\sqrt{A}\,R\,\sqrt{A}$ is, of course, positive definite. Now observe that if $B \geq 0$ then tr $B - B \geq 0$. This concludes the proof.

REFERENCES

1. G. Ungerboeck, "Theory on the Speed of Convergence in Adaptive Equalizers for Digital Communication," IBM J. Res. Develop., *16*, No. 6 (November 1972), pp. 546–555.
2. Peter Lancaster, *Theory of Matrices*, New York: Academic Press, 1969. The Perron-Frobenius theorem used immediately before (45) of the text is given in this reference as the corollary on p. 286.
3. T. Kato, *Perturbation Theory for Linear Operators*, New York: Springer-Verlag, 1976. See Chapter 2 for matrices.

Copyright © 1979 American Telephone and Telegraph Company
THE BELL SYSTEM TECHNICAL JOURNAL
Vol. 58, No. 5, May–June 1979
Printed in U.S.A.

Transmission Properties of Various Styles of Printed Wiring Boards

By A. J. RAINAL

(Manuscript received October 18, 1978)

This paper presents some experimental results concerning the pulse transmission properties of fine line printed conductors (e.g., width = 8 mils, spaces = 9 mils) on various styles of circuit packs (CPs). The pulse transmission properties include the characteristic impedance, the propagation delay, the rise time, the bandwidth, and the intralayer and interlayer pulse crosstalk. A simplified theoretical model is presented which leads directly to some basic crosstalk equations. Theoretical results are developed to extend the application of the experimental crosstalk results to arbitrary pulse signals, periodic signals, and random signals. Also, theoretical scaling laws are developed to extend the crosstalk results to conductor spaces in the range of 7 to 40 mils. The crosstalk results are very important, since they tend to limit the packaging density of printed conductors on the CP styles by limiting the coupled length and spacing of parallel conductors. The results can be incorporated into computer-aided designs which can analyze routed CPs to detect potential crosstalk problems before the CP routing is finalized for manufacture. Other applications include CP selection, crosstalk estimation, electrical characterization of CPs and backplanes, estimation of conductor capacitance and inductance, and effects of various dielectrics. The results are applicable to general styles of printed wiring boards. In particular, they apply directly to all styles of CPs in the BELLPAC™ *apparatus housing—a modular packaging system for packaging electronic equipment in the Bell System.*

I. INTRODUCTION

In the physical design of large electronic systems, the interconnection of the integrated circuits and other components at the circuit pack or printed wiring-board level constitutes a basic and relatively expensive level of interconnection. In addition to supplying power and ground, the circuit pack (CP) provides the conductor paths for the

Table I—Description of the circuit pack styles

Circuit Pack Style	Description
Wire wrap	Wire wrap board for breadboarding
Extender board	6 layer MLB, 2 pad layers, 2 signal layers, power (P) and ground (G) on inside, dedicated ground conductor between every pair of signal conductors
Double-sided (epoxy)	Double-sided, epoxy PWB
Double-sided (metal)	Double-sided, metal core, PWB
Bonded board (LAMPAC)†	Flex bonded to epoxy coated steel
4L MLB (EXT P/G)	4 layer MLB, 2 signal layers, P and G on outside
6L MLB (EXT P/G)	6 layer MLB, 4 signal layers, P and G on outside
6L MLB (INT P/G)	6 layer MLB, 2 pad layers, 2 signal layers, P and G on inside
6L MLB (INT P/G, surface routing)	6 layer MLB, 4 signal layers, P and G on inside
8L MLB (INT P/G)	8 layer MLB, 2 pad layers, 4 signal layers, P and G on inside

† This particular bonded board is also known as LAMPAC.

transmission of pulses and other types of signals between the integrated circuits, other components, and the CP connector.

The basic pulse transmission properties, such as characteristic impedance, propagation delay, rise time, bandwidth, and crosstalk depend a great deal on the CP configuration or style. Since the costs associated with the various CP styles differ significantly, it is very important to develop CP styles which are suitable electrically and which are relatively inexpensive.

For the past few years, a Bell System packaging effort[1] (*BELLPAC** packaging system) has been under way to develop a modular packaging system for packaging electronic equipment. This effort makes use of a suitable connector (963) and a number of CP styles that have common features suitable for computer-aided design.

The purpose of this paper is to present some basic transmission properties of various styles of CPs which include those in the *BELLPAC* hardware family. The transmission properties are very important, since they help to determine which CP style is most appropriate for a given application.

A listing of the CP styles along with a short description of each is presented in Table I. Copper conductors are used on all the CP styles. The dielectric material for most CPs is a composite of epoxy and glass fibers. The composite structure has a relative dielectric constant (effective) of about 4.2. Except for the extender board, all the CP styles have the common features shown in Fig. 1.

---

* Trademark of Western Electric.

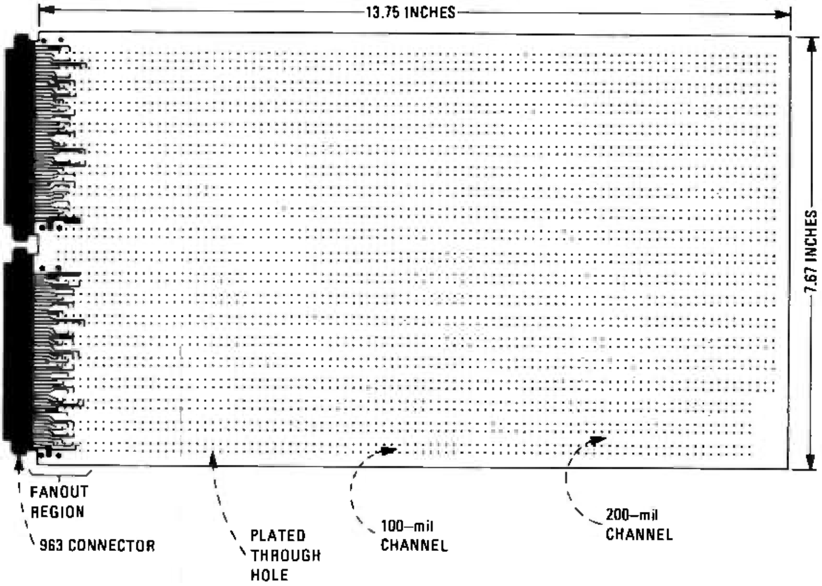

Fig. 1—Some common features applying to all circuit pack styles except the extender board. The plated-through holes are on either 100-mil or 200-mil centers. The spaces between the rows of plated-through holes are denoted as 100-mil or 200-mil channels.

The extender board is a very special design. Its primary function is to extend any CP beyond the apparatus housing so that both sides of the CP are accessible for debugging or test purposes. Thus, the extender board is basically an "extension cord" for a CP.

To determine the basic transmission properties of the various CPs, appropriate test boards were designed for each style of CP listed in Table I. Except for the double-sided (metal) board, all test boards were fabricated at the Western Electric printed-circuit manufacturing plant at Richmond, Virginia. The double-sided metal board was manufactured at the Western Electric plant in Kearny, New Jersey. The test routing consisted of either 8 ± 2 mil conductors with nominal 9-mil spaces or 12 ± 3 mil conductors with nominal 13-mil spaces. The 8-mil conductors were on 17-mil centers, and the 12-mil conductors were on 25-mil centers. In general, the length of the conductor paths was about 1 foot.

An experimental approach was necessary for this study because detailed theoretical models which include all CP styles of interest become very complicated, and they are not now very useful for determining many basic pulse transmission properties. The experimental methods used to determine the transmission properties of the test boards are described in the next section.

II. DESCRIPTION OF THE EXPERIMENTAL METHODS

2.1 Pulse transmission properties

Each CP style containing the test routing was probed with a Hewlett Packard time domain reflectometer (TDR) system consisting of a 1815A sampling plug-in, an 1817A sampling head, and an 1106B tunnel diode pulse generator. The TDR system was used to apply a fast rising step signal into each CP and display the reflected waveform on a sampling oscilloscope. In general, the conductor path on the CP was open-circuited and was free of any parallel branches.

For purposes of detailed analysis, a photograph was taken of each TDR display of interest. The general form of the TDR display is presented in Fig. 2. By analyzing the TDR display of the reflected waveform, one can determine the basic pulse transmission properties of the various CP styles. The particular CP properties of interest are the characteristic impedance, Z_1, the propagation delay, T_d, the 80-percent rise time, T_r, and the bandwidth, B. All these CP properties can be determined by analyzing each TDR display as indicated in Fig. 2. The 80-percent rise time, T_r, on the TDR display is a result of the input step signal traversing the CP twice, as is characteristic of a reflection method. The one-way rise time is faster by a factor of approximately $1/\sqrt{2}$. By applying this factor to the usual relationship between bandwidth and rise time, we have

$$B = \frac{0.35}{T_r/\sqrt{2}} \doteq \frac{1}{2T_r}. \tag{1}$$

Reference 2 presents some additional discussion concerning the TDR method along with some detailed results concerning the theoretical TDR display for an ideal CP.

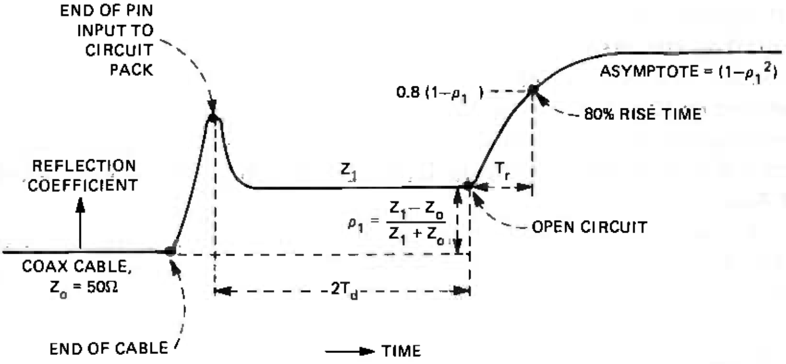

Fig. 2—The general form of the TDR display.

2.2 Pulse crosstalk properties

The pulse crosstalk properties of the CPs were determined experimentally by using the method described in Refs. 3, 4, and 5. Briefly, the method consists of applying a fast pulse (rise time ~ 2 ns) to a driven conductor and monitoring the resultant waveform at the near-end or far-end of some idle conductor of interest. In all cases, the crosstalk results apply when all conductors are properly terminated with matched loads. The corresponding results for other loads can yield higher values of crosstalk which can be estimated from the results for matched loads by determining the reflections and using superposition. Thus, the crosstalk results for the matched loads are basic properties of the CP styles. The crosstalk results are very important since they limit the packaging density of printed conductors on the CPs by limiting the coupled length and spacing of parallel conductors.

We now summarize all the experimental results presented in the appendix to this paper.

III. SUMMARY OF THE EXPERIMENTAL RESULTS

Table II presents a summary of the pulse transmission properties of all the CPs considered in this paper. More detailed properties for each of the CP styles are presented in the appendix, as stated in the last column of Table II.

The propagation delay per foot, the rise time, and the bandwidth include the effects of the 963 connector plus fanout (see Fig. 1). However, an earlier study[6] has shown that the 963 connector plus fanout limits all the CP styles to applications having one-way signal rise times ($= 1/\sqrt{2}$ of the TDR rise time values) no faster than about 2.0 ns (bandwidths $\leq$ 175 MHz). This 2.0-ns limit was determined by considering the crosstalk levels and impedance mismatch associated with the 963 connector plus fanout. This lower limit on signal rise time is sufficient to include most applications in the Bell System.

The pulse crosstalk results were measured as a percentage of the signal step in the driven conductor. The crosstalk results apply when the printed conductors are terminated with matched loads.

The interlayer crosstalk can be decreased to negligible values by simply using orthogonal routing on adjacent layers. This technique is now widely used during the routing of the conductors. Therefore, intralayer crosstalk is usually more of a concern than is interlayer crosstalk.

The attenuation of the conductors has not been thoroughly investigated, but some preliminary results have shown that signal attenuation is about 0.4 dB/ft at 250 MHz.

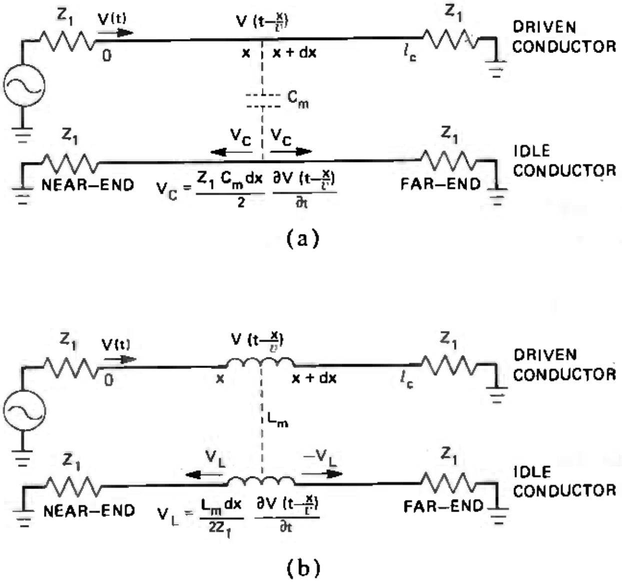

Fig. 3—A simplified model of crosstalk for a pair of lossless, uniformly, and loosely coupled conductors terminated with matched loads. Z_1, v, and l_c denote characteristic impedance, propagation velocity, and coupled length, respectively. (a) Capacitive crosstalk, V_c, resulting from the mutual capacitance per unit length, C_m. (b) Inductive crosstalk, V_L, resulting from the mutual inductance per unit length, L_m.

Table II shows that the CP styles in the *BELLPAC* family of CPs* provide a wide variety of pulse transmission properties that can satisfy the CP needs of most presentday Bell System projects. Many current projects (e.g., AMARC, PDT2A, PLAID, Triport, ESS Ring and Tone, DIF) make use of the double-sided (epoxy) style. In fact, this is the most common CP style. The double-sided metal CP is used in customer equipment and is now under consideration for power supply applications. The 4L MLB and 6L MLB (EXT P/G) were used in some switching applications such as the PROCON project. The higher capability MLBs, the 6L MLBs (INT P/G with and without surface routing), were used in the 1A ESS processor, and are expected to find use in projects such as the 3B ESS processor and DIF.

IV. THEORETICAL CROSSTALK RESULTS

4.1 Derivation of basic crosstalk equations

Consider the simplified model of crosstalk presented in Fig. 3. The capacitive crosstalk voltage denoted by V_c in Fig. 3a is a suitable approximation when the conductors are loosely coupled. A more

---

* At the present time, the bonded board (LAMPAC) and the 8L MLB (INT P/G) are not members of the *BELLPAC* family of CP's.

Table II—Summary of pulse transmission properties of various circuit pack styles

Circuit Pack Style	Characteristic Impedance (ohms)	Propagation delay* (ns per ft)	Rise time* (TDR) (ns)	Bandwidth* (MHz)	Maximum† Interlayer Pulse Crosstalk (Near-End) (percent)	Maximum† Intralayer Pulse Crosstalk (Near-End) (percent)	More Details Shown in the Following Figures in the Appendix
Wire wrap‡	125 ± 50	1.4	2.0	250	—	40	4
	160 ± 35	1.3	1.8	278		35	
Extender Board	70 ± 5	1.8	1.3	385	0.3	1.6	5
Double-Sided	150 ± 20	1.5	2.6	190	21	39	6
(epoxy)§	150 ± 20	1.5	2.6	190	24	34	
Double-Sided	98 ± 8	1.5	2.6	190	1.2	15	7
(metal)§	83 ± 6	1.5	2.6	190	3.2	13	
Bonded Board§	95 ± 10	1.5	2.6	190	38	21	8
(LAMPAC)	85 ± 10	1.5	2.6	190	44	19	
4L MLB	95 ± 35	1.8	2.5	200	20	30	9
(EXT P/G)§	85 ± 30	1.8	2.5	200	21	16	
6L MLB	75 ± 30	1.8	2.5	200	40	32	10
(EXT P/G)§	70 ± 35	1.8	2.5	200	46	16	
6L MLB	68 ± 3	1.9	1.8	278	0.5	20	11
(INT P/G)§	61 ± 3	1.9	1.8	278	0.5	15	
6L MLB (INT P/G, Surface Routing)§	85 ± 25	1.5 (surface), 1.8	1.8	278	22	16	12
	75 ± 15	1.5 (surface), 1.8	1.8	278	26	14	
8L MLB	85 ± 25	1.9	1.8	278	20	18	13
(INT P/G)§	75 ± 15	1.9	1.8	278	24	12	

* Includes the effect of 963 connector plus fanout; see Fig. 1.

† Maximum pulse crosstalk occurs when the round trip propagation delay over the coupled length is at least as great as the signal rise time. See Section 4.2.

‡ The first entry applies to Milene (registered trademark of W. L. Gore & Assoc., Inc.) insulation, the second to Teflon (registered trademark of E. I. DuPont) insulation.

§ The first entry applies to conductor width = 8 mils, conductor space = 9 mils, the second to 12, 13 mils.

accurate expression for V_c is obtained by applying circuit theory to the elemental circuit in Fig. 3a. The result is that V_c satisfies

$$\frac{dV_c}{dt} + \frac{V_c}{Z_1C_m} = \frac{1}{2}\frac{\partial V(t - (x/v))}{\partial t} \tag{2}$$

or

$$V_c = \frac{1}{2}\int_{(x/v)}^{t} e^{-\frac{(t-\xi)}{Z_1C_m}} \frac{\partial V(\xi - (x/v))}{\partial \xi}\, d\xi. \tag{3}$$

When the conductors are loosely coupled, C_m is relatively small, and eq. (3) yields the approximation given in Fig. 3a, since

$$V_c = \frac{Z_1C_m}{2}\int_{(x/v)}^{t} \frac{e^{-\frac{(t-\xi)}{Z_1C_m}}}{Z_1C_m} \frac{\partial V(\xi - (x/v))}{\partial \xi}\, d\xi \sim \frac{Z_1C_m}{2}\frac{\partial V(t - (x/v))}{\partial t}. \tag{4}$$

The loose coupling approximation not only allows the simplification of V_c but also allows one to neglect the interaction of the idle conductor on the driven conductor. When this interaction is considered along with conductor losses, the analysis becomes extremely difficult (see, for example, Refs. 7 and 8).

Using this simplified model, the total near-end (backward) crosstalk waveform, $V_{ne}(t)$, and the total far-end (forward) crosstalk waveform, $V_{fe}(t)$, can be expressed as two independent differential equations:

$$dV_{ne}(t) = \frac{1}{2}\left(Z_1C_m + \frac{L_m}{Z_1}\right)dx \frac{\partial V(t - (2x/v))}{\partial t} \tag{5}$$

$$dV_{fe}(t) = \frac{1}{2}\left(Z_1C_m - \frac{L_m}{Z_1}\right)dx \frac{dV(t - (l_c/v))}{dt}. \tag{6}$$

By integrating the variable x over the coupled length l_c, we have that

$$V_{ne}(t) = \frac{1}{2}\left(Z_1C_m + \frac{L_m}{Z_1}\right)\int_0^{l_c} \frac{\partial V(t - (2x/v))}{\partial t}\, dx \tag{7}$$

$$= K_{ne}[V(t) - V(t - 2T_D)], \tag{8}$$

where

$$T_D = \frac{l_c}{v} = \text{propagation delay over the coupled length}$$

$$K_{ne} = \frac{v}{4}\left[Z_1C_m + \frac{L_m}{Z_1}\right].$$

Similarly,

$$V_{fe}(t) = \frac{1}{2}\left(Z_1C_m - \frac{L_m}{Z_1}\right)\int_0^{l_c} \frac{dV(t - T_D)}{dt}\,dx \tag{9}$$

$$= K_{fe}l_c\frac{dV(t - T_D)}{dt}, \tag{10}$$

where

$$K_{fe} = \frac{1}{2}\left(Z_1C_m - \frac{L_m}{Z_1}\right).$$

Equations (8) and (10) agree with the earlier results presented in Refs. 3, 4, 9, 10, 11, and 12. These references also contain some useful discussions of crosstalk associated with printed wiring interconnections.

Notice that, if $Z_1C_m = (L_m/Z_1)$, $K_{fe} \equiv 0$ and $V_{fe}(t) = 0$. This result forms the basis of the design of directional couplers and occurs quite naturally whenever the conductors are surrounded by a homogeneous medium. See Ref. 13 for a discussion of this interesting point. However, for all the CPS considered in this paper, it turns out that $V_{fe}(t) \neq 0$.

The simplified model presented in Fig. 3 can be generalized to include the case when the driven conductor has characteristic impedance Z_1 and propagation velocity v_1 while the idle conductor has characteristic impedance Z_2 and propagation velocity v_2. For this case, (5) and (6) become:

$$dV_{ne}(t) = \frac{1}{2}\left(Z_2C_m + \frac{L_m}{Z_1}\right)dx\frac{\partial V\left(t - \dfrac{x}{v_1} - \dfrac{x}{v_2}\right)}{\partial t} \tag{11}$$

$$dV_{fe}(t) = \frac{1}{2}\left(Z_2C_m - \frac{L_m}{Z_1}\right)dx\frac{\partial V\left[t - \dfrac{x}{v_1} - (l_c - x)/v_2\right]}{\partial t}. \tag{12}$$

By integrating the variable x over the coupled length l_c, we have

$$V_{ne}(t) = \frac{1}{2}\left(Z_2C_m + \frac{L_m}{Z_1}\right)\left(\frac{v_1v_2}{v_1 + v_2}\right) \cdot\left\{V(t) - V\left[t - l_c\left(\frac{v_1 + v_2}{v_1v_2}\right)\right]\right\} \tag{13}$$

$$V_{fe}(t) = \frac{1}{2}\left(Z_2C_m - \frac{L_m}{Z_1}\right)\left(\frac{v_1v_2}{v_2 - v_1}\right) \cdot\left\{V\left(t - \frac{l_c}{v_2}\right) - V\left(t - \frac{l_c}{v_1}\right)\right\}. \tag{14}$$

Equations (13) and (14) agree with the results given in Ref. 11, and they reduce to (8) and (10) when $Z_2 = Z_1$ and $v_1 = v_2 = v$.

The corresponding results for the case when the driven conductor has Z_2, v_2 and the idle conductor has Z_1, v_1 can be obtained from eqs. (13) and (14) merely by interchanging Z_1 and Z_2 and also v_1 and v_2. In this manner, one can determine the following general result:

$$\frac{V_{ne}(t, Z_2, v_2)}{V_{ne}(t, Z_1, v_1)} = \frac{V_{fe}(t, Z_2, v_2)}{V_{fe}(t, Z_1, v_1)} = \frac{Z_2}{Z_1}, \tag{15}$$

where

$V_{ne}(t, Z_i, v_i)$ = near-end crosstalk waveform when the idle conductor has Z_i, v_i,

and

$V_{fe}(t, Z_i, v_i)$ = far-end crosstalk waveform when the idle conductor has Z_i, v_i.

Notice that eq. (15) is independent of time and the propagation velocities. Also, it can be shown that (15) satisfies reciprocity.

In CP design, one usually attempts to make the characteristic impedance constant throughout the CP or $Z_1 = Z_2$. However, if $Z_1 \neq Z_2$ (as it can be when dealing with interlayer crosstalk), then eq. (15) shows that both near-end and far-end crosstalk are reduced when the conductor having the lower characteristic impedance is taken as the idle conductor.

Although eqs. (13) and (14) are more general, experimental work has shown that eqs. (8) and (10) or, more generally, eqs. (13) and (14) with $v_1 = v_2 = v$ are sufficient for characterizing the crosstalk on all the CP styles of interest in this paper. Also, in order to help simplify the tables in the appendix, we shall only report on the average interlayer crosstalk associated with a given conductor pair. This appears to be sufficient, since interlayer crosstalk is usually of less concern than intralayer crosstalk.

The results based on the simplified model given in Fig. 3 turn out to be good approximations for printed wiring boards when the value of K_{ne} is less than about 25 percent. However, even when K_{ne} is somewhat greater than 25 percent, the results based on the simplified model can still be applied, although they become less accurate in this region.

On all styles of CPs, we have found experimentally that max $|V_{fe}(t)|$ < max $V_{ne}(t)$ for all signals and coupled lengths of interest* in this paper. Thus, by controlling $V_{ne}(t)$, one also controls $V_{fe}(t)$. Accordingly, we have directed our experimental work toward estimating the magnitude of the near-end crosstalk and only provide experimental bounds on the intralayer far-end crosstalk for all the CP styles.

---

* Because of connector limitations, the signal rise times of interest are 2 ns or more (i.e., a signal bandwidth of 175 MHz or less). The coupled lengths of interest are all less than 18 inches.

4.2 Crosstalk resulting from a pulse signal

Let $V(t)$ represent a ramp type of pulse signal given by:

$$V(t) = \begin{cases} \dfrac{V_o t}{T_R}, & 0 \le t \le T_R \\ V_o, & t > T_R. \end{cases} \tag{16}$$

When $V_o > 0$, $V(t)$ represents a rising step signal having a 100 percent rise time of T_R. This type of signal is convenient for characterizing the crosstalk resulting from the leading edge of a pulse signal.

In practice, the total near-end crosstalk, NEXT, is usually defined as the fraction of the pulse drive signal that appears at the near-end of the idle conductor. Thus, for the pulse signal, eq. (8) yields:

$$\text{NEXT} = \frac{\max V_{ne}(t)}{V_0} = \begin{cases} K_{ne}, & 2T_D > T_R \\ K_{ne}\left(\dfrac{2T_D}{T_R}\right), & 2T_D \le T_R. \end{cases} \tag{17}$$

When $2T_D > T_R$, the near-end waveform, $V_{ne}(t)$, is a trapezoidal pulse and when $2T_D \le T_R$, this waveform is a triangular pulse.

Equation (17) shows that the value of K_{ne} represents the maximum value of near-end pulse crosstalk. In the appendix, the experimental values of K_{ne} and $1/v = T_D/l_c$ for all CPs of interest in this paper are tabulated in Tables A and B of Figs. 4 through 13. By using these tabulated values and eq. (17), one can readily estimate the NEXT for an arbitrary pulse-like signal on any CP style.

As discussed in Section 4.1, only the average values of K_{ne} for interlayer, near-end crosstalk are tabulated. To estimate the two individual values of K_{ne} for interlayer, near-end crosstalk, it can be shown that each K_{ne} value must be multiplied by $\sqrt{Z_1/Z_2}$ and $\sqrt{Z_2/Z_1}$. The values of Z_1, Z_2, the characteristic impedances of the conductors, are also tabulated in the appendix.

The corresponding result for the total far-end crosstalk, FEXT, can be obtained from eq. (10):

$$\text{FEXT} = \frac{\max |V_{fe}(t)|}{V_o} = \frac{|K_{fe}|\, l_c}{T_R}. \tag{18}$$

In this case, the far-end crosstalk waveform, $V_{fe}(t)$, is a rectangular pulse.

For all the CP styles, we have determined experimentally that $|K_{fe}| \le 0.09$ ns/ft for intralayer crosstalk. We shall see that this result can be used to bound intralayer FEXT on all the CPs.

4.3 Crosstalk resulting from a periodic signal

If $V(t)$ represents a periodic signal of period $T = 1/f_o$, then

$$V(t) = \sum_{n=-\infty}^{\infty} \alpha_n e^{i\omega_n t}, \tag{19}$$

where

$$\alpha_n = \frac{1}{T}\int_{-T/2}^{T/2} V(t) e^{-i\omega_n t}\, dt$$

and

$$\omega_n = n2\pi f_o.$$

For this periodic signal, eq. (8) yields

$$V_{ne}(t) = K_{ne} \sum_{n=-\infty}^{\infty} (2i\alpha_n \sin \omega_n T_D) e^{i\omega_n (t-T_D)}. \tag{20}$$

If we now define near-end crosstalk, NEXT, as

$$\text{NEXT} \equiv \left[\frac{\text{ac power of } V_{ne}(t)}{\text{ac power of } V(t)}\right]^{1/2}, \tag{21}$$

then

$$\text{NEXT} = 2K_{ne}\left[\frac{\sum_{n=1}^{\infty} |\alpha_n \sin \omega_n T_D|^2}{\sum_{n=1}^{\infty} |\alpha_n|^2}\right]^{1/2} \le 2K_{ne}. \tag{22}$$

Equation (22) shows that NEXT $\le 2K_{ne}$ for all periodic signals.

The corresponding result for FEXT, assuming no jump discontinuities in $V(t)$, is

$$V_{fe}(t) = K_{fe} l_c \sum_{n=-\infty}^{\infty} i\alpha_n \omega_n e^{i\omega_n (t-T_D)} \tag{23}$$

and

$$\text{FEXT} \equiv \left[\frac{\text{ac power of } V_{fe}(t)}{\text{ac power of } V(t)}\right]^{1/2} \tag{24}$$

$$= |K_{fe}|\, l_c \left[\frac{\sum_{n=1}^{\infty} |\alpha_n \omega_n|^2}{\sum_{n=1}^{\infty} |\alpha_n|^2}\right]^{1/2}. \tag{25}$$

By using the tabulated values of K_{ne} and $1/v = T_D/l_c$ given in the appendix together with eq. (22), one can estimate the NEXT resulting from a general periodic signal on any of the CPS. Also, by using the bound on $|K_{fe}|$ given in Section 4.2 along with eq. (25), one can bound the intralayer FEXT on any of the CPS.

As an example of a simple periodic signal, let $V(t)$ represent a sinusoid of frequency f_o. Then eqs. (22) and (25) yield

$$\text{NEXT} = 2K_{ne}|\sin 2\pi f_o T_D| \tag{26}$$

$$\text{FEXT} = |K_{fe}|\, l_c 2\pi f_o. \tag{27}$$

When $f_o = (4T_D)^{-1}$, NEXT attains its maximum value of $2K_{ne}$, which is twice the maximum NEXT resulting from the pulse signal considered in Section 4.2.

It can be shown that eqs. (26) and (27) are special cases of the more general results presented in the classical works on sinusoidal crosstalk presented in Refs. 14 and 15. These references also include the effects of conductor losses. In our application, the coupled length, l_c, is relatively short ($l_c \le 18''$), so that conductor losses are negligible over a frequency range of about 250 MHz.

For small values of $f_oT_D(= f_ol_c/v)$, eq. (26) yields

$$\text{NEXT} = 4\pi K_{ne} f_o T_D = 4\pi K_{ne}\frac{f_o l_c}{v}. \tag{28}$$

In this case, eq. (28) shows that NEXT is proportional to both frequency, f_o, and coupled length l_c much as is FEXT.

4.4 Crosstalk resulting from a random signal

Let $V(t)$ represent a differentiable, stationary random signal having zero mean and one-sided power spectral density $W(f)$. The correlation function, $\rho(\tau)$, of the random signal is defined by

$$\rho(\tau) = E[V(t)V(t+\tau)] = \int_0^\infty W(f)\cos 2\pi f\tau\, df, \tag{29}$$

where E = expectation operator.

The correlation function, $\rho_{ne}(\tau)$, of the crosstalk waveform at the near-end of the idle conductor can be determined from eq. (8). Thus,

$$\begin{aligned}\rho_{ne}(\tau) &= E[V_{ne}(t)V_{ne}(t+\tau)]\\ &= K_{ne}^2[2\rho(\tau) - \rho(\tau - 2T_D) - \rho(\tau + 2T_D)].\end{aligned} \tag{30}$$

The power spectral density, $W_{ne}(f)$, of $V_{ne}(t)$ is given by

$$W_{ne}(f) = 4\int_0^\infty \rho_{ne}(\tau)\cos 2\pi f\tau\, d\tau \tag{31}$$

$$= 4K_{ne}^2 W(f)\sin^2 2\pi f T_D. \tag{32}$$

For this random signal case, it is reasonable to define the NEXT by

$$\text{NEXT} = \frac{\sigma_{ne}}{\sigma}, \tag{33}$$

where

$$\sigma_{ne} = \text{rms value of } V_{ne}(t)$$

$$\sigma = \text{rms value of } V(t).$$

Thus,

$$\text{NEXT} = \frac{\sigma_{ne}}{\sigma} = \sqrt{\frac{\rho_{ne}(0)}{\rho(0)}} \tag{34}$$

$$= \sqrt{2}\,K_{ne}\left[1 - \frac{\rho(2T_D)}{\sigma^2}\right]^{1/2} \le 2K_{ne}. \tag{35}$$

Equation (35) shows that NEXT is bounded by $2K_{ne}$ for all stationary random signals.

The corresponding results at the far end are

$$\rho_{fe}(\tau) = E[V_{fe}(t)V_{fe}(t+\tau)] = -|K_{fe}|^2 l_c^2 \rho''(\tau) \tag{36}$$

$$W_{fe}(f) = [|K_{fe}|\, l_c(2\pi f)]^2\, W(f) \tag{37}$$

and

$$\text{FEXT} = \frac{\sigma_{fe}}{\sigma} = |K_{fe}|\, l_c \sqrt{\frac{-\rho''(0)}{\rho(0)}} \tag{38}$$

$$= |K_{fe}|\, l_c \pi \beta, \tag{39}$$

where

σ_{fe} = rms value of $V_{fe}(t)$
β = average number of zero crossings per second of $V(t)$.

Thus, for all differentiable, stationary random signals FEXT is proportional to the average number of zero crossings per second of $V(t)$.

By using the tabulated values of K_{ne} and $1/v (= T_D/l_c)$ given in the appendix together with eq. (35), one can estimate the NEXT resulting from a general random signal on any of the CPS. Also, by using the bound on $|K_{fe}|$ given in Section 4.2 along with eq. (38), one can bound the intralayer FEXT on any of the CPS.

As an example of a random signal, let

$$W(f) = \begin{cases} \dfrac{\sigma^2}{B}, & f_o - \dfrac{B}{2} \le f \le f_o + \dfrac{B}{2} \\ 0, & \text{otherwise,} \end{cases} \tag{40}$$

where

B = bandwidth of the signal $V(t)$

f_o = center frequency of the signal $V(t)$.

For this case, eqs. (29) and (35) yield

$$\text{NEXT} = \frac{\sigma_{ne}}{\sigma} = \sqrt{2} K_{ne} \left[1 - \left(\frac{\sin 2\pi B T_D}{2\pi B T_D} \right) \cos 4\pi f_o T_D \right]^{1/2}. \tag{41}$$

Notice that, as $B \to 0$, eq. (41) approaches eq. (26), the corresponding result for the sine wave case.

The result for FEXT is

$$\text{FEXT} = \frac{\sigma_{fe}}{\sigma} = |K_{fe}| \, l_c \pi \sqrt{4f_0^2 + B^2/3}. \tag{42}$$

As $B \to 0$, this result approaches eq. (27), the corresponding result for the sine wave case.

The theoretical developments in Sections 4.2, 4.3, and 4.4 can be generalized to include eqs. (13) and (14) in place of eqs. (8) and (10). When $v_1 = v_2 = v$, all one needs to do is replace Z_1C_m by Z_2C_m in K_{ne} and K_{fe}. The more general case, $v_1 \neq v_2$, will not be treated in this paper, since experimental results show that the propagation velocity is approximately constant on a given CP.

V. SOME APPLICATIONS

5.1 *Selection of a CP style*

Since the costs associated with the various CP styles differ significantly,[1] it is very important to select a CP style which is both suitable electrically and relatively inexpensive. The pulse transmission properties summarized in Table II and tabulated in more detail in the appendix can be used to help select such a cost-effective CP for a given application.

It is also very important that the physical designers and systems designers using *BELLPAC* hardware be aware of these basic pulse transmission properties. The CP transmission properties must be compatible with the transmission properties of the backplane, frame wiring, and the CP components.

5.2 *Estimation of crosstalk on a given CP style*

By using the theoretical results presented in Section IV together with the appropriate K_{ne} and $1/v$ values given in the appendix, one can estimate the amount of near-end crosstalk for fine line conductors carrying a wide variety of signals on any of the CPs considered in this paper. As discussed in Section IV, far-end crosstalk is always less than near-end crosstalk, usually much less. Also, intralayer, far-end crosstalk can be bounded by using the experimentally determined constant $|K_{fe}| \leq 0.09$ ns/ft and the theoretical results presented in Section IV.

Let us consider as an example a pair of adjacent, parallel conductors on the inside signal layer of the 6L MLB (INT P/G, surface routing). From Table B of Figure 12 in the appendix, we see that $K_{ne} = 0.16$ for two adjacent conductors $(Y_1 Y_2)$ in the 200-mil channel when the conductor width and conductor spacing are 8 and 9 mils, respectively. Table A of this same figure gives $1/v = 1.8$ ns/ft. Thus, for a pulse signal, eq. (17) yields

$$\text{NEXT} = \begin{cases} 0.16, & 2T_D > T_R \\ (0.16)\left(\dfrac{2T_D}{T_R}\right), & 2T_D \leq T_R, \end{cases} \tag{43}$$

where

$T_D = \dfrac{l_c}{v}$ = propagation delay over the coupled length (ns)

l_c = coupled length (ft)

T_R = rise time of the pulse signal (ns).

Also, for the pulse signal, eq. (18) yields

$$\text{FEXT} \leq (0.09)\,\frac{l_c}{T_R}. \tag{44}$$

Similarly, for a sine wave signal of frequency f_o, eqs. (26) and (27) yield

$$\text{NEXT} = (2)(0.16)\,|\sin 2\pi f_o T_D| \tag{45}$$

$$\text{FEXT} \leq (0.09)\, l_c 2\pi f_o. \tag{46}$$

In a very similar manner, one can also estimate the NEXT and bound the intralayer FEXT for an arbitrary periodic or random signal by using eqs. (22), (25), (35), and (39).

By using this method, one can estimate the NEXT and bound the FEXT for a wide variety of conductor pairs and a wide variety of signal types on any of the CPs considered in this paper.

For a required crosstalk constraint, the theoretical and experimental crosstalk results can be used to help determine routing restrictions on coupled length for general types of signals. Alternately, this information can be incorporated into computer-aided designs to help determine whether a routed CP has violated a given crosstalk constraint associated with a particular signal type. In this manner, a routed CP can be analyzed to detect potential crosstalk problems before the CP routing is finalized for manufacture.

As a final point concerning the estimate of crosstalk, one can also estimate intralayer NEXT for a pair of adjacent, parallel conductors having a range of conductor spacings. It turns out that intralayer NEXT is essentially independent of conductor width (see Ref. 4). Accordingly, to estimate the value of $K_{ne}(S)$ for a pair of adjacent, parallel conductors (i.e., Y_1Y_2) having conductor spacing S, one can interpolate or extrapolate the values of K_{ne} for $S = 9$ mils or 13 mils given in the appendix by assuming that $K_{ne}(S)$ is proportional to $1/S$. It can be shown that this is a satisfactory assumption when 7 mils $\leq S \leq$ 40 mils, the region of most interest in this paper.

As an example, let us apply this method to a pair of adjacent parallel conductors having conductor spacing S (mils) on the inside signal layer of the 6L MLB (INT P/G, surface routing). For the 200-mil channel, Table B of Fig. 12 yields the following minimum mean square error estimate:

$$K_{ne}(S) = (9)(13)\,\frac{[13K_{ne}(9) + 9K_{ne}(13)]}{(9^2 + 13^2)S} = \frac{147.9}{S}\,\%. \tag{47}$$

This method can be applied to pairs of adjacent, parallel conductors on any CP considered in this paper.

5.3 Electrical comparison of the CPs

The results in Table II and the appendix can be used to compare the various CPs from the electrical point of view. For example, Table II shows that, of the three CPs containing only two layers of metallization, namely, the double-sided epoxy, the double-sided metal, and the bonded board, the double-sided epoxy board is inferior to the other two. It has a relatively high characteristic impedance and higher values of intralayer crosstalk. Recall that intralayer crosstalk is more troublesome than interlayer crosstalk, which can be reduced considerably by using orthogonal routing on adjacent layers.

Also, the double-sided metal board is somewhat better electrically than the bonded board because the impedance variations and crosstalk are less for the metal board.

Table II also shows that the MLBs having an internal power and ground plane (INT P/G) are superior electrically to those having an external power and ground plane (EXT P/G). The MLBs having (INT P/G) have less impedance variations and yield less intralayer crosstalk.

Notice from Table II that a wire-wrap CP and the double-sided (epoxy) CP are both inferior to the MLB styles from the electrical point of view. Also, the double-sided (metal) and the bonded board have electrical properties which are comparable to all the MLBs having (INT P/G).

Finally, the extender board, because of its special design, is clearly the best electrical design of all the CPs considered in this paper. It has relatively little variation in characteristic impedance and very low crosstalk.

5.4 Estimation of the capacitance and inductance of the conductors

In certain applications of the CPs, it is important to have an estimate of the value of C, the capacitance per unit length, and L, the inductance per unit length for the conductors on all of the CP styles. This information is important, for example, when one needs to estimate the electrical load on a driver circuit for certain ranges of frequency or rise times. The values of C and L can be estimated from the values of propagation delay per foot $(1/v)$ and characteristic impedance Z_1 given in the appendix for each CP style. Using these values, C and L are given by

$$C = \frac{(1/v)}{Z_1} \frac{nf}{ft} \tag{48}$$

$$L = \left(\frac{1}{v}\right) Z_1 \frac{nh}{ft}. \tag{49}$$

For worst case estimates, $1/v$ should be increased by about 10 percent, since the values listed in the appendix are averages over about 20 different conductor paths on each CP.

5.5 Generalization to other dielectric materials

If eqs. (48) and (49) are used in eq. (8) to reduce K_{ne}, we have

$$K_{ne} = \frac{1}{4}\left[\frac{C_m}{C} + \frac{L_m}{L}\right]. \tag{50}$$

Equation (50) shows that K_{ne} is independent of the relative dielectric constant, ϵ_r (effective). It can also be shown that the more general K_{ne} discussed at the end of Section 4.4 is also independent of the relative dielectric constant. Thus, the values of K_{ne} given in the appendix apply when the CPs are fabricated with any dielectric material.

One can also show that the propagation delay per foot, $1/v$, and the far-end crosstalk coefficient $|K_{fe}|$ are both proportional to $\sqrt{\epsilon_r}$, while the characteristic impedance, Z_1, is inversely proportional to $\sqrt{\epsilon_r}$. Thus, many of the results in this paper can be applied when the CPs are fabricated with other dielectric materials such as ceramic, Teflon, or polyimide.

5.6 Electrical characterization of backplanes

In the physical design of large electronic systems, various styles of printed wiring-board backplanes are often used to interconnect CPs.

These backplanes are usually very similar to some CP styles considered in this paper. Accordingly, many results in this paper can be applied to help electrically characterize various styles of backplanes.

VI. SUMMARY

A Bell System packaging effort (*BELLPAC* packaging system) is now under way to develop a modular packaging system for packaging electronic equipment. This effort makes use of a suitable connector (963) and a number of circuit pack (CP) styles (ranging from wire-wrap CPS to multilayer board CPS) which have common features suitable for computer-aided design.

This paper presents some experimental results concerning the pulse transmission properties of fine line printed conductors (e.g., width = 8 mils, spaces = 9 mils) on various styles of CPS which include those in the *BELLPAC* hardware family of CPS. The pulse transmission properties include the characteristic impedance, the propagation delay, the rise time, the bandwidth, and the intralayer and interlayer pulse crosstalk. Theoretical scaling laws are developed to extend the application of the experimental crosstalk results to conductor spaces in the range of 7 to 40 mils.

A simplified theoretical model is presented which leads, directly, to some basic crosstalk equations. Also, theoretical results are developed to extend the application of the experimental crosstalk results to arbitrary pulse signals, periodic signals, and random signals.

The results in this paper can be applied to the:

(*i*) Selection of a CP style for a given application.
(*ii*) Estimation of crosstalk on a given CP style.
(*iii*) Comparison of the electrical properties of the CP styles.
(*iv*) Estimation of the capacitance and inductance of the conductors.
(*v*) Determination of the pulse transmission properties of the CP styles with various dielectrics.
(*vi*) Electrical characterization of various styles of backplanes.

The crosstalk results are very important since they tend to limit the packaging density of printed conductors on the CP styles by limiting the coupled length and spacing of parallel conductors.

VII. ACKNOWLEDGMENTS

In the course of carrying out this program, the author received valuable support from A. G. Lubowe, A. P. Irwin, J. J. Waltz, H. B. Koons, M. P. Lum, W. H. Knausenberger, R. J. Stanzione, B. C. Fichter, R. A. Davis, and D. Dinella. The author also wishes to thank J. G. Brinsfield for some initial encouragement.

APPENDIX

Experimental Results

Index to pulse transmission properties

Circuit Pack Style	Figure No. Containing the Pulse Transmission Properties
Wire wrap	4
Extender board	5
Double-sided (epoxy)	6
Double-sided (metal)	7
Bonded board (LAMPAC)	8
4L MLB (EXT P/G)	9
6L MLB (EXT P/G)	10
6L MLB (INT P/G)	11
6L MLB (INT P/G, surface routing)	12
8L MLB (INT P/G)	13

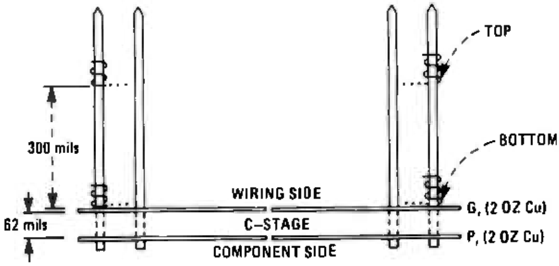

LAYUP FOR THE WIRE WRAP BOARD

TABLE A
PULSE TRANSMISSION PROPERTIES OF THE WIRE WRAP BOARD

	AWG 30 WITH MILENE INSULATION		AWG 30 WITH TEFLON INSULATION	
	LOCATION OF WRAP ON PIN	CHARACTERISTIC IMPEDANCE (OHMS)	LOCATION OF WRAP ON PIN	CHARACTERISTIC IMPEDANCE (OHMS)
ROUTING IN 200 mil CHANNELS(1)	TOP	175 OHMS	TOP	194 OHMS
	BOTTOM	78	BOTTOM	124
ROUTING IN 100 mil CHANNELS	TOP	158	TOP	164
	BOTTOM	117	BOTTOM	138

- ● PROPAGATION DELAY = 1.4 ns/ft. (=1/v, MILENE), 1.3 ns/ft. (=1/v, TEFLON).
- ● 80% RISE TIME ON TDR FOR 1 ft CONDUCTOR LENGTH = 2.0 ns (MILENE) 1.8 ns (TEFLON).
- ● BANDWIDTH FOR 1 ft CONDUCTOR LENGTH = 250 MHz (MILENE), 278 MHz (TEFLON).

(1) THE 200 mil CHANNEL ALSO CONTAINS A GROUND PLANE.

TABLE B
K_{ne} = MAXIMUM NEAR–END PULSE CROSSTALK(1) FOR VARIOUS WIRE PAIRS ON THE WIRE WRAP BOARD

	AWG 30 WITH MILENE INSULATION		AWG 30 WITH TEFLON INSULATION	
	LOCATION OF WRAP ON PIN	CROSSTALK (TIGHTLY COUPLED PAIRS)	LOCATION OF WRAP ON PIN	CROSSTALK (TIGHTLY COUPLED PAIRS)
ROUTING IN 200 mil CHANNELS(2)	TOP	40 %	TOP	35 %
	BOTTOM	16	BOTTOM	23
ROUTING IN 100 mil CHANNELS	TOP	28	TOP	36
	BOTTOM	23	BOTTOM	13

(1) CROSSTALK WAS MEASURED AS A PERCENTAGE OF THE INPUT STEP.

(2) THE 200 mil CHANNEL ALSO CONTAINS A GROUND PLANE.

Fig. 4—Impedance, propagation delay, rise time, bandwidth, and pulse crosstalk for the wire-wrap board with 963C-100 connectors.

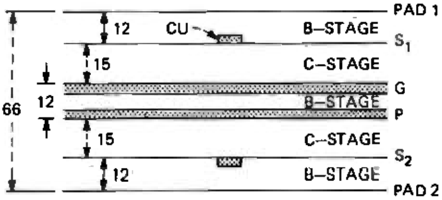

- 2 OZ CU CONDUCTORS
- ALL DIMENSIONS IN MILS

(a) NOTATION FOR INTERLAYER CROSSTALK ON THE EXTENDER BOARD.

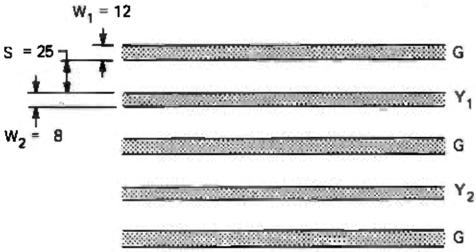

(b) NOTATION ~~FOR~~ INTRALAYER CROSSTALK ON THE EXTENDER BOARD.

ELECTRICAL CHARACTERISTICS OF LARGEST (7.67" X 14.78") EXTENDER BOARD (WITH 963C CONNECTORS)

- CHARACTERISTIC IMPEDANCE = 70 ± 5 OHMS.
- PROPAGATION DELAY = 1.80 ns/ft.
- 80 % RISE TIME ON TDR = 1.3 ns.
- BANDWIDTH = 385 MHz.
- MAXIMUM INTRALAYER NEXT: Y_1 Y_2 = 1.6 %
- MAXIMUM INTERLAYER NEXT: S_1 S_2 = 0.3 %

Fig. 5—Impedance, propagation delay, rise time, bandwidth, and pulse crosstalk for the extender board with 963C-100 connectors.

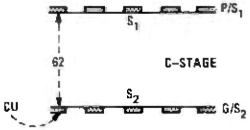

• 2 OZ CONDUCTORS • ALL DIMENSIONS IN MILS
(a) NOTATION FOR INTERLAYER CROSSTALK ON THE DOUBLE SIDED EPOXY PWB.

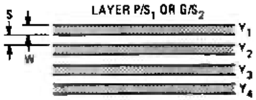

(b) NOTATION FOR INTRALAYER CROSSTALK W = 12, S = 13 MILS OR W = 8, S = 9 MILS.

TABLE A
PULSE TRANSMISSION PROPERTIES OF THE DOUBLE-SIDED EPOXY PWB[3]

	CONDUCTOR WIDTH = 12 mils CONDUCTOR SPACING = 13 mils		CONDUCTOR WIDTH = 8 mils CONDUCTOR SPACING = 9 mils	
	SIGNAL LAYER	CHARACTERISTIC IMPEDANCE (OHMS)	SIGNAL LAYER	CHARACTERISTIC IMPEDANCE (OHMS)
ROUTING IN 200 mil CHANNELS[2]	P/S$_1$	163 OHMS	P/S$_1$	158 OHMS
	G/S$_2$	166	G/S$_2$	163
	P/S$_1$ → G/S$_2$[1]	146	P/S$_1$ → G/S$_2$	150
ROUTING IN 100 mil CHANNELS	P/S$_1$	142	P/S$_1$	142
	G/S$_2$	135	G/S$_2$	146
	P/S$_1$ → G/S$_2$	129	P/S$_1$ → G/S$_2$	129

- PROPAGATION DELAY = 1.5 ns/ft. (=1/v).
- 80% RISE TIME ON TDR FOR 1ft CONDUCTOR LENGTH = 2.6 ns.
- BANDWIDTH FOR 1ft CONDUCTOR LENGTH = 190 MHz.

(1) THE TRANSITIONS FROM P/S$_1$ TO G/S$_2$ USED 10 VIAS.

(2) THE P/G ROUTING ALSO OCCUPIES THE 200 mil CHANNELS.

(3) NO COVERCOAT CASE. COVERCOAT (GFR) HAS NEGLIGIBLE EFFECT ON RISE TIME (OR BANDWIDTH) BUT DECREASES THE CHARACTERISTIC IMPEDANCE BY ABOUT 5% AND INCREASES THE PROPAGATION DELAY BY ABOUT 10%.

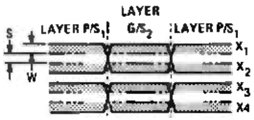

(c) NOTATION FOR CROSSTALK BETWEEN CONDUCTORS WHICH APPEAR ALTERNATELY ON LAYERS P/S$_1$ AND G/S$_2$.
W = 12, S = 13 MILS OR W = 8, S = 9 MILS.

TABLE B
K_{ne} = MAXIMUM NEAR-END PULSE CROSSTALK[1] FOR VARIOUS CONDUCTOR PAIRS ON THE DOUBLE-SIDED EPOXY PWB[3]

CONDUCTOR WIDTH = 12 mils, CONDUCTOR SPACING = 13 mils

	INTERLAYER	INTRALAYER				ALTERNATELY ON P/S$_1$, G/S$_2$		
LOCATION OF ROUTING	S$_2$ S$_1$	LAYER	Y$_1$ Y$_2$	Y$_1$ Y$_3$	Y$_1$ Y$_4$	X$_1$ X$_2$	X$_1$ X$_3$	X$_1$ X$_4$
200 mil CHANNEL[2]	24%	P/S$_1$	34%	12%	8.0%	32%	20%	20%
		G/S$_2$	34	12	8.0			
100 mil CHANNEL	19	P/S$_1$	—	—	—	—	—	—
		G/S$_2$	—	—	—			

CONDUCTOR WIDTH = 8 mils, CONDUCTOR SPACING = 9 mils

	INTERLAYER	INTRALAYER				ALTERNATELY ON P/S$_1$, G/S$_2$		
LOCATION OF ROUTING	S$_2$ S$_1$	LAYER	Y$_1$ Y$_2$	Y$_1$ Y$_3$	Y$_1$ Y$_4$	X$_1$ X$_2$	X$_1$ X$_3$	X$_1$ X$_4$
200 mil CHANNEL	21%	P/S$_1$	39%	17%	10%	34%	22%	22%
		G/S$_2$	37	16	9.2			
100 mil CHANNEL	17	P/S$_1$	32	—	—	30	—	—
		G/S$_2$	32	—	—			

(1) CROSSTALK WAS MEASURED AS A PERCENTAGE OF THE SIGNAL STEP.

(2) THE P/G ROUTING ALSO OCCUPIES THE 200 mil CHANNELS.

(3) NO COVERCOAT CASE. COVERCOAT (GFR) INCREASES CROSSTALK BY ABOUT 10% OF THE TABULATED VALUES.

Fig. 6—Impedance, propagation delay, rise time, bandwidth, and pulse crosstalk for the double-sided epoxy printed wiring board with 963C-100 connectors.

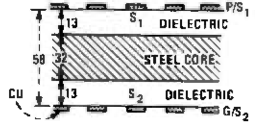

- 2 OZ CU CONDUCTORS • ALL DIMENSIONS IN MILS

(a) NOTATION FOR INTERLAYER CROSSTALK ON THE DOUBLE SIDED METAL PWB.

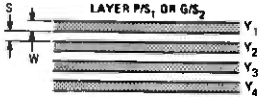

(b) NOTATION FOR INTRALAYER CROSSTALK. W = 12, S = 13 MILS OR W = 8, S = 9 MILS.

TABLE A
PULSE TRANSMISSION PROPERTIES OF THE DOUBLE-SIDED METAL PWB[3]

	CONDUCTOR WIDTH = 12 mils CONDUCTOR SPACING = 13 mils		CONDUCTOR WIDTH = 8 mils CONDUCTOR SPACING = 9 mils	
	SIGNAL LAYER	CHARACTERISTIC IMPEDANCE (OHMS)	SIGNAL LAYER	CHARACTERISTIC IMPEDANCE (OHMS)
ROUTING IN 200 mil CHANNELS[2]	P/S$_1$	89 OHMS	P/S$_1$	104 OHMS
	G/S$_2$	85	G/S$_2$	108
	P/S$_1$ → G/S$_2$[1]	77	P/S$_1$ → G/S$_2$	92
ROUTING IN 100 mil CHANNELS	P/S$_1$	87	P/S$_1$	104
	G/S$_2$	83	G/S$_2$	104
	P/S$_1$ → G/S$_2$	78	P/S$_1$ → G/S$_2$	90

- PROPAGATION DELAY = 1.5 ns/ft. (=1/v).
- 80% RISE TIME ON TDR FOR 1 ft. CONDUCTOR LENGTH = 2.6 ns.
- BANDWIDTH FOR 1 ft. CONDUCTOR LENGTH = 190 MHz.

(1) THE TRANSITIONS FROM P/S$_1$ TO G/S$_2$ USED 10 VIAS.

(2) THE P/G ROUTING ALSO OCCUPIES THE 200 mil CHANNELS.

(3) NO COVERCOAT CASE. COVERCOAT (GFR) HAS NEGLIGIBLE EFFECT ON RISE TIME (OR BANDWIDTH) BUT DECREASES THE CHARACTERISTIC IMPEDANCE BY ABOUT 5% AND INCREASES THE PROPAGATION DELAY BY ABOUT 10%.

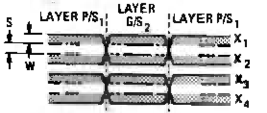

(c) NOTATION FOR CROSSTALK BETWEEN CONDUCTORS WHICH APPEAR ALTERNATELY ON LAYERS P/S$_1$ AND G/S$_2$. W = 12, S = 13 MILS OR W = 8, S = 9 MILS.

TABLE B
K_{ne} = MAXIMUM NEAR-END PULSE CROSSTALK[1] FOR VARIOUS CONDUCTOR PAIRS ON THE DOUBLE-SIDED METAL PWB[3]

CONDUCTOR WIDTH = 12 mils, CONDUCTOR SPACING = 13 mils

	INTERLAYER	INTRALAYER				ALTERNATELY ON P/S$_1$, G/S$_2$		
LOCATION OF ROUTING	$S_2 S_1$	LAYER	$Y_1 Y_2$	$Y_1 Y_3$	$Y_1 Y_4$	$X_1 X_2$	$X_1 X_3$	$X_1 X_4$
200 mil CHANNEL[2]	3.2%	P/S$_1$	13%	2.8%	0.8%	9.2%	2.4%	6.8%
		G/S$_2$	13	2.4	0.8			
100 mil CHANNEL	1.2	P/S$_1$	—	—	—	—	—	—
		G/S$_2$	—	—	—			

CONDUCTOR WIDTH = 8 mils, CONDUCTOR SPACING = 9 mils

	INTERLAYER	INTRALAYER				ALTERNATELY ON P/S$_1$, G/S$_2$		
LOCATION OF ROUTING	$S_2 S_1$	LAYER	$Y_1 Y_2$	$Y_1 Y_3$	$Y_1 Y_4$	$X_1 X_2$	$X_1 X_3$	$X_1 X_4$
200 mil CHANNEL	1.2%	P/S$_1$	15%	3.6%	1.2%	11%	3.2%	8.0%
		G/S$_2$	14	3.2	1.2			
100 mil CHANNEL	1.2	P/S$_1$	14	—	—	11	—	—
		G/S$_2$	13	—	—			

(1) CROSSTALK WAS MEASURED AS A PERCENTAGE OF THE SIGNAL STEP.

(2) THE P/G ROUTING ALSO OCCUPIES THE 200 mil CHANNELS.

(3) NO COVERCOAT CASE. COVERCOAT (GFR) INCREASES CROSSTALK BY ABOUT 10% OF THE TABULATED VALUES.

Fig. 7—Impedance, propagation delay, rise time, bandwidth, and pulse crosstalk for the double-sided metal printed wiring board with 963C-100 connectors.

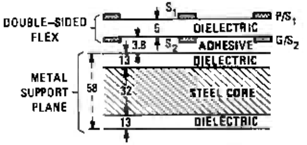

•2 OZ CU CONDUCTORS •ALL DIMENSIONS IN MILS

(a) NOTATION FOR INTERLAYER CROSSTALK ON THE BONDED BOARD.

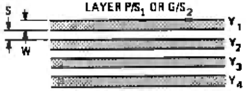

(b) NOTATION FOR INTRALAYER CROSSTALK.
W = 12, S = 13 MILS OR W = 8, S = 9 MILS.

TABLE A
PULSE TRANSMISSION PROPERTIES OF THE BONDED BOARD[3]

	CONDUCTOR WIDTH = 12 mils CONDUCTOR SPACING = 13 mils		CONDUCTOR WIDTH = 8 mils CONDUCTOR SPACING = 9 mils	
	SIGNAL LAYER	CHARACTERISTIC IMPEDANCE (OHMS)	SIGNAL LAYER	CHARACTERISTIC IMPEDANCE (OHMS)
ROUTING IN 200 mil CHANNELS[2]	P/S_1	95 OHMS	P/S_1	104 OHMS
	G/S_2	84	G/S_2	89
	$P/S_1 \rightarrow G/S_2$[1]	77	$P/S_1 \rightarrow G/S_2$	88
ROUTING IN 100 mil CHANNELS	P/S_1	89	P/S_1	102
	G/S_2	73	G/S_2	84
	$P/S_1 \rightarrow G/S_2$	82	$P/S_1 \rightarrow G/S_2$	97

- PROPAGATION DELAY = 1.5 ns/ft. (=1/v).
- 80% RISE TIME ON TDR FOR 1 ft. CONDUCTOR LENGTH = 2.8 ns.
- BANDWIDTH FOR 1 ft. CONDUCTOR LENGTH = 190 MHz.

(1) THE TRANSITIONS FROM P/S_1 TO G/S_2 USED 10 VIAS.

(2) THE P/G ROUTING ALSO OCCUPIES THE 200 mil CHANNELS.

(3) NO COVERCOAT CASE. COVERCOAT (GFR) HAS NEGLIGIBLE EFFECT ON RISE TIME (OR BANDWIDTH) BUT DECREASES THE CHARACTERISTIC IMPEDANCE BY ABOUT 5% AND INCREASES THE PROPAGATION DELAY BY ABOUT 10%.

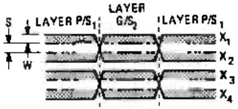

(c) NOTATION FOR CROSSTALK BETWEEN CONDUCTORS WHICH APPEAR ALTERNATELY ON LAYERS P/S_1 AND G/S_2.
W = 12, S = 13 MILS OR W = 8, S = 9 MILS.

TABLE B
K_{ne} = MAXIMUM NEAR-END PULSE CROSSTALK[1] FOR VARIOUS CONDUCTOR PAIRS ON THE BONDED BOARD[3]

CONDUCTOR WIDTH = 12 mils, CONDUCTOR SPACING = 13 mils

	INTERLAYER	INTRALAYER				ALTERNATELY ON P/S_1, G/S_2		
LOCATION OF ROUTING	$S_2 S_1$	LAYER	$Y_1 Y_2$	$Y_1 Y_3$	$Y_1 Y_4$	$X_1 X_2$	$X_1 X_3$	$X_1 X_4$
200 mil CHANNEL[2]	44%	P/S_1	19%	4.0%	1.2%	16%	6.4%	7.6%
		G/S_2	19	3.6	1.2			
100 mil CHANNEL	40	P/S_1	—	—	—	—	—	—
		G/S_2	—	—	—			

CONDUCTOR WIDTH = 8 mils, CONDUCTOR SPACING = 9 mils

	INTERLAYER	INTRALAYER				ALTERNATELY ON P/S_1, G/S_2		
LOCATION OF ROUTING	$S_2 S_1$	LAYER	$Y_1 Y_2$	$Y_1 Y_3$	$Y_1 Y_4$	$X_1 X_2$	$X_1 X_3$	$X_1 X_4$
200 mil CHANNEL	38%	P/S_1	21%	7.2%	3.2%	20%	8.4%	11%
		G/S_2	21	6.8	3.2			
100 mil CHANNEL	38	P/S_1	20	—	—	21	—	—
		G/S_2	20	—	—			

(1) CROSSTALK WAS MEASURED AS A PERCENTAGE OF THE SIGNAL STEP.

(2) THE P/G ROUTING ALSO OCCUPIES THE 200 mil CHANNELS.

(3) NO COVERCOAT CASE. COVERCOAT (GFR) INCREASES INTRALAYER CROSSTALK BY ABOUT 10% OF THE TABULATED VALUES.

Fig. 8—Impedance, propagation delay, rise time, bandwidth, and pulse crosstalk for the bonded board with 963C-100 connectors.

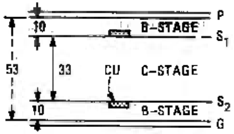

● 2 OZ CU CONDUCTORS ● ALL DIMENSIONS IN MILS

(a) NOTATION FOR INTERLAYER CROSSTALK ON THE 4L MLB (EXT P/G)

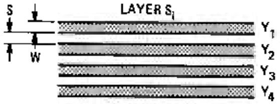

(b) NOTATION FOR INTRALAYER CROSSTALK. W = 12, S = 13 MILS OR W = 8, S = 9 MILS.

TABLE A
PULSE TRANSMISSION PROPERTIES OF THE 4L MLB (EXT P/G)

	CONDUCTOR WIDTH = 12 mils CONDUCTOR SPACING = 13 mils		CONDUCTOR WIDTH = 8 mils CONDUCTOR SPACING = 9 mils	
	SIGNAL LAYER	CHARACTERISTIC IMPEDANCE (OHMS)	SIGNAL LAYER	CHARACTERISTIC IMPEDANCE (OHMS)
ROUTING IN 200 mil CHANNELS(2)	S_1	58 OHMS	S_1	61 OHMS
	S_2	56	S_2	64
	$S_1 \rightarrow S_2$ (1)	54	$S_1 \rightarrow S_2$	64
ROUTING IN 100 mil CHANNELS	S_1	117	S_1	129
	S_2	117	S_2	129
	$S_1 \rightarrow S_2$	111	$S_1 \rightarrow S_2$	120

- PROPAGATION DELAY = 1.8 ns/ft. (=1/v).
- 80% RISE TIME ON TDR FOR 1 ft. CONDUCTOR LENGTH = 2.5 ns.
- BANDWIDTH FOR 1 ft. CONDUCTOR LENGTH = 200 MHz.

(1) THE TRANSITIONS FROM S_1 TO S_2 USED 10 VIAS.
(2) THE EXTERNAL P/G ROUTING ALSO OCCUPIES THE 200 mil CHANNELS.

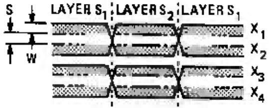

(c) NOTATION FOR CROSSTALK BETWEEN CONDUCTORS WHICH APPEAR ALTERNATELY ON LAYERS S_1 AND S_2. W = 12, S = 13 MILS OR W = 8, S = 9 MILS.

TABLE B
K_{ne} = MAXIMUM NEAR-END PULSE CROSSTALK(1) FOR VARIOUS CONDUCTOR PAIRS ON THE 4L MLB (EXT P/G)

CONDUCTOR WIDTH = 12 mils, CONDUCTOR SPACING = 13 mils

	INTERLAYER	INTRALAYER				ALTERNATELY ON S_1, S_2		
LOCATION OF ROUTING	S_2 S_1	LAYER	Y_1 Y_2	Y_1 Y_3	Y_1 Y_4	X_1 X_2	X_1 X_3	X_1 X_4
200 mil CHANNEL(2)	13%	S_1	16%	9.2%	8.4%	14%	9.0%	8.0%
		S_2	14	11	8.4			
100 mil CHANNEL	21	S_1	—	—	—	—	—	—
		S_2	—	—	—			

CONDUCTOR WIDTH = 8 mils, CONDUCTOR SPACING = 9 mils

	INTERLAYER	INTRALAYER				ALTERNATELY ON S_1, S_2		
LOCATION OF ROUTING	S_2 S_1	LAYER	Y_1 Y_2	Y_1 Y_3	Y_1 Y_4	X_1 X_2	X_1 X_3	X_1 X_4
200 mil CHANNEL	12%	S_1	16%	10%	8.4%	13%	7.2%	8.8%
		S_2	16	12	8.4			
100 mil CHANNEL	20	S_1	31	—	—	28	—	—
		S_2	30	—	—			

(1) CROSSTALK WAS MEASURED AS A PERCENTAGE OF THE SIGNAL STEP.
(2) THE EXTERNAL P/G ROUTING ALSO OCCUPIES THE 200 mil CHANNELS.

Fig. 9—Impedance, propagation delay, rise time, bandwidth, and pulse crosstalk for the 4L MLB (EXT P/G) with 963C-100 connectors.

(a) NOTATION FOR INTERLAYER CROSSTALK ON THE 6L MLB (EXT P/G)

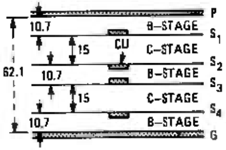

● 2 OZ CU CONDUCTORS ● ALL DIMENSIONS IN MILS

(b) NOTATION FOR INTRALAYER CROSSTALK W = 12, S = 13 MILS OR W = 8, S = 9 MILS.

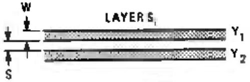

TABLE A
PULSE TRANSMISSION PROPERTIES OF THE 6L MLB (EXT P/G)

	CONDUCTOR WIDTH = 12 mils CONDUCTOR SPACING = 13 mils		CONDUCTOR WIDTH = 8 mils CONDUCTOR SPACING = 9 mils	
	SIGNAL LAYER	CHARACTERISTIC IMPEDANCE (OHMS)	SIGNAL LAYER	CHARACTERISTIC IMPEDANCE (OHMS)
ROUTING IN 200 mil CHANNELS[2]	S_1	36 OHMS	S_1	43 OHMS
	S_2	64	S_2	68
	S_3	61	S_3	62
	S_4	39	S_4	47
	$S_1 \rightarrow S_4$[1]	44	$S_1 \rightarrow S_4$	52
ROUTING IN 100 mil CHANNELS	S_1	102	S_1	104
	S_2	95	S_2	106
	S_3	95	S_3	97
	S_4	104	S_4	106
	$S_1 \rightarrow S_4$	99	$S_1 \rightarrow S_4$	103

- ● PROPAGATION DELAY = 1.8 ns/ft. (=1/v).
- ● 80% RISE TIME ON TDR FOR 1 ft. CONDUCTOR LENGTH = 2.5 ns.
- ● BANDWIDTH FOR 1 ft. CONDUCTOR LENGTH = 200 MHz.

(1) THE TRANSITIONS FROM S_1 TO S_4 USED 5 OR 10 VIAS.

(2) THE EXTERNAL P/G ROUTING ALSO OCCUPIES THE 200 mil CHANNELS.

(c) NOTATION FOR CROSSTALK BETWEEN CONDUCTORS WHICH APPEAR ALTERNATELY ON LAYERS S_1 AND S_4. W = 12, S = 13 MILS OR W = 8, S = 9 MILS.

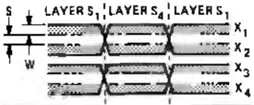

TABLE B
K_{ne} = MAXIMUM NEAR-END PULSE CROSSTALK[1] FOR VARIOUS CONDUCTOR PAIRS ON THE 6L MLB (EXT P/G)

CONDUCTOR WIDTH = 12 mils, CONDUCTOR SPACING = 13 mils

	INTERLAYER			INTRALAYER		ALTERNATELY ON S_1, S_4		
LOCATION OF ROUTING	S_2S_1	S_2S_3	S_2S_4	LAYER	Y_1Y_2	X_1X_2	X_1X_3	X_1X_4
200 mil CHANNEL[2]	12%	35%	5.0%	S_1	11%	16%	7.2%	8.0%
				S_2	14			
				S_3	16			
				S_4	16			
100 mil CHANNEL	32	46	16	S_1	—	—	—	—
				S_2	—			
				S_3	—			
				S_4	—			

CONDUCTOR WIDTH = 8 mils, CONDUCTOR SPACING = 9 mils

	INTERLAYER			INTRALAYER		ALTERNATELY ON S_1, S_4		
LOCATION OF ROUTING	S_2S_1	S_2S_3	S_2S_4	LAYER	Y_1Y_2	X_1X_2	X_1X_3	X_1X_4
200 mil CHANNEL	8.0%	30%	5.0%	S_1	17%	16%	13%	14%
				S_2	20			
				S_3	20			
				S_4	18			
100 mil CHANNEL	28	40	13	S_1	31	29	—	—
				S_2	32			
				S_3	32			
				S_4	32			

(1) CROSSTALK WAS MEASURED AS A PERCENTAGE OF THE SIGNAL STEP.

(2) THE EXTERNAL P/G ROUTING ALSO OCCUPIES THE 200 mil CHANNELS.

Fig. 10—Impedance, propagation delay, rise time, bandwidth, and pulse crosstalk for the 6L MLB (EXT P/G) with 963C-100 connectors.

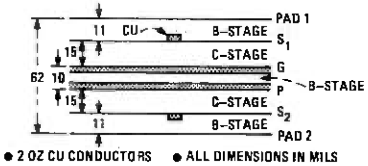

(a) NOTATION FOR INTERLAYER CROSSTALK ON THE 6L MLB (INT P/G).

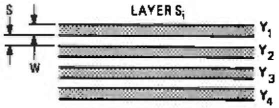

(b) NOTATION FOR INTRALAYER CROSSTALK W = 12, S = 13 MILS OR W = 8, S = 9 MILS.

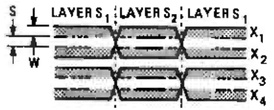

(c) NOTATION FOR CROSSTALK BETWEEN CONDUCTORS WHICH APPEAR ALTERNATELY ON LAYERS S_1 AND S_2. W = 12, S = 13 MILS OR W = 8, S = 9 MILS.

TABLE A
PULSE TRANSMISSION PROPERTIES OF THE 6L MLB (INT P/G)

	CONDUCTOR WIDTH = 12 mils CONDUCTOR SPACING = 13 mils		CONDUCTOR WIDTH = 8 mils CONDUCTOR SPACING = 9 mils	
	SIGNAL LAYER	CHARACTERISTIC IMPEDANCE (OHMS)	SIGNAL LAYER	CHARACTERISTIC IMPEDANCE (OHMS)
ROUTING IN 200 mil CHANNELS	S_1	61 OHMS	S_1	72 OHMS
	S_2	62	S_2	70
	$S_1 \rightarrow S_2$(1)	60	$S_1 \rightarrow S_2$	64
ROUTING IN 100 mil CHANNELS	S_1	64	S_1	71
	S_2	64	S_2	68
	$S_1 \rightarrow S_2$	58	$S_1 \rightarrow S_2$	65

- PROPAGATION DELAY = 1.9 ns/ft. (= 1/v).
- 80% RISE TIME ON TDR FOR 1 ft. CONDUCTOR LENGTH = 1.8 ns.
- BANDWIDTH FOR 1 ft. CONDUCTOR LENGTH = 278 MHz.

(1) THE TRANSITIONS FROM S_1 TO S_2 USED 10 VIAS.

TABLE B
K_{ne} = MAXIMUM NEAR-END PULSE CROSSTALK(1) FOR VARIOUS CONDUCTOR PAIRS ON THE 6L MLB (INT P/G)

CONDUCTOR WIDTH = 12 mils, CONDUCTOR SPACING = 13 mils

	INTERLAYER	INTRALAYER				ALTERNATELY ON S_1, S_2		
LOCATION OF ROUTING	$S_2 S_1$	LAYER	$Y_1 Y_2$	$Y_1 Y_3$	$Y_1 Y_4$	$X_1 X_2$	$X_1 X_3$	$X_1 X_4$
200 mil CHANNEL	0.5%	S_1	15%	3.0%	2.0%	12%	5.2%	8.4%
		S_2	14	2.9	1.2			
100 mil CHANNEL	0.5%	S_1	—	—	—	—	—	—
		S_2	—	—	—			

CONDUCTOR WIDTH = 8 mils, CONDUCTOR SPACING = 9 mils

	INTERLAYER	INTRALAYER				ALTERNATELY ON S_1, S_2		
LOCATION OF ROUTING	$S_2 S_1$	LAYER	$Y_1 Y_2$	$Y_1 Y_3$	$Y_1 Y_4$	$X_1 X_2$	$X_1 X_3$	$X_1 X_4$
200 mil CHANNEL	0.4%	S_1	20%	5.0%	2.4%	16%	5.2%	6.8%
		S_2	20	5.0	2.0			
100 mil CHANNEL	0.4	S_1	20	—	—	16	—	—
		S_2	20	—	—			

(1) CROSSTALK WAS MEASURED AS A PERCENTAGE OF THE SIGNAL STEP.

Fig. 11—Impedance, propagation delay, rise time, bandwidth, and pulse crosstalk for the 6L MLB (INT P/G) with 963C-100 connectors.

(a) NOTATION FOR INTERLAYER CROSSTALK ON THE 6L MLB (INT P/G, SURFACE ROUTING).

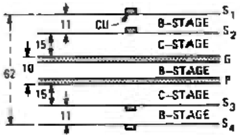

• 1 OZ CU CONDUCTORS • ALL DIMENSIONS IN MILS

(b) NOTATION FOR INTRALAYER CROSSTALK. W = 12, S = 13 MILS OR W = 8, S = 9 MILS.

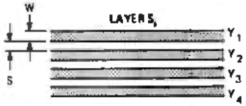

(c) NOTATION FOR CROSSTALK BETWEEN CONDUCTORS WHICH APPEAR ALTERNATELY ON LAYERS S_2 AND S_3. W = 12, S = 13 MILS OR W = 8, S = 9 MILS.

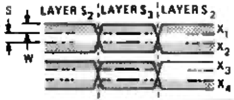

TABLE A
PULSE TRANSMISSION PROPERTIES OF THE 6L MLB (INT P/G, SURFACE ROUTING)[2]

	CONDUCTOR WIDTH = 12 mils CONDUCTOR SPACING = 13 mils		CONDUCTOR WIDTH = 8 mils CONDUCTOR SPACING 9 mils	
	SIGNAL LAYER	CHARACTERISTIC IMPEDANCE (OHMS)	SIGNAL LAYER	CHARACTERISTIC IMPEDANCE (OHMS)
ROUTING IN 200 mil CHANNELS	S_1	89 OHMS	S_1	104 OHMS
	S_2	66	S_2	72
	S_3	66	S_3	75
	S_4	92	S_4	110
	$S_2 \rightarrow S_3$[1]	59	$S_2 \rightarrow S_3$	65
ROUTING IN 100 mil CHANNELS	S_1	92	S_1	106
	S_2	69	S_2	73
	S_3	68	S_3	75
	S_4	93	S_4	109
	$S_2 \rightarrow S_3$	60	$S_2 \rightarrow S_3$	66

- PROPAGATION DELAY = 1.5 ns/ft. (= 1/v) ON S_1, S_4 AND 1.8 ns/ft. (= 1/v) ON S_2, S_3.
- 80% RISE TIME ON TDR FOR 1 ft. CONDUCTOR LENGTH = 1.8 ns.
- BANDWIDTH FOR 1 ft. CONDUCTOR LENGTH = 278 MHz.

[1] THE TRANSITIONS FROM S_2 TO S_3 USED 10 VIAS.

[2] NO COVERCOAT CASE. ON LAYERS S_1, S_4, COVERCOAT (GFR) HAS NEGLIGIBLE EFFECT ON RISE TIME (OR BANDWIDTH) BUT DECREASES THE CHARACTERISTIC IMPEDANCE BY ABOUT 10% AND INCREASES THE PROPAGATION DELAY BY ABOUT 10%.

TABLE B
K_{ne} = MAXIMUM NEAR-END PULSE CROSSTALK[1] FOR VARIOUS CONDUCTOR PAIRS ON THE 6L MLB (INT P/G, SURFACE ROUTING)[2]

CONDUCTOR WIDTH = 12 mils, CONDUCTOR SPACING = 13 mils

	INTERLAYER		INTRALAYER				ALTERNATELY ON S_2, S_3		
LOCATION OF ROUTING	S_1S_2	S_3S_4	LAYER	Y_1Y_2	Y_1Y_3	Y_1Y_4	X_1X_2	X_1X_3	X_1X_4
200 mil CHANNEL	25%	25%	S_1	14%	4%	1.8%	9.2%	2.8%	5.0%
			S_2	12	3.2	1.7			
			S_3	12	3.0	1.1			
			S_4	14	4.0	1.7			
100 mil CHANNEL	26	26	S_1	—	—	—	—	—	—
			S_2	—	—	—			
			S_3	—	—	—			
			S_4	—	—	—			

CONDUCTOR WIDTH = 8 mils, CONDUCTOR SPACING = 8 mils

	INTERLAYER		INTRALAYER				ALTERNATELY ON S_2,S_3		
LOCATION OF ROUTING	S_1S_2	S_3S_4	LAYER	Y_1Y_2	Y_1Y_3	Y_1Y_4	X_1X_2	X_1X_3	X_1X_4
200 mil CHANNEL	22%	22%	S_1	16%	5.8%	3.1%	12%	3.8%	7.1%
			S_2	16	4.5	2.0			
			S_3	16	5.3	2.0			
			S_4	16	5.8	2.5			
100 mil CHANNEL	21	22	S_1	16	—	—	13	—	—
			S_2	16	—	—			
			S_3	16	—	—			
			S_4	16	—	—			

[1] CROSSTALK WAS MEASURED AS A PERCENTAGE OF THE SIGNAL STEP.

[2] NO COVERCOAT CASE. ON LAYERS S_1, S_4, COVERCOAT (GFR) INCREASES INTRALAYER CROSSTALK BY ABOUT 20% OF THE TABULATED VALUES.

Fig. 12—Impedance, propagation delay, rise time, bandwidth, and pulse crosstalk for the 6L MLB (INT P/G, surface routing) with 963C-100 connectors.

(a) NOTATION FOR INTERLAYER CROSSTALK ON THE 8L MLB (INT P/G).

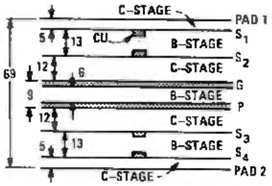

- 1 OZ CU CONDUCTORS
- ALL DIMENSIONS IN MILS

(b) NOTATION FOR INTRALAYER CROSSTALK. W = 12, S = 13 MILS OR W = 8, S = 9 MILS.

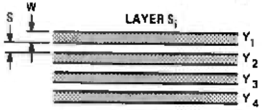

(c) NOTATION FOR CROSSTALK BETWEEN CONDUCTORS WHICH APPEAR ALTERNATELY ON LAYERS S_2 AND S_3. W = 12, S = 13 MILS OR W = 8, S = 9 MILS.

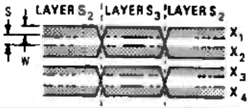

TABLE A
PULSE TRANSMISSION PROPERTIES OF THE 8L MLB (INT P/G)

	CONDUCTOR WIDTH = 12 mils CONDUCTOR SPACING = 13 mils		CONDUCTOR WIDTH = 8 mils CONDUCTOR SPACING = 9 mils	
	SIGNAL LAYER	CHARACTERISTIC IMPEDANCE (OHMS)	SIGNAL LAYER	CHARACTERISTIC IMPEDANCE (OHMS)
ROUTING IN 200 mil CHANNELS	S_1	94 OHMS	S_1	114 OHMS
	S_2	65	S_2	83
	S_3	68	S_3	82
	S_4	85	S_4	102
	$S_2 \rightarrow S_3$[1]	62	$S_2 \rightarrow S_3$	73
ROUTING IN 100 mil CHANNELS	S_1	91	S_1	111
	S_2	65	S_2	84
	S_3	68	S_3	83
	S_4	84	S_4	102
	$S_2 \rightarrow S_3$	62	$S_2 \rightarrow S_3$	74

- PROPAGATION DELAY = 1.9 ns/ft. (= 1/v).
- 80% RISE TIME ON TDR FOR 1 ft. CONDUCTOR LENGTH = 1.8 ns.
- BANDWIDTH FOR 1 ft. CONDUCTOR LENGTH = 278 MHz.

[1] THE TRANSITIONS FROM S_2 TO S_3 USED 10 VIAS.

TABLE B
K_{ne} = MAXIMUM NEAR–END PULSE CROSSTALK[1] FOR VARIOUS CONDUCTOR PAIRS ON THE 8L MLB (INT P/G)

CONDUCTOR WIDTH = 12 mils, CONDUCTOR SPACING = 13 mils

	INTERLAYER		INTRALAYER				ALTERNATELY ON S_2, S_3		
LOCATION OF ROUTING	$S_1 S_2$	$S_3 S_4$	LAYER	$Y_1 Y_2$	$Y_1 Y_3$	$Y_1 Y_4$	$X_1 X_2$	$X_1 X_3$	$X_1 X_4$
200 mil CHANNEL	20%	24%	S_1	12%	3.2%	1.3%	6.8%	2.6%	3.3%
			S_2	8.4	1.8	0.6			
			S_3	9.2	1.9	1.1			
			S_4	12	3.2	1.3			
100 mil CHANNEL	20	24	S_1	—	—	—	—	—	—
			S_2	—	—	—			
			S_3	—	—	—			
			S_4	—	—	—			

CONDUCTOR WIDTH = 8 mils, CONDUCTOR SPACING = 9 mils

	INTERLAYER		INTRALAYER				ALTERNATELY ON $S_2 S_3$		
LOCATION OF ROUTING	$S_1 S_2$	$S_3 S_4$	LAYER	$Y_1 Y_2$	$Y_1 Y_3$	$Y_1 Y_4$	$X_1 X_2$	$X_1 X_3$	$X_1 X_4$
200 mil CHANNEL	19%	20%	S_1	16%	6.2%	2.4%	9.2%	2.8%	5.2%
			S_2	12	3.6	2.0			
			S_3	12	3.6	1.6			
			S_4	18	5.6	2.4			
100 mil CHANNEL	18	20	S_1	15	—	—	10	—	—
			S_2	12	—	—			
			S_3	12	—	—			
			S_4	16	—	—			

[1] CROSSTALK WAS MEASURED AS A PERCENTAGE OF THE SIGNAL STEP.

Fig. 13—Impedance, propagation delay, rise time, bandwidth, and pulse crosstalk for the 8L MLB (INT P/G) with 963C-100 connectors.

REFERENCES

1. Bell Laboratories, "*BELLPAC* User Guidelines," unpublished work.
2. A. J. Rainal, "Pulse Transmission Properties of Various Circuit Pack Configurations," unpublished work.
3. D. B. Jarvis, "The Effects of Interconnections on High Speed Logic Circuits," IEEE Trans. Elec. Computers, *EC-12,* No. 5 (October 1963), pp. 476–487.
4. H. R. Kaupp, "Pulse Crosstalk Between Microstrip Transmission Lines," 7th International Electronic Circuit Packaging Symposium, IECP 2/5, August 1966, pp. 1–12.
5. A. J. Rainal, R. C. Restrick, and J. N. Lahti, "1A Processor; Backplane Signal Propagation Experiments," unpublished work.
6. A. J. Rainal, "Electrical Guidelines on the Use of the 963 Connector for CDCP Applications," unpublished work.
7. P. I. Kuznetsov and R. L. Stratonovich, *The Propagation of Electromagnetic Waves in Multiconductor Transmission Lines, 1964,* New York: Pergamon Press, 1964.
8. J. C. Isaacs, Jr., and N. A. Strakhov, "Crosstalk in Uniformly Coupled Lossy Transmission Lines," B.S.T.J., *52,* No. 1 (January 1973), pp. 101–114.
9. H. S. Gray, *Digital Computer Engineering,* Englewood Cliffs, N.J.: Prentice-Hall, 1963.
10. A. Feller, H. R. Kaupp, and J. J. Digiacomo, "Crosstalk and Reflections in High-Speed Digital Systems," Proceedings—Fall Joint Computer Conference, December 1965, Washington, D. C.: Spartan Books, pp. 511–525.
11. N. C. Arvanitakis, J. T. Kolias, and W. Radzelovage, "Coupled Noise Prediction in Printed Circuit Boards for a High-Speed Computer System," 7th International Electronic Circuit Packaging Symposium, IECP 2/6, August 1966, pp. 1-11.
12. Bell Telephone Laboratories Staff, *Physical Design of Electronic Systems,* Vol. I, "Design Technology," Englewood Cliffs, N.J.: Prentice-Hall, 1970, pp. 389–392.
13. B. M. Oliver, "Directional Electromagnetic Coupling," Proc. IRE, *42,* No. 11 (November 1954), pp. 1686-1692.
14. G. A. Campbell, "Dr. Campbell's Memoranda of 1907 and 1912," B.S.T.J., *14,* No. 4 (October 1935), pp. 558–572.
15. S. A. Shelkunoff, and T. M. Odarenko, "Crosstalk Between Coaxial Transmission Lines," B.S.T.J., *16,* No. 2 (April 1937), pp. 144–164.

Copyright © 1979 American Telephone and Telegraph Company
THE BELL SYSTEM TECHNICAL JOURNAL
Vol. 58, No. 5, May–June 1979
Printed in U.S.A.

High Resolution, Steep Profile, Resist Patterns

By J. M. MORAN and D. MAYDAN

(Manuscript received September 26, 1978)

High resolution and steep profile patterns have been generated in a 2.6-μm thick organic layer which conforms to the steps on a wafer surface and is planar on its top. This thick organic layer (a photoresist in the present experiments) is covered with an intermediate layer of SiO_2 *and a top, thin layer of X-ray or photoresist. After exposure and development of the top resist layer, the intermediate layer is etched by* CHF_3 *reactive ion etching. The thick organic layer is then etched by* O_2 *reactive ion etching. Submicron resolution with essentially vertical walls in the thick organic material was achieved. The technique is also applicable to photo- and electron lithography. It reduces the need for thick resist patterns for the lithography step and, at the same time, ensures high resolution combined with good step coverage.*

I. INTRODUCTION

One of the more difficult problems with resist pattern generation is to achieve good linewidth control, high resolution, and good step coverage simultaneously. Often the requirements appear to be mutually exclusive; good step coverage requires thick resist; high resolution, however, is more easily obtained in thin resist. This is true for all resists, both positive and negative.

With any resist, the ideal conditions to obtain high resolution and good linewidth control are a flat surface and a thin resist (3000–4000 A°). The flat surface means that the resist has very little variation in thickness and that, as a result, there will be little variation in resist line width. However, such resist line width variations will occur when lines traverse a step. As device wafers do have steps, thick resist (7000–15000 Å) must be applied to achieve coverage over steps.

We discuss here a method for generating high resolution, steep profile resist patterns by first preparing a flatter surface on the wafer.[1] This is done by applying a layer of thick organic material that conforms with its lower surface to the wafer and is planar on its top. The thick

Table I—High resolution, steep profile, resist patterns

Advantages
1. Planar surface for resist patterning
2. Excellent step coverage
3. Good linewidth control
4. Thinner resist can be used for better resolution
5. Eliminates standing waves and scattering in photolithography
6. Reduces proximity effects in electron lithography
7. Minimal resist erosion during substrate etch by plasma or ions
Disadvantage
Requires extra processing steps

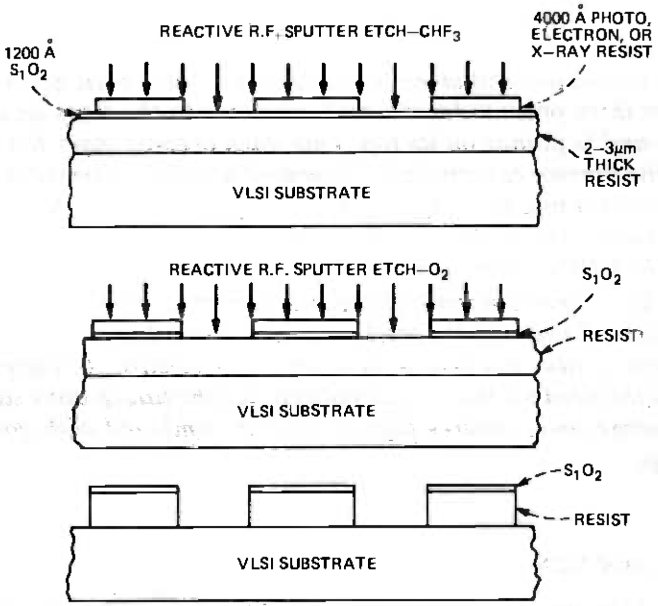

Fig. 1—Schematic presentation of the various steps required to define a steep resist profile.

layer is then patterned using an intermediate masking layer and a thin top layer of X-ray resist. The result is that as much as 2.6 μm of plasma-resistant organic material can be patterned with better than 1-μm resolution and steep sidewalls comparable with those in positive photoresist. The advantages and disadvantages of this technique are outlined in Table I.

II. EXPERIMENT

A 2.6-μm thick layer of photoresist,* serving as the thick organic layer, was spun on a silicon wafer. The intermediate layer of 0.12 μm

---

* HPR-204, manufactured by Hunt Chemical Co.

of silicon dioxide was plasma-deposited at 200°C on the photoresist, and then a 1.0-μm thick layer of chlorine-based negative X-ray resist was deposited on top of the oxide. Figure 1 is a schematic presentation of the processing sequence.

The top layer of X-ray resist was exposed and developed to a final thickness of 0.45 μm using an X-ray exposure tool.[2,3] With the X-ray resist as a mask, the SiO_2 was either plasma- or reactive-ion-etched with a CHF_3 gas. The pattern was then transferred into the thick organic (resist) layer using reactive RF sputter etching, with pure O_2 gas forming the plasma and the SiO_2 acting as the mask. The RF power density was 0.50 watt/cm^2 and the time required to etch the resist was

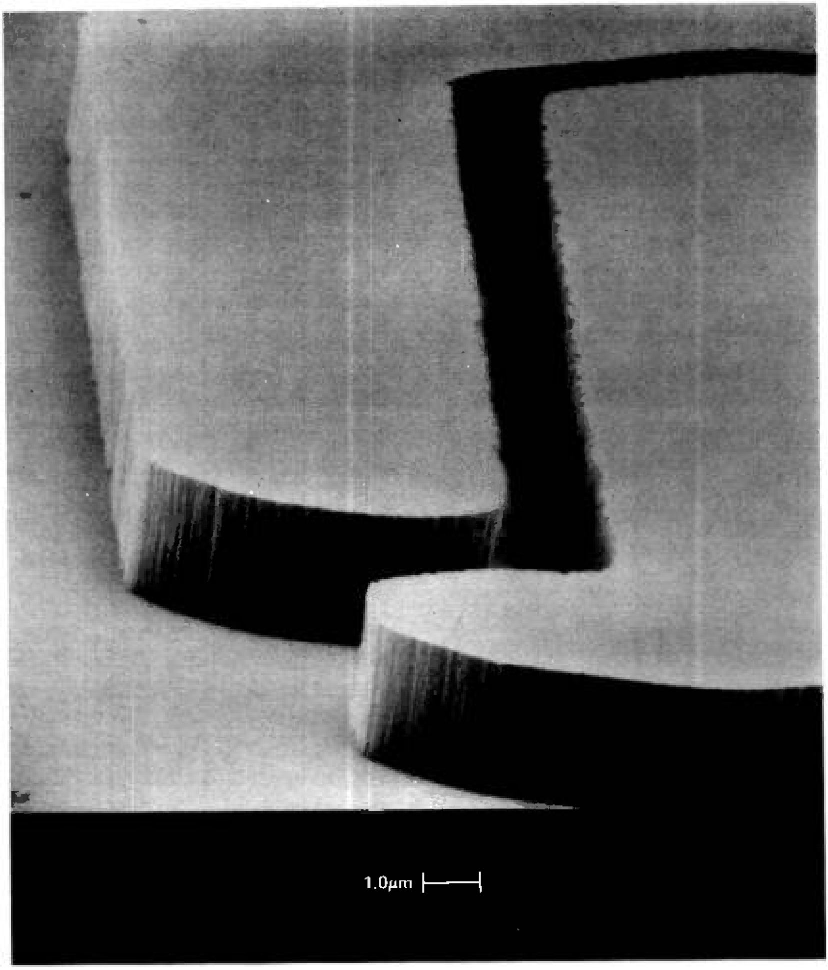

Fig. 2—Pattern etching into 2.6-μm thick resist layer using reactive RF sputter etching. Trench width is 1.5 μm.

20 minutes. Figure 2 shows the resultant pattern, which is 2.6 μm high and has a trench width of 1.5 μm. The photos were taken with a scanning electron microscope at a very steep angle to clearly show the wall structure of the resist. Note that the walls are perpendicular and there is very little undercut. The oxide is still on top of the organic (resist) layer, and its thickness loss during the sputter etch was less than 0.02 μm.

Another method of etching the thick organic layer is with plasma etching using a radial flow machine. This method, however, produced patterns with some undercut and had a resist etch uniformity variation across a 3-in. wafer of 50 percent, which, coupled with the undercut, would give poor linewidth control.

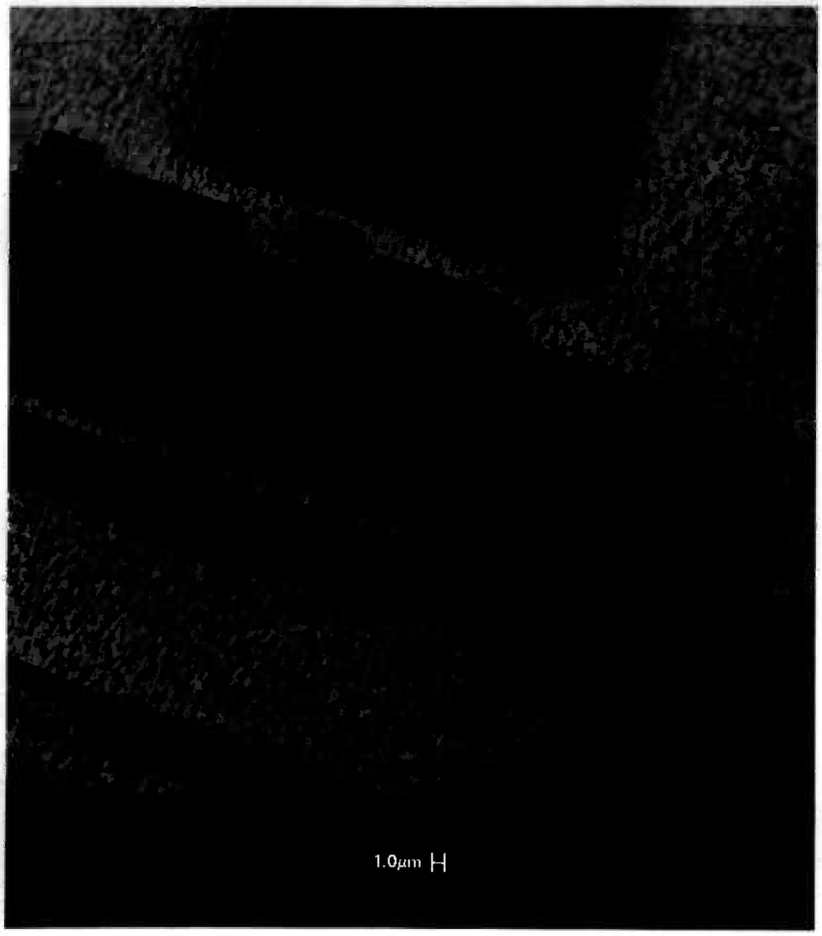

Fig. 3—SEM photograph of texture surrounding all the etched features. The fibers of this texture are aluminum oxide and are submicron in diameter.

One of the more serious problems encountered with RF reactive etching was the presence of texture after completion of the etch (see Fig. 3). This texture,[4,5] as determined by Auger analysis, consisted of aluminum oxide fibers that were resistant to further plasma processing. Their formation was due to the presence of aluminum in the active plasma area. In fact, the presence of any metals (e.g., copper, titanium, tantalum, etc.) also produced this texture.

Solution to the texture problem involved the construction of a chamber having no exposed metallic surfaces. Figure 4 shows a pattern etched under these conditions. The thick organic layer in this case is

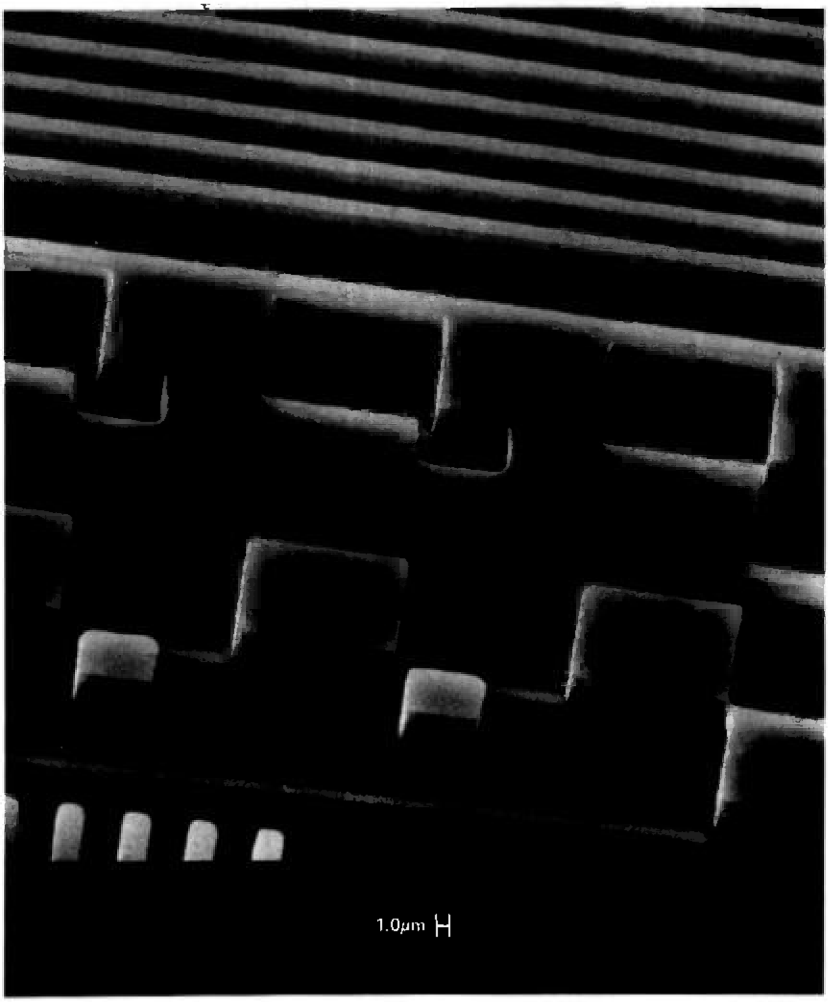

Fig. 4—Pattern sputter-etched using a system having no exposed metallic surfaces. Etching has caused no fiber formation.

Copyright © 1979 American Telephone and Telegraph Company
THE BELL SYSTEM TECHNICAL JOURNAL
Vol. 58, No. 5, May-June 1979
Printed in U.S.A.

A New Selective Fading Model: Application to Propagation Data

By W. D. RUMMLER

(Manuscript received September 21, 1978)

Channel transmission models for use in estimating the performance of radio systems on line-of-sight paths at 6 GHz are explored. The basis for this study is the simple three-ray multipath fade, which provides a channel transfer function of the form $H(\omega) = a[1 - b \exp -j(\omega - \omega_0)\tau]$, *where a is the scale parameter, b is a shape parameter,* τ *is the delay difference in the channel, and* ω_0 *is the (radian) frequency of the fade minimum. This model is indistinguishable from an ideal channel model, within the accuracy of existing measurements. The propagation data that confirm the model were obtained in summer 1977 from a 26.4-mile hop near Atlanta, Georgia. The received power at 24 sample frequencies spaced at 1.1 MHz and centered on 6034.2 MHz was continuously monitored and recorded during periods of anomalous behavior. The model is applied to estimating the statistics of the channel delay difference,* τ. *The average delay difference giving rise to significant selectivity in the channel is between 5 and 9 ns. The distribution of delay difference is obtained for delay differences greater than 10 ns. The channel is found to have more than 3 dB of selectivity (difference between maximum and minimum attenuation in band) due to delay differences greater than 20 ns for more than 70 seconds in a heavy fading month. (This is comparable to the time the channel attenuation of a single frequency exceeds 40 dB.) The three-path model requires further simplification for narrowband channel application. For a channel with 30 MHz bandwidth, a model with fixed delay of 6.3 ns provides a sufficiently accurate representation of all observed channel conditions. The resulting nonphysical model is used to statistically characterize the condition of the fading channel. The statistics of the parameters of the fixed delay model are almost independent and of relatively simple form. The distribution of the shape parameter b is of the form* $(1 - b)^{2.3}$. *The distribution of a is lognormal. For* $b > 0.5$, *the mean and standard deviation of* $-20 (\log a)$ *are 25 and 5 dB, respectively; the* *mean decreases to 15 dB for smaller values of b. The probability density function of ω_0 is uniform at two levels; measuring ω_0 from the center of the band, the magnitude of $\omega_0\tau$ is five times as likely to be less than $\pi/2$ than to be greater. A companion paper describes the use of this model for determining the bit error rate statistics of a digital radio system on the modeled path.*

I. INTRODUCTION

Performance prediction of a digital radio system on a line-of-sight microwave channel requires an accurate statistical model of the channel. Because different digital radio systems may have different sensitivities to the various channel impairments, the model must be complete to the extent that it must be capable of duplicating the amplitude and phase (at least approximately) of all observed channel conditions. To facilitate laboratory measurements and computer simulations for calculating outage, the model should be realizable as a practical test circuit and should have as few parameters as possible. Most important, the parameters should be statistically well behaved.

Two types of models have been generally considered for line-of-sight microwave radio channels: power series type models[1-3] and multipath models.[4-6] A power series model will require a few terms only if the channel is a multipath medium with a small spread of delays relative to the reciprocal bandwidth of the channel.[3] This implies that one must understand the channel as a multipath medium to understand the behavior of a power series model. Hence, we have limited our characterization efforts to multipath models.

The basis for this study is the simple three-ray multipath fade.[7] If the fading in a channel can be characterized by a simple three-path model, the channel will (as shown in Section II) have a voltage transfer function of the form

$$H(\omega) = a[1 - be^{\pm j(\omega-\omega_0)\tau}]. \tag{1}$$

where the real positive parameters a and b control the scale and shape of the fade, respectively, τ is the delay difference in the channel, and ω_0 is the radian frequency of the fade minimum. The plus and minus signs in the exponent correspond, respectively, to the channel being in a nonminimum phase or minimum phase state. Note that, with appropriate choices of parameters, this model can be reduced to a two-path model or a scaled two-path model, etc.

It has been shown previously,[7] and is illustrated in Section II, that the simple three-path fade overspecifies the channel transfer function if the delay is less than ⅙ B, where B is the observation bandwidth. The critical value of τ for a 30-MHz channel is about 5.5 ns, which is comparable to the mean delay in the channel. As a consequence, unless the channel response can be determined to an accuracy on the order of 0.001 dB, a unique set of parameters a, b, τ, and f_o cannot be determined for more than half the faded channel conditions encountered. To avoid this problem, one must suppress or fix one of the model parameters. Section II shows that the delay, τ, is the only parameter which, when fixed, produces a reasonable model.

While a model with a fixed delay may appear to be a strange choice, it has all the required characteristics for modeling the channel transfer function. Figure 1 shows the amplitude of the channel transfer function of eq. (1) on a power scale and on a decibel scale for $\tau = 6.31$ ns. With τ fixed, the response minimum is shifted with respect to frequency by varying f_o. Varying a changes the overall level and b changes the

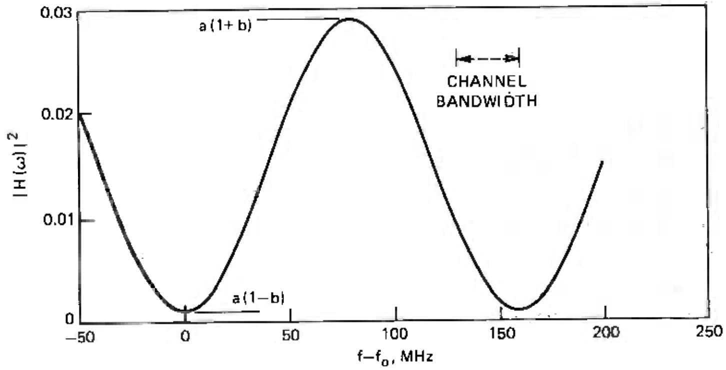

(a) MODEL POWER RATIO

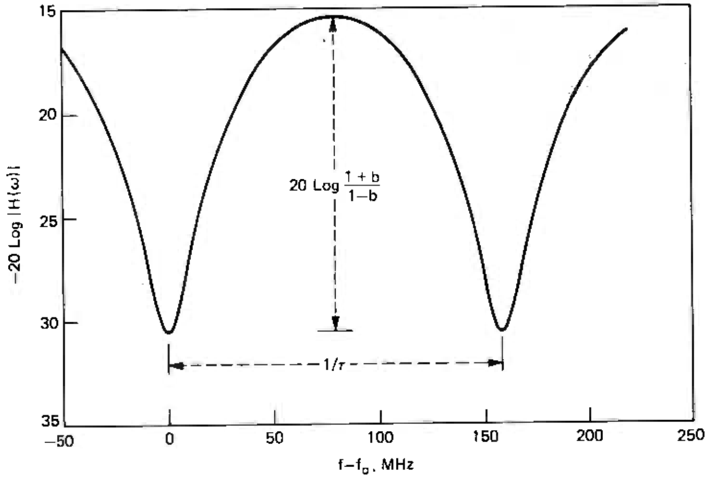

(b) MODEL ATTENUATION IN DECIBELS

Fig. 1—Channel model function. $H(\omega) = a[1 - b\exp(-j\,2\,\pi(f - f_o)\tau)]$, for $\tau = 6.3$ ns, $a = 0.1$, $b = 0.7$.

"shapeliness." If the minimum is within the 30-MHz bandwidth of a channel, the fixed delay model can generate notches with a wide range of levels and notch widths. With the minimum out of band, it can generate a wide range of combinations of levels, slopes, and curvatures within the channel bandwidth. Section VI shows that the model versatility, with τ chosen to be 6.31 ns, is sufficient to characterize a 30-MHz channel in the 6-GHz common carrier band.

Section II provides a brief discussion of the simple three-path fade. A comparative discussion of the relative merits of the different possible simplifications of this model leads to the choice of the fixed delay model.

The data used for detailed evaluation of models were obtained from a 6-GHz experiment in Palmetto, Georgia, in June 1977. The radio channel was equipped with a general trade 78-Mbit/s, 8-PSK digital radio system, and the received spectrum was monitored with a set of 24 filters with bandwidths of 200 kHz spaced at a 1.1-MHz separation across this channel. During fading activity, the received power of each of these frequencies was measured five times each second, or once every 2 seconds, depending on how rapidly the channel was changing; sampled power, quantized in 1-dB steps, was recorded by the MIDAS system.* The data base used for this study consists of approximately 25,000 scans representing 8400 seconds of fading activity; about 8700 scans were recorded during periods when the equipment was indicating errors. These data represent about 60 percent of the fading activity of a heavy fading month; therefore, the derived statistics must be viewed as provisional and subject to some modification as additional data are processed. At the very least, the data base is sufficiently large to indicate what can happen on the channel and to form a basis for choosing and validating a model.

As described in Section III, the model parameters were estimated for each scan by fitting the magnitude squared of the transfer characteristic [eq. (1)] to the observed channel shape as characterized by the power received at the sampling frequencies. Phase is subsequently derived by assuming the channel is minimum phase. Problems are encountered in realizing a minimum-phase solution because of quantization noise and the presence of certain channel shapes caused by large delays. The procedure for handling these difficulties is described.

The statistics of the parameters of the fixed delay model are discussed in Section IV. Equations providing an idealized description of the statistics of the parameters of the model are also given here.

In Section V, the determination of the delay difference present in the channel is considered. In the first subsection, it is demonstrated

---

* Multiple Input Data Acquisition System, constructed by G. A. Zimmerman; see Ref. 1.

that, during the observed period of fading activity, the average delay is 9 ns. A lower bound on the distribution of delay difference for large delays is developed in the second subsection. A third subsection provides an example of a channel scan that can best be approximated by a three-path fade with a delay difference of 26 ns. Fades with at least this delay and with a more moderate amount of shape (2 dB or more) were encountered for about 60 seconds of the data base studied. Thus, one might expect 26-ns delays to be present during about 100 seconds of a heavy fading month.

The presence of such large apparent delays raises questions as to the accuracy with which the fixed delay model represents the channel. These questions are addressed in Section VI where the statistics of the errors in modeling scan fits are described. The errors are small and do not compromise the usefulness of the model.

Results and conclusions are briefly summarized in Section VII.

II. CHOICE OF MODEL

In this section, we provide a brief description of the simple three-path model and show why it cannot be used to estimate delays when the delay bandwidth product is less than ⅙. In a comparative discussion, we show why the fixed delay model is the only simplification of the model that is manageable.

2.1 Simple three-path model

Consider a channel characterized by three paths or rays. The amplitude of the signal on each of these three paths, as seen by the receiver, is 1, a_1, and a_2. The second and third paths are delayed with respect to the first by τ_1 and τ_2 seconds, respectively, where $\tau_2 > \tau_1$. We define the simple three-path model by requiring the delay between the first two paths to be sufficiently small, i.e.,

$$(\omega_2 - \omega_1)\tau_1 \ll 1, \tag{2}$$

where ω_2 and ω_1 are the highest and lowest (radian) frequencies in the band. The complex voltage transfer function of the channel at a frequency ω may be illustrated with a phasor diagram. Figure 2a shows the phasor diagrams for ω_1 and ω_2 superimposed. By designating the amplitude of the (vector) sum of the first two paths by a; the angle of the sum by $\phi = \omega_0\tau - \pi$, where τ is equal to τ_2, the delay difference in the channel; and the amplitude of the third ray by ab, we obtain the simplified diagram in Fig 2b.*

---

* Note that, if the third amplitude is greater than the sum of the first two, we interchange the assignments of amplitudes a and ab and obtain a nonminimum phase fade.

The simple three-path fade cannot be used for a channel model because the path parameters lack uniqueness. The basic difficulty is illustrated by the two superimposed fades in Fig. 3. Note that the amplitudes of the transfer functions of these two fades match, at

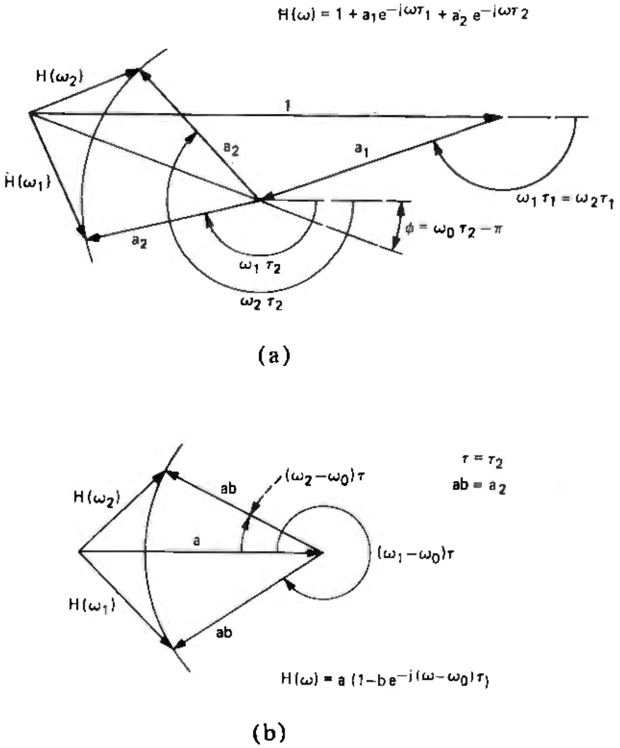

Fig. 2—Simple three-path fade. (a) Three rays shown. (b) Simplified.

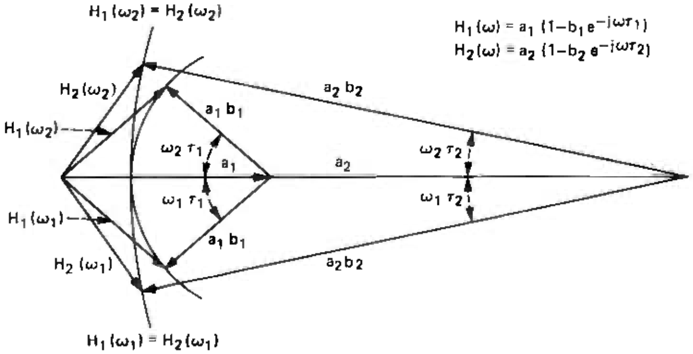

Fig. 3—Two degenerate simple three-path fades with $\omega_0\tau = 0$.

midband and at both edges. It has been shown elsewhere[7] that fades matched in this way will be identical in band to within a few tenths of a decibel at most, and will have almost identical envelope delay distortion. Given noisy quantized measurements of $|H(\omega)|$ over the band, it is impossible to distinguish between such fades unless we fix one of the four parameters. Let us consider each of the four possibilities.

2.2 Pseudo two-path fade

If one fixes the amplitude, a, at unity, the simple three-path fade reduces to a two-path fade with independent control of the frequency of the minimum of the response. The difficulty with this model, as may be seen by referring to Fig. 2b, is that it can provide in-band minima only for $|H(\omega)| < 1$ and maxima in-band only for $|H(\omega)| > 1$. In other words, the model cannot match an in-band maximum at an arbitrary fade level. In addition, it was found that during approximately half the periods when the radio equipment was indicating errors, the channel could not be well modeled with a pseudo two-path model.

2.3 Scaled two-path fade

If one fixes the phase, $\phi = \omega_0\tau - \pi$, in the simple three-path model at 0, the fade reduces to a scaled two-path fade. (For a two-path fade, we require the additional condition $a = 1$.) This is the most physically desirable of the reduced three-path models because it may be derived without recourse to the three-path formalism. Unfortunately, it is mathematically intractable, particularly when dealing with amplitude data only. In fitting the model to a given channel shape (in the manner described in Section III for the fixed delay model), one obtains a function of a, b, and τ that must be minimized to obtain the best fit. Because of the $\omega\tau$ term in the exponent of the model, this function has a local minimum in every interval of τ of length 0.17 ns, the reciprocal of 6 GHz. Since the possible range of τ extends to about 30 ns, one may have to perform hundreds of minimizations to find the best fit to a single channel scan. Even then this "best fit" may have no minimum phase realization, and there is no known procedure that leads to one.

2.4 Fixed b model

If one fixes the amplitude b in the simple three-path model, the resulting reduced model has all the mathematical difficulties of the scaled two-path model and no satisfactory physical interpretation.

2.5 Fixed delay model

It is demonstrated in the remainder of this paper that the fixed delay model described in Section I is useful and effective in characterizing the channel.

III. ESTIMATION PROCEDURES

This section describes how the model parameters are estimated from the channel scans and how realizability difficulties are surmounted.

3.1 Parameter estimation

The channel data consist of a set of 25,000 scans of the channel power spectrum. Each scan consists of a power measurement at each of 24 frequencies at 1.1-MHz spacing across the channel. (Actually, only 23 frequencies are used since the 19th was inoperative during this test period). The power measurements are recorded in decibels, and each must be referenced to the average power level of that frequency at mid-day. With proper conversion and calibration, the basic data characterizing a scan are a set of power ratios. We designate the power ratio at nth frequency by Y_n, where

$$Y_n = Y(\omega_n) \qquad n = 1, 2, \cdots, 24. \tag{3}$$

We wish to model the channel with a voltage transfer function of the form given in eq. (1), which we repeat here for convenience

$$H(\omega) = a[1 - be^{\pm j(\omega-\omega_0)\tau}], \tag{1}$$

Thus our estimate of Y_n will be

$$\hat{Y}_n = |H(\omega_n)|^2 = \alpha - \beta \operatorname{Cos}(\omega_n - \omega_0)\tau, \tag{4}$$

where

$$\begin{aligned} \alpha &= a^2(1 + b^2) \\ \beta &= 2a^2b. \end{aligned} \tag{5}$$

For convenience, we measure frequency in the units of the frequency separation of the power measurements. Thus,

$$\omega_n = 2\pi f_n = 2\pi n(1.1 \times 10^6) \quad n = 1, 2, 3, \cdots, 24. \tag{6}$$

If we choose

$$\tau = \frac{1}{N(1.1 \times 10^6)}, \tag{7}$$

then

$$\omega_n\tau = 2\pi \frac{n}{N}. \tag{8}$$

For the fixed delay model, we choose $N = 144$ which gives a model τ of 6.31 ns. Thus, the in-band frequencies correspond to n values between 1 and 24, and the channel transfer function given by the model is periodic for n modulo 144, corresponding to a frequency shift of $144 \times 1.1 \times 10^6 = 158.4$ MHz.

The weighted mean-square error between the estimated and observed power is given by

$$E = \frac{\sum_{n=1}^{24} C_n (Y_n - \hat{Y}_n)^2}{\sum_{n=1}^{24} C_n}, \tag{9}$$

where the summation skips $n = 19$ as described above, and where C_n is a weighting applied to the measurement at frequency ω_n. Since the original data, from which the Y_n's were derived, were uniformly quantized on a logarithmic scale, it is appropriate to use a weighting that is approximately logarithmic. Hence, we use the weighting function

$$C_n = \frac{1}{Y_n^2}. \tag{10}$$

A number of different weighting functions were tested, but the one given by (10) is, generally, the most satisfactory.

Estimates of a, b, and f_o may be obtained by minimizing the weighted mean-square error, E. It is shown in the appendix that one may obtain closed form estimators for α, β, and f_o by substituting eq. (4) into (9) and minimizing E, first with respect to α, then with respect to β (or vice versa), and last with respect to f_o. In the resulting scheme, the estimator of f_o, the frequency of the model minimum, is a function of data only. The estimators of α and β are functions of the estimated f_o and the data.*

After estimates of α and β have been calculated, the parameters a and b of the model are obtained by inverting the relationships given by eq. (5).

$$b = \frac{\alpha}{\beta} - \left[\left(\frac{\alpha}{\beta}\right)^2 - 1\right]^{1/2} \tag{11}$$

$$a = \left[\frac{\beta}{2b}\right]^{1/2}. \tag{12}$$

It is clear from (11) and (12) that we can realize the channel shape with the model only if $\alpha \geq \beta$. This is to be expected. Since $|H(\omega)|^2$ is a power transfer function, it must be positive for all frequencies, which is possible only if $\alpha \geq \beta$ [see eq. (4)]. Thus, the condition $\alpha \geq \beta$ allows us to obtain a minimum (or nonminimum) phase transfer function whose magnitude squared is the minimum weighted mean-square error fit to the observed power transfer response of the channel.

---

* For mathematical simplicity, we actually use an estimator for β conditioned on f_o, α, and the data.

3.2 Application of estimators

If the procedure described above is strictly applied to the set of 25,000 scans in the data base, one finds that about 35 percent of the scans cannot be modeled with real values of a and b. A study of these problem scans revealed that the estimator for f_o, the frequency of the fade minimum, was biased for two types of scans. One type is a scan with little shape, dominated by quantization noise; the other is a selective channel shape having a steep slope across the band. Both types of scan are illustrated in Fig. 4. The scan in Fig. 4, which is almost flat, was fabricated to illustrate the severity of the quantization problem. The other scan is typical of the more shapely troublesome scans.

To obtain a good realizable fit to such channel shapes requires degrading the quality of the fit; that is, moving the parameters away from the values that minimize the fit error, eq. (9). Given the form of the estimation scheme, this is easily accomplished by moving the frequency of the fade minimum, f_o, away from its original "optimum" value and reoptimizing the remaining parameters to obtain values of a and b that are optimum for the new value of f_o. Figures 5 and 6 illustrate the results of such a quasi-optimization regarding f_o as a free parameter. They show the fit error E and the values of a and b as f_o is varied from its original optimum value. Figure 5 corresponds to the flat fade in Fig. 4 and Fig. 6 to the sloped fade.

The shapes of the curves in Figs. 5 and 6 are typical of those obtained when the channel has no minimum in band. The weighted error in the fit, E, is not very sensitive to the estimate of f_o, the

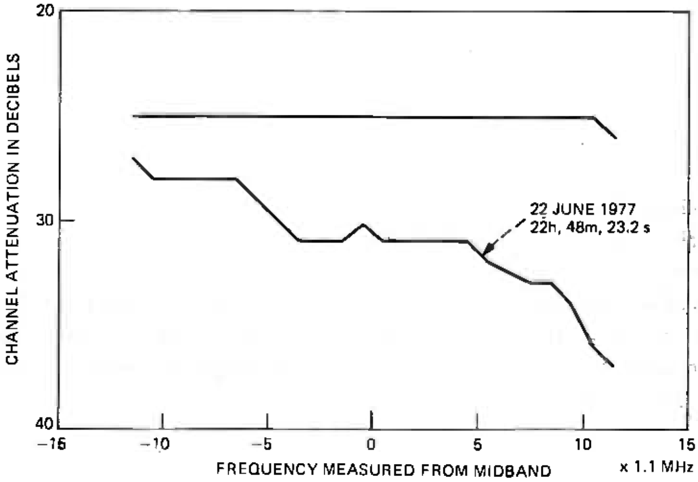

Fig. 4—Two channel scans that produce realization difficulties.

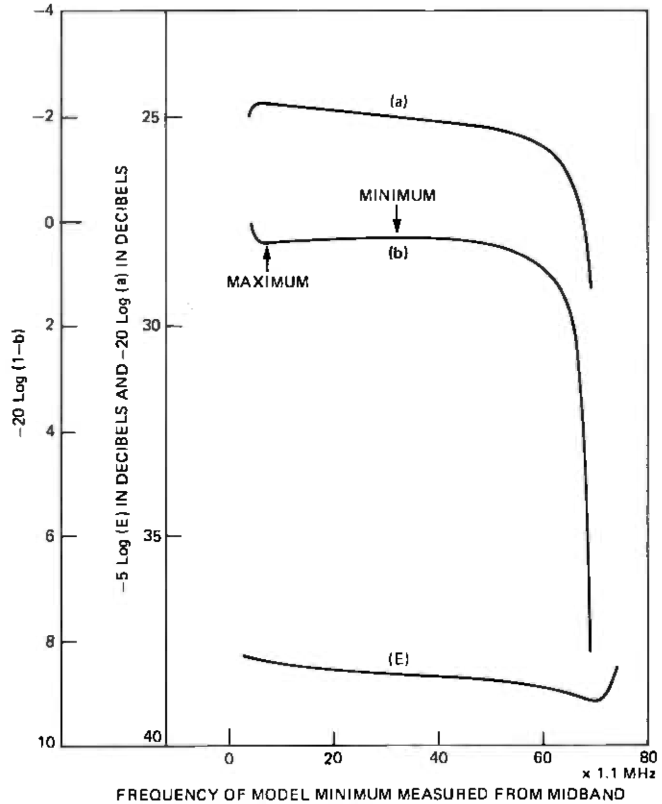

Fig. 5—Locus of weighted fit error and model parameters with f_o as a free variable for flat fade in Fig. 4.

frequency of the modeled fade minimum. The minimum of E is broad and flat, due to quantization and instrumentation noise in the channel. The variation of the parameter a with f_o is also typically very gradual. The salient features of the variation of b with respect to f_o are clearly seen in Fig. 6, and are also present and labeled in Fig. 5. As f_o is varied from its original optimum value, b varies from a value of 1 to a value of 0 in a sideways s-curve with two stationary points, a maximum and a minimum. Extensive simulations with known channel characteristics indicate that a good choice of parameters is the set corresponding to the point where b is locally minimized. To illustrate this point, assume that the channel shape is that given by the model, with 6.3-ns delay, f_o at 18.5 × 1.1 MHz, $a = 0.04$, and $b = 0.7$. One can construct a plot similar to Figs. 5 and 6 for this simulated fade, with the result shown in Fig. 7. The curves in this figure illustrate the results cited above, in that the true value of f_o occurs near a minimum value of b. A better

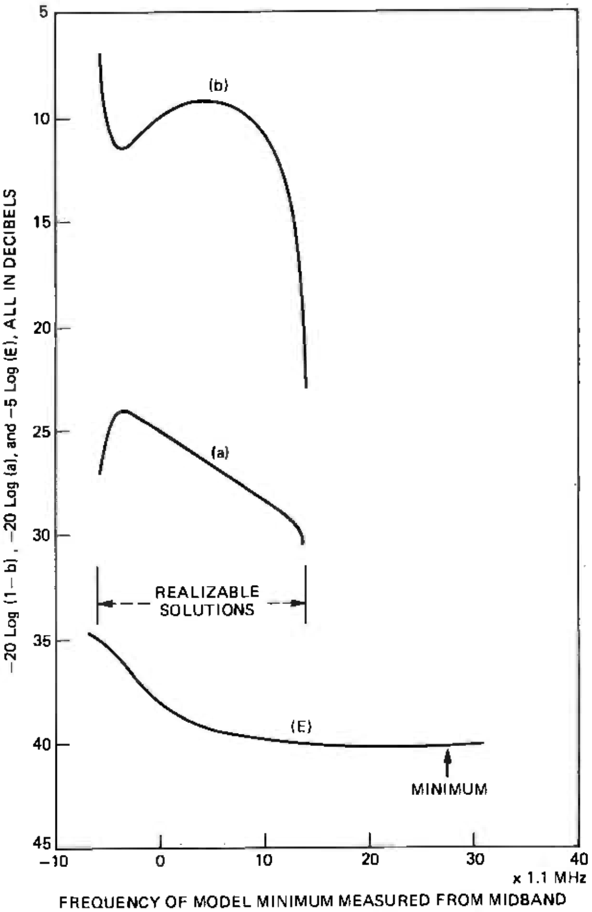

Fig. 6—Locus of weighted fit error and model parameters with f_o as a free variable for typical scan in Fig. 4.

choice for the case shown and for others that have been simulated would be "on the shoulder" between the minimum and $b = 1$; however, such a criterion is difficult to quantify.

To summarize, if the standard routine does not provide a realizable fit to a scan, one merely varies f_o, the position of the minimum, until one obtains a realizable solution with a value of b that is stationary* with respect to variations in f_o. We recognize that this procedure introduces additional sources of error into the estimates of the model parameters. The errors in a and b are small because b is near a stationary value and a is slowly varying. The error in f_o is also small,

---

* Since b is a monotone function of α/β, it is only necessary to invert solutions with stationary values of the ratio, α/β.

usually less than 3 MHz, but is always in the direction corresponding to moving the minimum nearest to the band closer. We consider the effects of these errors in Section VI.

IV. MODEL STATISTICS

Applying the procedures described in Section III to the scans in the data base results in 25,000 sets of values of a, b, and f_o. The relative joint frequency of occurrence of these three parameters may be described by the set of distribution functions shown in Figs. 8 to 12. The distribution of the parameter b is described in Fig. 8 in terms of the distribution of $-20 \log (1 - b)$, which is approximately exponentially distributed with a mean of 3.8 dB. This distribution gives the time that b exceeds the value given by the abscissa as a fraction of the time in a heavy fading month that the rms level in the channel is depressed by more than 15 dB. For instance, we see that 40 percent of the time

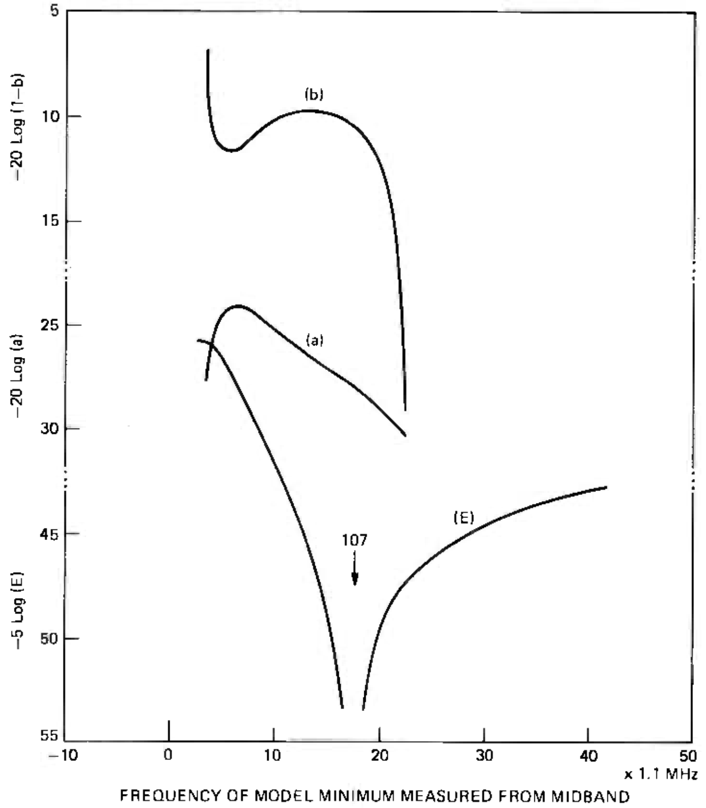

Fig. 7—Locus of weighted fit error and model parameters with f_o as a free variable. For channel given by model with $\tau = 6.31$ ns, $a = 0.04$, $b = 0.7$, $f_o = 18.5 \times 1.1$ MHz.

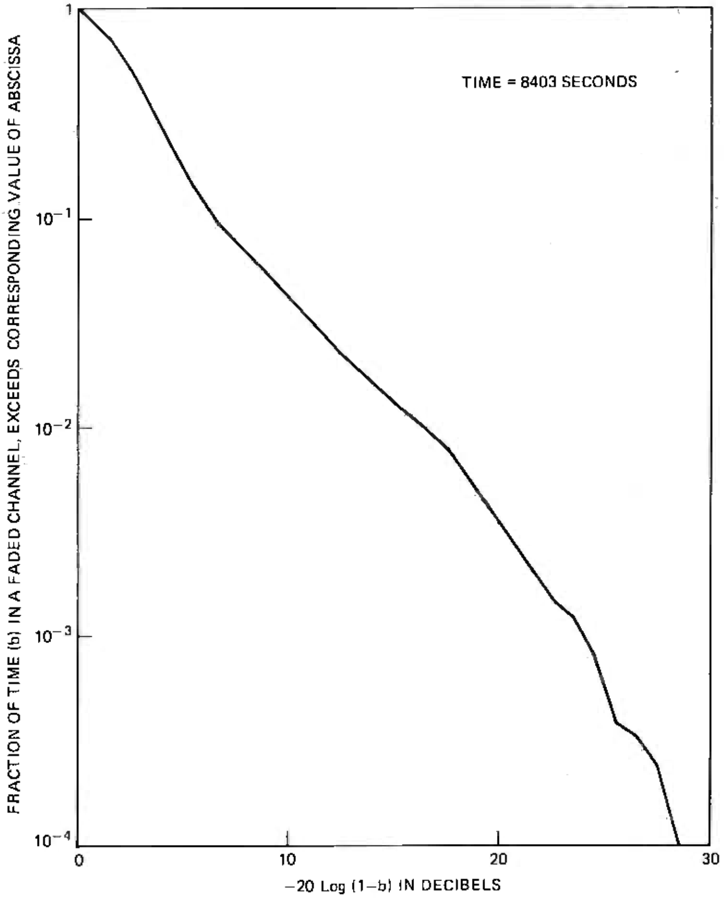

Fig. 8—Distribution of *b*.

when the channel is depressed the value of b exceeds 0.3. It exceeds 0.7 for 4 percent of that time, and 0.99 about 0.3 percent of that time. The distribution of b can be modeled in the form

$$P(1 - b < X) = X^{\overline{\frac{20}{3.8 \text{ Log } 10}}} = X^{2.3}. \tag{13}$$

The distribution of a is conditioned on b and is approximately lognormal as shown in Figs. 9 and 10. The mean and standard deviation of the distributions in Figs. 9 and 10 are plotted in Fig. 11. From Figs. 9 to 11 it is apparent that a and b are almost independent; however, less shapely fades tend to occur at less depressed values. We note that shape occurs when the average depression is 20 to 25 dB,* that the

---

* The value of a corresponds to average power level over a large frequency span and not strictly to the average power in a narrowband channel.

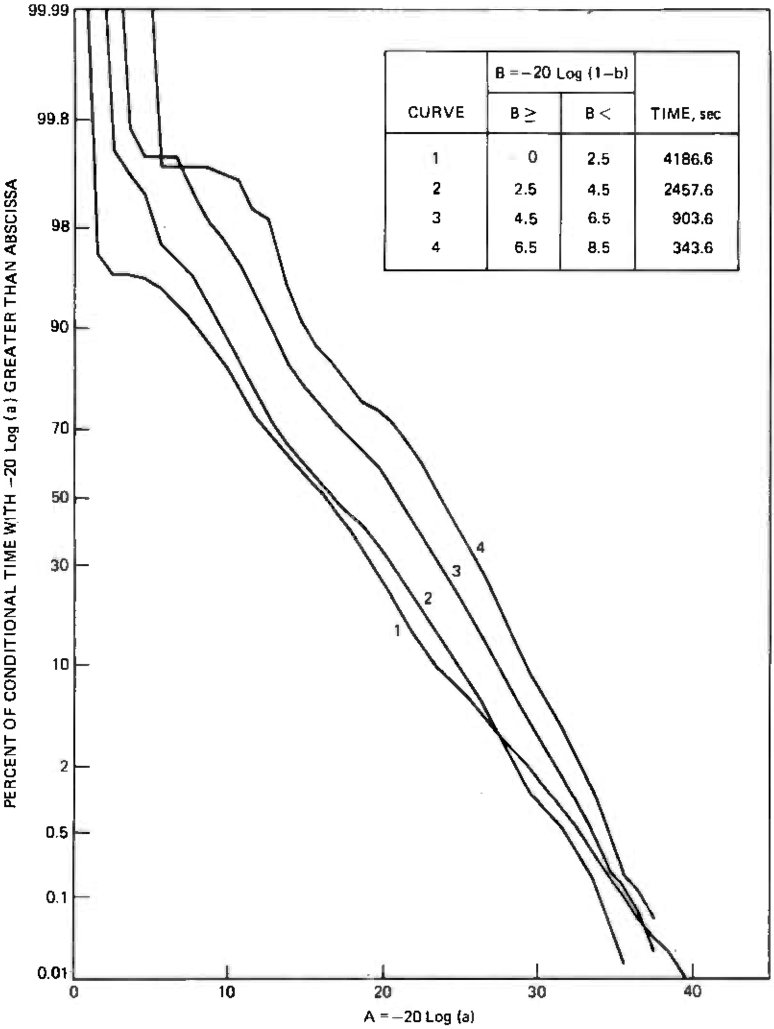

CURVE	B = −20 Log (1−b)		TIME, sec
	B ≥	B <	
1	0	2.5	4186.6
2	2.5	4.5	2457.6
3	4.5	6.5	903.6
4	6.5	8.5	343.6

Fig. 9—Distribution of a conditioned on the value of b for $-20 \log (1 - b)$ less than 8.5 dB.

average depression is near 25 dB for b greater than 0.7, and that it falls off gradually to 15 dB for small b. The distribution of $A = -20 \log a$ is conditioned on b and may be modeled as

$$P(A > Y) = 1 - P\left[\frac{Y - A_o(b)}{5}\right], \tag{14}$$

where P is the cumulative distribution function of a zero mean, unit variance, and Gaussian random variable, and $A_o(b)$ is the mean of A for a given value of b as given in Fig. 11. We see from Fig. 11 that the

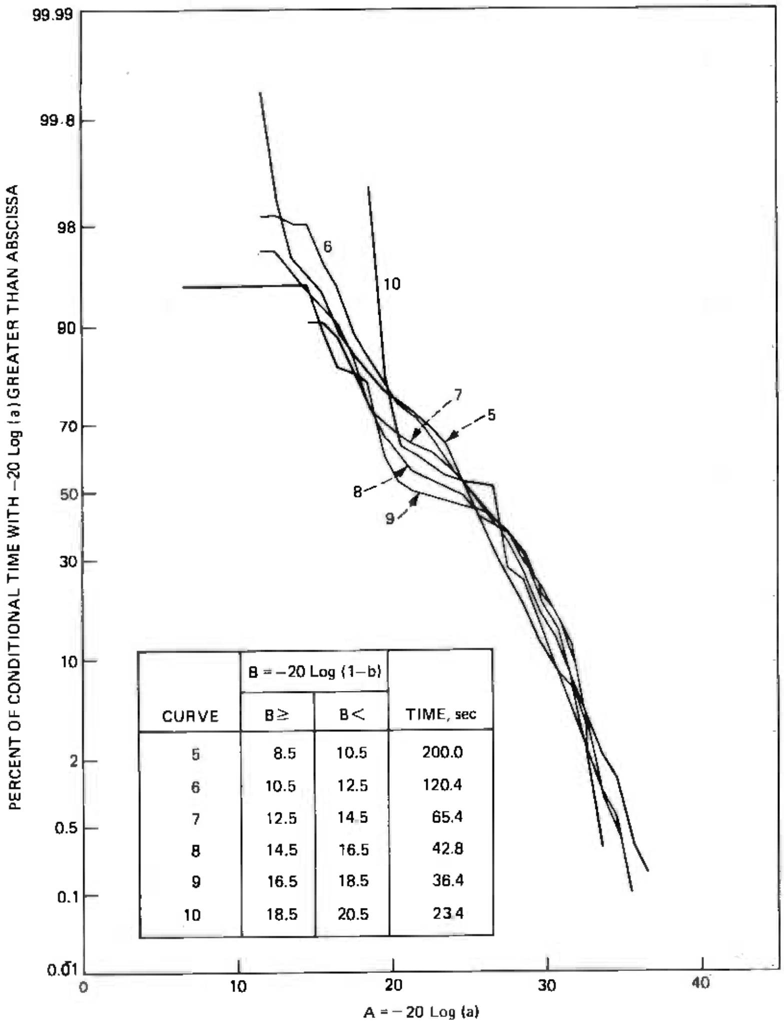

CURVE	B = −20 Log (1−b) B≥	 B<	TIME, sec
5	8.5	10.5	200.0
6	10.5	12.5	120.4
7	12.5	14.5	65.4
8	14.5	16.5	42.8
9	16.5	18.5	36.4
10	18.5	20.5	23.4

Fig. 10—Distribution of *a* conditioned on the value of *b* for $-20 \log (1 - b)$ greater than 8.5 dB.

standard deviation of A may be taken as 5 dB regardless of the value of b; the variations near $-20 \log (1 - b) = 20$ are due to small sample problems.

Figure 12 shows the time during which scans had f_o in 4 × 1.1-MHz frequency intervals. It is, in effect, an estimate of the density function of the distribution of f_o and is, consequently, quite noisy. The maxima near ± 30 × 1.1 MHz from the center of the band are due in part to the movement of estimates of f_o to achieve realizability. While, on physical grounds, one would expect f_o to have a uniform distribution, the fixed delay model is decidedly not a physical model. Consider a simulated set of simple three-path fades having a uniform distribution of f_o, fixed values for a and b, and a delay τ, fixed at a value other than 6.31 ns. This set of fades will engender a nonflat probability density function for the f_o's obtained in fitting to the 6.31-ns model. The probability density function is flat within the band regardless of the fixed delay of the set of simulated fades; however, it will more nearly resemble that shown in Fig. 12 if the delay of the set is greater than 6.31 ns than if it is less than 6.31 ns. In short, Fig. 12 is characteristic of a channel with a considerable fraction of delay differences greater than 6 ns.

Based on Fig 12, we approximate the probability density function of f_o by a two-level function. Note that f_o is defined on an interval of length $1/\tau$, where τ is 6.3 ns the delay of the model. Thus, with f_o measured from the center of the band, the probability density function for f_o may be approximated by

$$p_{f_o}(f_o) = \begin{cases} \dfrac{5\tau}{3} & |f_o| \le \dfrac{1}{4\tau} \\ \dfrac{\tau}{3} & \dfrac{1}{4\tau} < |f_o| < \dfrac{1}{2\tau}. \end{cases} \tag{15}$$

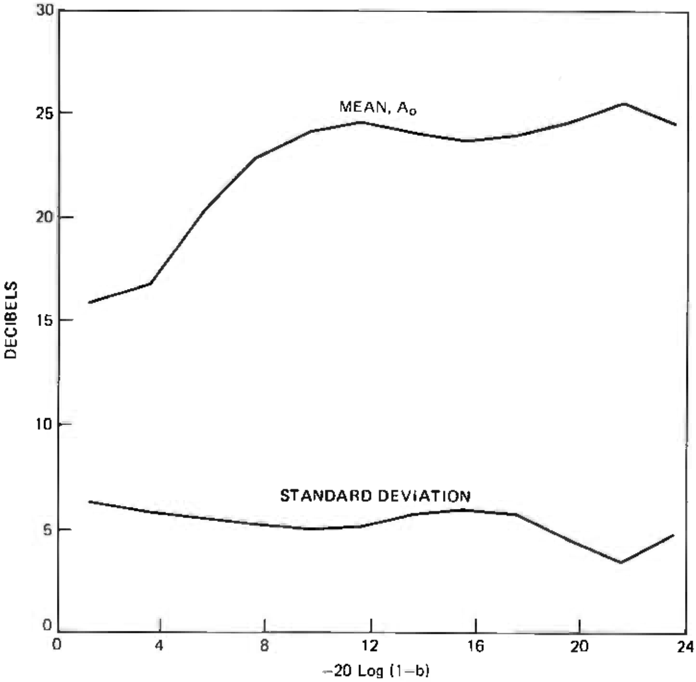

Fig. 11—Mean and standard deviation of the distribution of $-20 \log a$ as a function of $-20 \log (1 - b)$.

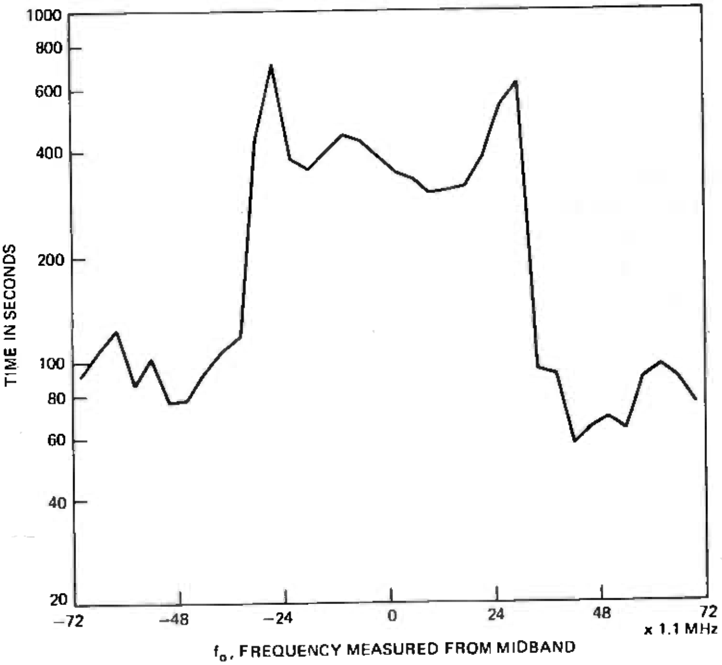

Fig. 12—Time that model parameter, f_o, was in intervals of width 4 × 1.1 MHz.

An extensive examination of various conditional distributions has established that there are no other obvious and pervasive dependencies among the statistics of the parameters.

V. CHANNEL DELAY DIFFERENCE

This section presents some results obtained in estimating the channel delay difference. Some techniques described here are used in the error analysis in Section VI. Three topics are considered in this section. First a simple method is presented of estimating the average delay spread in the channel. A second subsection shows that the distribution of large delays (larger than 10 ns) can be obtained for a simple three-path fade model. The delay distribution is shown to be consistent with the estimate of average delay. A third subsection illustrates the problem with an observed channel shape that can be matched most successfully using a simple three-path model with a delay of approximately 26 ns.

5.1 Mean delay difference in the channel

The mean delay difference of a channel that can be characterized by a simple three-path model is easily estimated. Consider a fade with a delay, τ. If f_o, the frequency of the minimum, is uniformly distributed, the probability that such a fade produces a minimum in a band B Hz wide is equal to the ratio of the bandwidth to the spacing of the minima, or

$$\frac{B}{1/\tau} = B\tau. \tag{16}$$

If $p(\tau_k)\Delta\tau$ is the fractional number of fades having delays between $(k-1)\Delta\tau$ and $k\Delta\tau$, then the fractional number of fades having a minimum in band will be $P_{\min}$, where

$$P_{\min} = \sum_k B\tau_k p(\tau_k)\Delta\tau = B\bar{\tau} \tag{17}$$

and

$$\bar{\tau} = \sum \tau_k p(\tau_k)\Delta\tau = \int \tau p(\tau)\,d\tau. \tag{18}$$

It follows from eq. (17) that one may estimate the mean delay, $\bar{\tau}$, from a knowledge of $P_{\min}$, the fractional number of scans having a minimum in a band of width B. Since any method of determining $P_{\min}$ is acceptable, consider estimates of $P_{\min}$ from the parameters estimated using the fixed delay model. The method of estimating the frequency parameter in the model involved moving null positions of some fades that had out-of-band minima. These fades can be excluded by using only the central two-thirds of the band in estimating $\bar{\tau}$. Of the 24,920 scans in the data base, 3974 had minima between the *4th* and *20th* frequencies. Hence,

$$\bar{\tau} = \left[\frac{3974}{24920}\right] \frac{1}{16 \times 1.1 \times 10^6} = 9.1 \text{ ns}. \tag{19}$$

One might argue that the mean delay should be estimated for a more carefully screened set of scans. Table I shows the mean delay estimates obtained from scan populations qualified by having the estimate of the model parameter a in a given 5-dB interval. Table II

Table I—Mean delay for scans selected by value of parameter, a

$-20 \log a$, dB	Number of Scans	Scans with Min. in Band	Delay, $\bar{\tau}$, ns
0–5	101	31	17.4
5–10	725	235	18.4
10–15	4299	875	11.6
15–20	6891	1161	9.6
20–25	7644	906	6.7
25–30	4184	606	8.2
30–35	1019	159	8.9
All	24920	3974	9.1

Table II—Mean delay for scans selected by value of parameter, b

$-20 \log 1\text{-}b$, dB	Number of Scans	Scans With Min. in Band	Delay, $\bar{\tau}$, ns
0–2	10,442	1186	6.5
2–4	7040	1712	13.8
4–6	3721	538	8.2
6–8	1474	191	7.4
8–10	892	118	7.5
10–12	527	68	7.3
12–14	282	28	5.6
14–16	190	21	6.3
16–18	146	46	17.9
18–20	99	32	18.4
All	24920	3974	9.1

shows mean delay estimates qualified by the model parameter b, which specifies the shapeliness of the fade.

With several exceptions, the estimated delay spreads given in Tables I and II are reasonably constant. One exception is seen for large values of b ($-20 \log 1 - b$ greater than 16). This is consistent with a channel for which large differential attenuation across the channel is more likely to occur when long delays are present. The existence of such a correlation should not be surprising. The other exception is the large delays estimated for small values of b and for values of a between 0 and 10 dB. We provide strong evidence of the existence of such a class of fades in the next subsection. The existence of this subclass of fades suggests that they have a different physical source than the other fades in the population.

5.2 Distribution of delay difference

To further enhance our knowledge of the distribution of delay in the channel, the data base was processed to extract a delay estimate. Recall that, for the fixed delay model, parameter estimates are chosen to minimize the weighted fit error [E in eq. (9)] for a given fixed τ. The present calculation was performed for a set of different values of τ and the value which produced the smallest weighted fit error and corresponded to a realizable fade was designated as the delay for that scan if it met certain qualifications.

Because of the degeneracy in the simple three-path model, changing the delay in the fixed delay model will not appreciably improve the fit for any scan that can be well approximated by a fixed delay of 6 ns or less.[7] In performing the optimum delay calculation, the weighted fit error was minimized for a predetermined set of delays; the differences between adjacent delay values were chosen to be approximately 15 percent. A given scan was assigned a delay different from 6.3 ns only if the third best value of the weighted fit error was at least 0.1 dB worse than the best value. (We use the third best value because we must examine three values to detect a minimum.) This criterion sets a threshold on the acceptable sharpness of the minimum in the fit error with respect to changes in delay.

The selection criterion was chosen, after several iterations, to insure regularity in the estimates derived from successive scans. With the chosen criterion, the scans that were assigned a new delay occurred in groups of consecutive scans and may be said to constitute fading events. During any of these events, the delay was consistent in that indicated delays were within ±15 percent. If we assume that the physical channel does not change between scans, we can associate a time with each scan and plot the distribution of the time periods during which the characterizing delay was greater than a specified delay.

A series of such plots, conditioned on the concurrently estimated value of *b*, is given in Fig. 13. The uppermost curve contains the data derived from all scans which met the selection criterion; its shape is

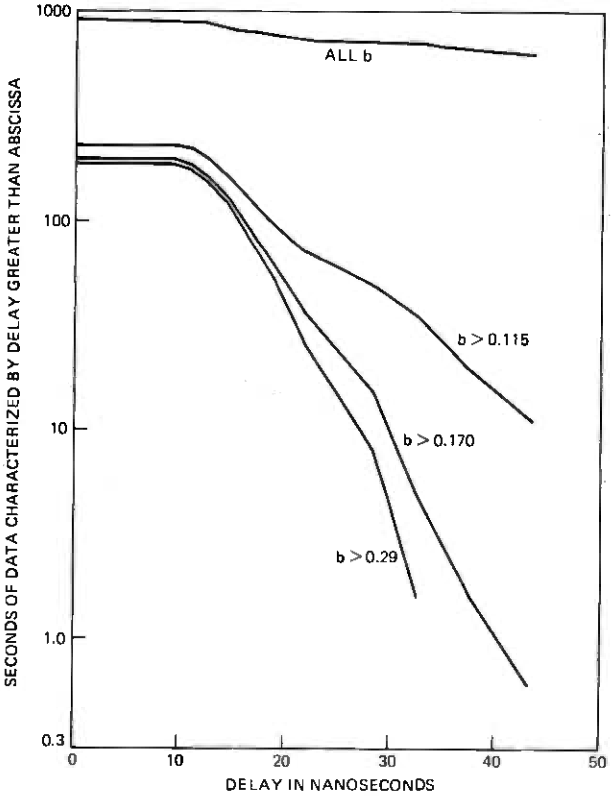

Fig. 13—Distribution of optimum delay for simple three-path model, as qualified by realizability, the sharpness of minimum, and by several values of the model parameter *b*.

dominated by the 627 seconds during which the channel was best modeled by a delay of 43 ns (the largest delay in the test set) or more, but had little shape ($b < 0.115$). These characteristics contribute to the large (18 ns) mean delays noted in the previous subsection for small values of b. They may be due to quantization but are apparently not artifacts of the estimation scheme. Although the origin of this type of channel defect is currently not understood, it should not trouble any existing radio system.

It is apparent from the distributions in Fig. 13 that very few scans qualified for a new delay with delays less than 10 ns. Consequently, the distribution should not be trusted for delays less than 12 or 15 ns; beyond 15 ns, it may be interpreted as a lower bound to the true distribution. The three curves qualified by the parameter b correspond to fades with peak-to-peak variability of 2, 3, and 6 dB. (Peak-to-peak variability is $20 \log(1 + b/1 - b)$, as may be seen in Fig. 1.) If the delay were exponentially distributed, the distribution of delay would be a straight line on Fig. 13 and would have the form

$$P(\tau > x) = e^{-x/\bar{\tau}}. \tag{20}$$

Fitting a straight line to the three distributions in Fig. 13 for which $b > 0.115$ shows that the average delay decreases with increasing b. The corresponding values are 5, 5.5, and 11 ns. Note that this implies that b and τ in a simple three-path model are not independent.

5.3 An example of a long delay scan

To confirm the existence of long delay scans, consider an event that covered approximately 10 seconds on 22 June 1977, from 23 h, 28 m, 54 s. A representative scan from the middle of this period is shown with the fit obtained with the fixed delay (6.3 ns) model in Fig. 14a. To emphasize the consistency of this channel condition, an average of the channel condition for the central 4.2 seconds (21 scans) of this event is compared to the selected scan in Fig. 14b.

It is apparent from Fig. 14*a* that the 6.3 ns delay does not have enough curvature (delay is too short) to precisely model the channel shape. Figure 15 shows the same scan modeled by three-path fades having delays of 22.7, 26, and 30.3 ns. The 26-ns fit is the best; it has a weighted fit error 0.4 dB better than the 22.7-ns fit and 0.8 dB better than the 30.3 ns fit. However, the closeness of all three fits illustrates the difficulties in estimating channel delay differences. Visually, one would choose the 26-ns model on the basis that the 30.3-ns fit has too much curvature and the 22.7-ns fit too little.

VI. ERROR ANALYSIS

To verify that the model adequately represents the transmission characteristics of the channel, we examine the errors between the

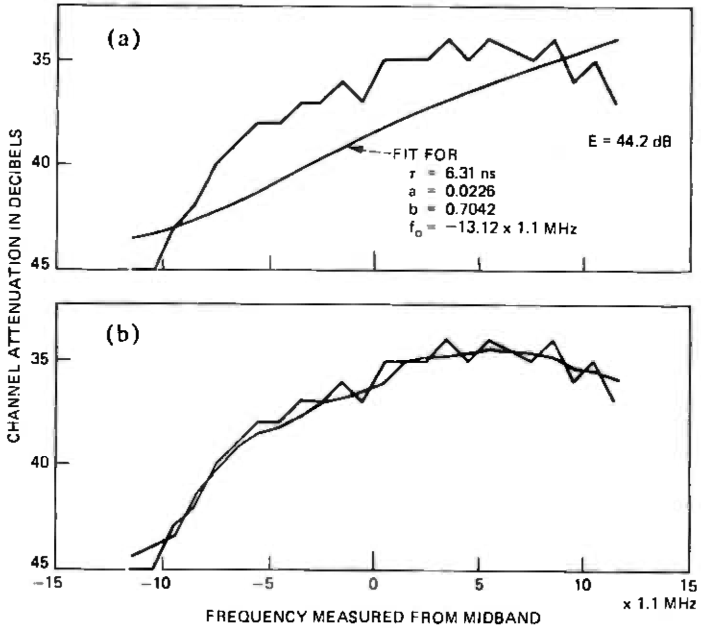

Fig. 14—Scan from 22 June 1977, 23 h, 28 m, 48.6 s. (a) Comparison with fixed delay model. (b) Comparison with average of scans from 23 h, 28 m, 46.4 s to 23 h, 28 m, 50.4 s.

channel as observed and as modeled. In this section we consider the statistics of the rms errors and the maximum errors.

6.1 RMS errors

A useful measure of the quality of the fit of the model to a given channel scan is the root-mean-square value of the decibel error at each of the sampled frequencies. Denoting this error as E_{rms}, we have

$$E_{rms} = \left[\frac{1}{23} \sum_{\substack{n=1 \\ n \neq 19}}^{24} (\text{dB error at } f_n)^2 \right]^{1/2}. \tag{21}$$

The model parameters were estimated, as described in Section III, to minimize the error, E, which is a weighted sum of the squares of the power differences at each frequency [see eq. (9)]. The weighting was chosen [eq. (10)] so that the error E would approximate the error E_{rms} as given by eq. (21).* Indeed, one may show directly that the two expressions are equivalent as long as

$$\left| 1 - \frac{\hat{Y}_n}{Y_n} \right| \ll 1 \text{ for all } n. \tag{22}$$

---

* Note that the parameter estimation problem cannot be solved in closed form by minimizing E_{rms}.

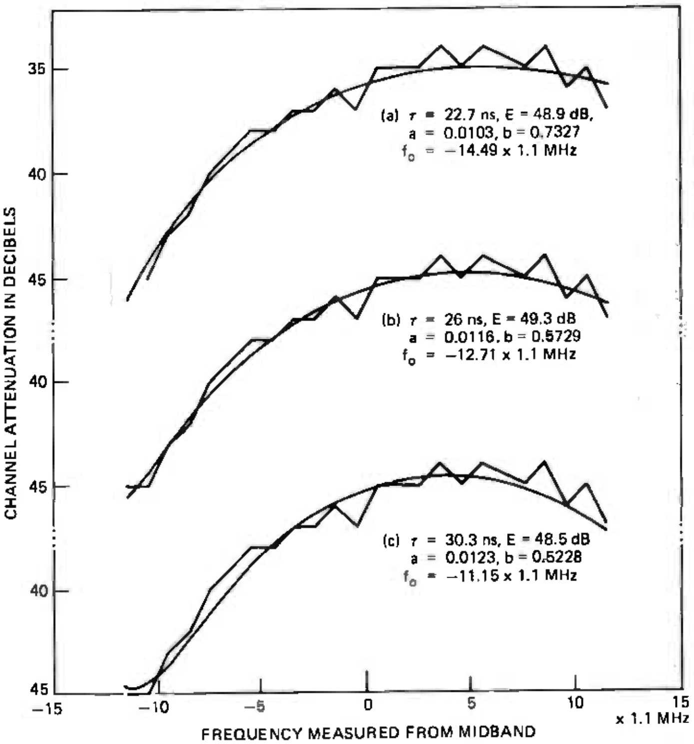

Fig. 15—Model fits to long delay scan for three different model delays.

As we have seen in Fig. 14, this inequality is not always satisfied. Consequently, in using E_{rms} as a standard of comparison, we are evaluating not only how well the model fits the observed channel, but also how well we have chosen the parameters to make the match.

The error E_{rms} is a desirable quantity to work with because we can estimate its distribution under the assumption of perfect matching. We observe that if the decibel error were Gaussian with unit variance and zero mean, 23 E_{rms}^2 would be a χ^2 variable with 20 degrees of freedom (to account for the three parameters estimated per scan). Observations of a simulated channel with the transmitter and receiver back-to-back indicate that the instrumentation errors are approximately Gaussian with a standard deviation, σ_i, of about 0.65 dB. Observations of the channel at mid-day with the channel nominally flat and unfaded indicate that the standard deviation of the errors is between 0.68 and 0.73, varying frequency to frequency and day to day by a few hundredths of a decibel. Hence, if we enter a table of the χ^2 distribution, $Q(\chi^2 \mid 20)$, with

$$\chi^2 = \frac{23\, E_{rms}^2}{\sigma_i^2}, \tag{23}$$

we can determine the distribution of E_{rms} under the assumption of perfect matching.* This distribution is shown as a reference on Figs. 16 and 17. It is indicated by a solid curve labeled "ideal" for $\sigma_i = 0.70$ and by o's for $\sigma_i = 0.75$.

Figure 16 presents the distribution of the rms error for two scan subpopulations using the fixed delay (6.3 ns) model. The subpopulation of the distribution labeled "standard" consists of all scans that could be modeled directly; the distribution labeled "modified" shows the rms error distribution for all scans which required an adjustment of the frequency of the modeled fade to achieve realizability. Figure 17 shows the distribution of the rms error for the composite of all samples using the fixed delay (6.3 ns) model. The distribution labeled simple three-path model indicates the error distribution that was obtained when the scan fitting allowed unqualified variation in model delay to achieve the best fit. That is, the calculation described in Section 5.2 was performed and the results were qualified only on the basis of realizability.†

In each case described above, the mean value of the rms error is close to the median value. For the two subpopulations shown in Fig. 16, the calculated mean fit errors correspond to σ_i values of 0.76 and 0.85 dB, or the errors are about 0.09 dB larger when a realizable fit is obtained by varying the frequency of the model minimum. Comparing the composite distributions in Fig. 17, we find that the mean error in the fixed delay (6.3 ns) model corresponds to $\sigma_i = 0.78$ dB or about 0.08 dB higher than that observed when the channel is quiescent. The simple three-path model has a distribution of rms error that very nearly matches the ideal distribution (with 19 degrees of freedom) for $\sigma_i = 0.75$. This is consistent with the instrumentation error imputed to the standard distribution in Fig. 16 and is indicative of the instrumentation error in the presence of multipath fading. It is exceptionally good considering that the data are obtained from time sequential measurements on a dynamically changing channel. One concludes that the modeling error is negligible for the simple three-path model. For the fixed delay model under the assumption that the instrumentation and modeling errors add in quadrature, the modeling error has a tolerable value on the order of 0.2 dB. That is,

$$[(0.75)^2 + (0.2)^2]^{1/2} = 0.776.$$

The tails of the distributions in Figs. 16 and 17 for large errors are of considerable interest. The tails near small values are of little

---

* From the central limit theorem, we know that E^2_{rms} will be approximately Gaussian, as is χ^2, regardless of whether or not the measurement errors are precisely Gaussian.

† Note that although one cannot always reliably localize the values of the parameters in fitting with the simple three-path model (see discussions in Section 2.1 and Ref. 7), the error in the fit is always well defined.

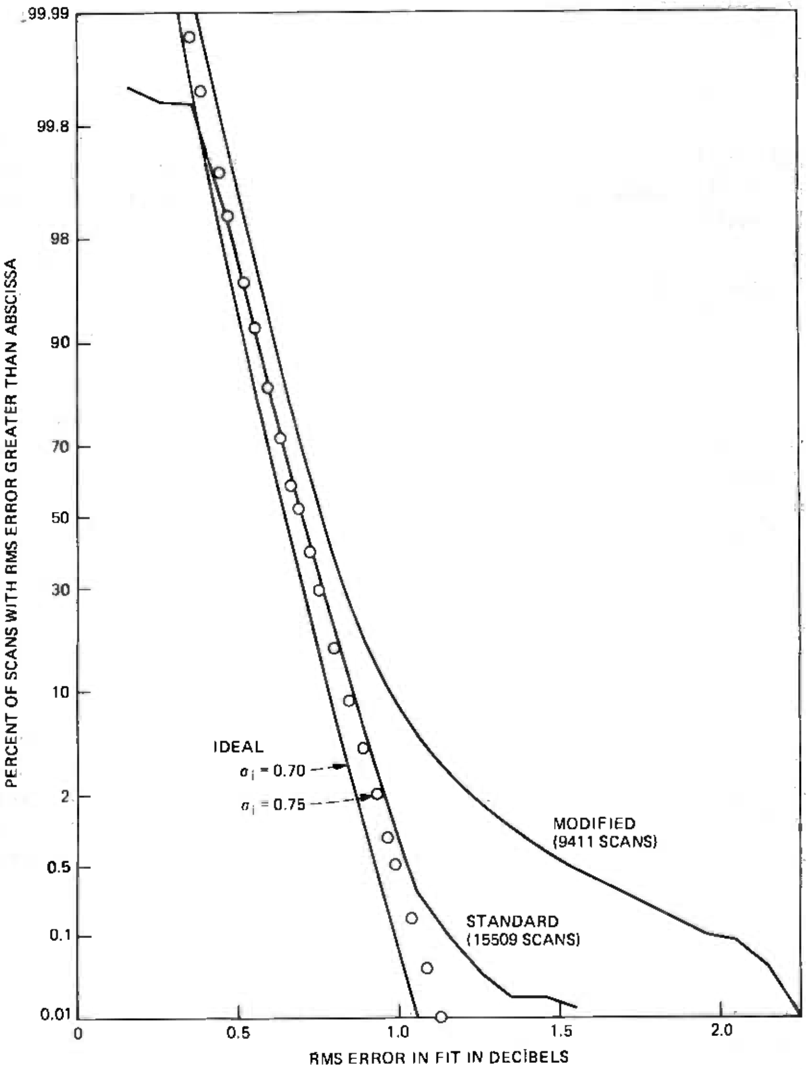

Fig. 16—Distribution of rms fit error for two scan subpopulations with fixed delay (6.3 ns) model.

consequence; they are distorted by quantization because one cannot associate any error with the 12 flat fades included in the data base. The deviation of the distributions from the ideal distribution at large errors is significant.

The large deviation of the modified fits in Fig. 16 reflects the failure of the fixed delay (6.3 ns) model to accurately fit the long delay fades. The tail deviation from ideal is modest down to about the 0.5 percent level, corresponding to a few tens of seconds per month. For compar-

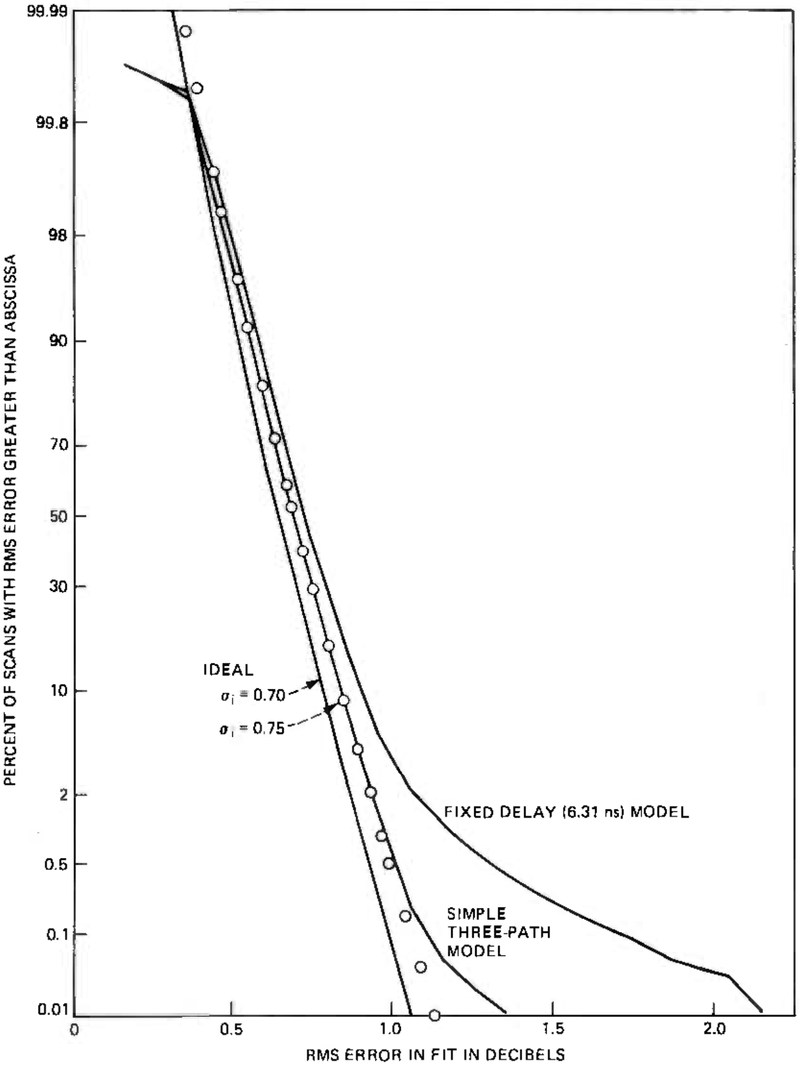

Fig. 17—Distribution of rms fit error for composite population with fixed delay and simple three-path models.

ison, we note that the rms error of the fit shown in Fig. 14a is 2.3 dB; this was the worst fit encountered for the fixed delay (6.3 ns) model. However, even in this case the model failure is hardly describable as severe. The model of the channel is depressed by 40 dB and has 9.5 dB of gain slope; the actual channel is depressed by 39 dB and has 11 dB of gain slope. Also, we note that the 6.3-ns delay model has the response minimum at about the same frequency as the best representation, the 26-ns delay model shown in Fig. 15.

The deviation of the tail of the error distribution for the three-path fade (Fig. 17) reflects the fact that there are fades that even this model has difficulty in fitting. An example of such a fade is shown in Fig. 18 along with the fit provided by the fixed delay (6.3 ns) model. The same rms error (1.6 dB) is obtained for all values of model delay between 0.05 and 9 ns; the fit degrades for larger delays. Either more than three rays are needed to describe the channel shape in Fig. 18, or the channel is so depressed that the amplitudes in the notch are distorted due to closeness to the noise level in the measuring equipment. The scan shown in Fig. 18 is one of three similar scans and has little statistical significance.

6.2 Maximum errors

Another type of error that can be used to judge the quality of the fit of the model to the channel is the worst-case error. That is, after fitting to each scan, one records the magnitude of the largest difference (in decibels) between the observed channel shape and the shape calculated from the model. The following paragraphs consider the distribution of these worst-case errors.

As in the preceding subsection, we can calculate an ideal distribution; however, the ideal distribution is not as realistic in this case since it is strongly dependent on the tails of the distributions of the individual measurement errors. We assume that each power measurement had

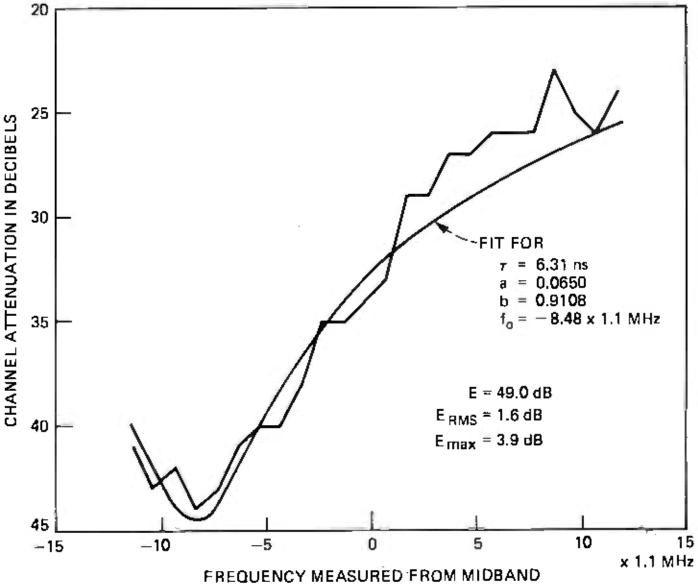

Fig. 18 –Severe fade observed on 22 June 1977 at 22 h, 29 m, 8.6 s.

an error in decibels that was Gaussian, with zero mean, a standard deviation of $\sqrt{20/23}\ \sigma_i$ to account for the three parameters estimated from the 23 observations per scan,* and that the errors are independent frequency to frequency. If the probability of any one measurement having an error less than x is denoted by $P_1(x)$, the probability that all 23 have values less than x is

$$P_{23}(x) = [P_1(x)]^{23}. \tag{24}$$

This is the probability that the maximum error is less than x, whereas we want the probability that it is greater than x which we denote $Q_{23}(x)$. It follows immediately from eq. (24) that

$$\begin{aligned} Q_{23}(x) &= 1 - [P_1(x)]^{23} \\ &= 1 - [1 - Q_1(x)]^{23}. \end{aligned} \tag{25}$$

The distribution given by (25) is used as a reference in Figs. 19 and 20, which show the distribution of the maximum error for the same cases as in Figs. 16 and 17. Since the tails of these distributions are well behaved for larger errors, the distribution of the maximum errors is apparently dominated by the instrumentation noise. That is, if we use for the standard deviation of the measurement noise the value obtained from the mean of E_{rms} for one of these cases (as given in Section 6.1), the resulting worst-case error distribution calculated with eq. (25) will closely match the observed maximum error distribution.

VII. CONCLUSIONS

By analyzing the errors in fitting the observed channel characteristics in Section VI, we demonstrated that the simple three-path fade model is indistinguishable from a perfect model of a line-of-sight microwave radio channel.

The simple three-path model was used in Section V to characterize the channel delay difference. By two different methods, it was shown that, when there is 3 dB or more shape present in the channel, the average delay difference is between 5 and 8 ns. We developed a lower bound on the tails of the distribution of delay difference. From these results, which are shown in Fig. 13, we observe that a differential channel attenuation in-band of 3 dB or more may be due to delay differences as great as 43 ns. In another dimension, one would expect to see differential attenuation of 3 dB or more in-band due to delays greater than 20 ns for at least 70 seconds in a heavy fading month. This is comparable to the time the channel attenuation at a single frequency exceeds 40 dB.

---

* For comparisons with the three-path model, it is appropriate to use $\sqrt{19/23}\,\sigma_i$.

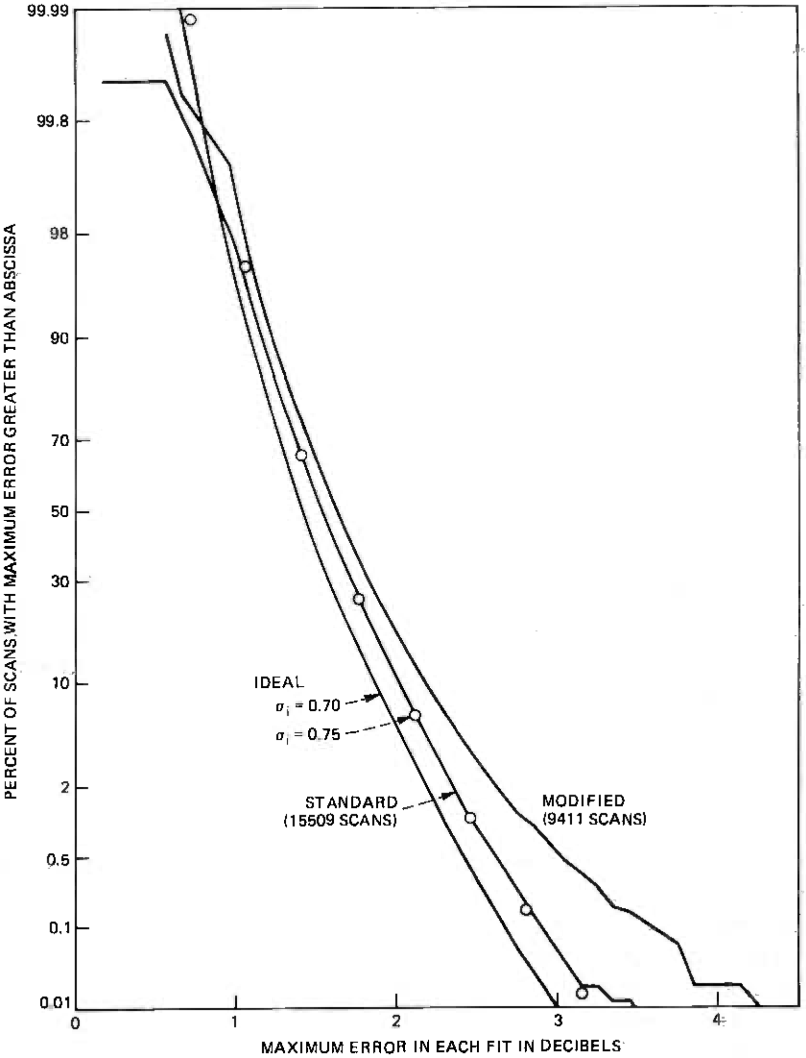

Fig. 19—Distribution of maximum (dB) fit error for two scan subpopulations with fixed delay (6.3 ns) model.

From the error analysis in Section VI, we also conclude that the fixed delay (6.3 ns) model is a very good approximation to the channel for all observed conditions. This conclusion is further substantiated by Figs. 14 and 18, which show the scans for which the fits with the fixed delay model exhibited the largest rms fit error (2.3 dB) and the largest maximum error (3.9 dB), respectively. The fixed delay model is preferable to the three-path model for channel modeling because it requires

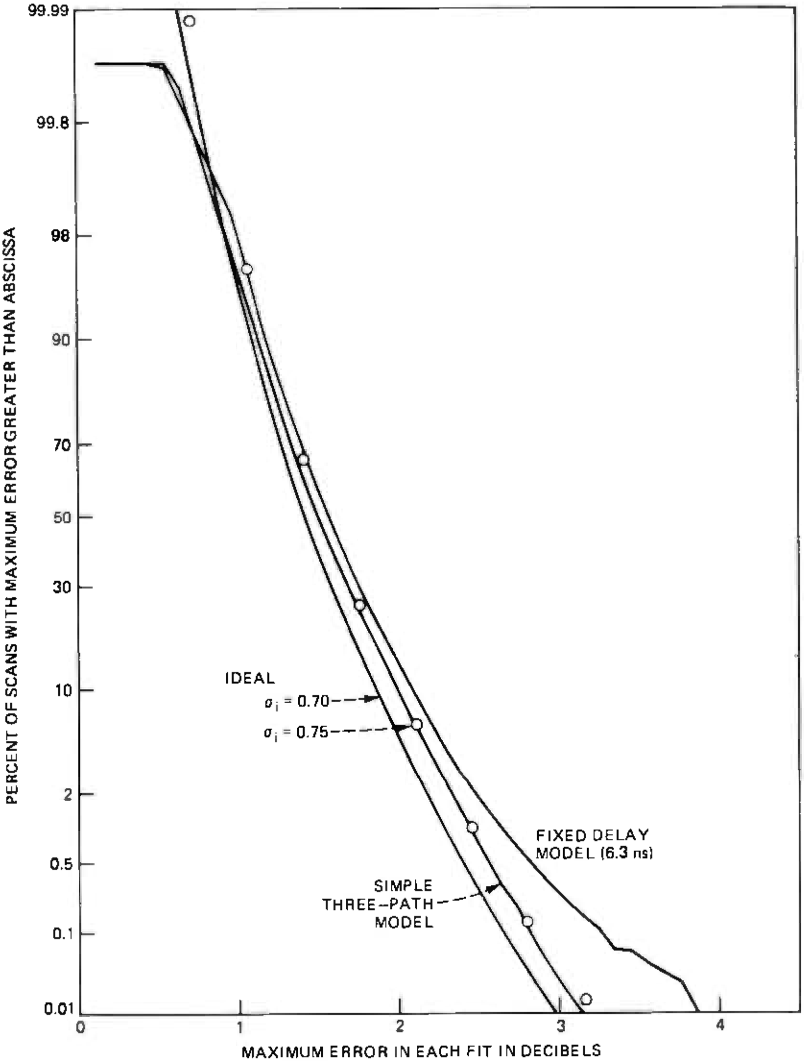

Fig. 20—Distribution of maximum (dB) fit error for composite population with fixed delay and simple three-path models.

only three parameters, and these can always be uniquely determined from a channel amplitude scan.

The statistics of the parameters of the fixed delay model as described in Section IV and shown in Figs. 8 to 12 provide the means of statistically generating all the channel conditions that one expects to see on a nominal hop channel operated at 6 GHz. If one determines, by laboratory test, the parameter values that will cause a particular error rate in a digital radio system, one can easily calculate the time during a heavy fading month that the error rate will equal or exceed this critical value. A companion paper describes the laboratory test and the required calculations.[8]

Future work will be directed toward verifying the model and model statistics with additional fading data obtained both at 6 GHz and at 4 GHz. Using coherent data obtained in 1973, it will be possible to determine the extent to which the channel is actually a minimum phase channel.

VIII. ACKNOWLEDGMENTS

This study would not have been possible without the contributions of many individuals. In particular, the radio equipment was installed, aligned, and maintained by R. A. Hohmann, C. W. Lundgren, and L. J. Morris with instrumentation designed by G. A. Zimmerman. The data processing expertise in setting up and calibrating the data base was provided by M. V. Pursley.

APPENDIX

Estimation of Parameters

The problem of estimating the parameters α, β, and f_o in Section III is equivalent to the problem of determining the first three terms in a subharmonic Fourier series expansion of a function in the frequency domain. Since such expansions are not standard, we provide a complete description of the methodology here.

From eqs. (4) and (9), we may express the weighted mean-square error between estimated and observed power as*

$$E = \frac{\sum C_n(Y_n - \alpha + \beta \cos(\omega_n - \omega_0)\tau)^2}{\sum C_n}. \tag{26}$$

For simplicity, we use a normalized weighting function, d_n, defined by

$$d_n = \frac{C_n}{\sum C_n} \tag{27}$$

so that

$$\sum d_n = 1. \tag{28}$$

In terms of the normalized weighting we may write (26) as

$$E = \sum d_n(Y_n - \alpha + \beta \cos(\omega_n - \omega_0)\tau)^2 \tag{29}$$

---

* Throughout this appendix, all summations are taken over all values of n corresponding to all frequencies observed in a scan.

or in expanded form as

$$
\begin{aligned}
E = \sum d_n Y_n^2 + \alpha^2 + \beta^2 \sum d_n \cos^2(\omega_n - \omega_0)\tau \\
+ 2\beta \sum d_n Y_n \cos(\omega_n - \omega_0)\tau \\
- 2\alpha\beta \sum d_n \cos(\omega_n - \omega_0)\tau - 2\alpha \sum d_n Y_n .
\end{aligned}
\tag{30}
$$

The error E is a minimum when α, β, and ω_0 are chosen so that the partial derivatives of E with respect to α, β, and ω_0 are all equal to zero. Setting the partial derivative of eq. (30) with respect to β equal to zero and solving for β gives

$$
\beta = \frac{\alpha \sum d_n \cos(\omega_n - \omega_0)\tau - \sum d_n Y_n \cos(\omega_n - \omega_0)\tau}{\sum d_n \cos^2(\omega_n - \omega_0)\tau} . \tag{31}
$$

Substituting (31) into eq. (30), we find E_β, the error minimized with respect to β, as

$$
\begin{aligned}
E_\beta = \sum d_n^2 Y_n^2 + \frac{1}{\sum d_n \cos^2(\omega_n - \omega_0)\tau} \\
\cdot \{\alpha^2[\sum d_n \cos^2(\omega_n - \omega_0)\tau - (\sum d_n \cos(\omega_n - \omega_0)\tau)^2] \\
- 2\alpha\,[(\sum d_n Y_n)(\sum d_n \cos^2(\omega_n - \omega_0)\tau) \\
- (\sum d_n \cos(\omega_n - \omega_0)\tau)(\sum d_n Y_n \cos(\omega_n - \omega_0)\tau)] \\
- (\sum d_n Y_n \cos(\omega_n - \omega_0)\tau)^2\}.
\end{aligned}
\tag{32}
$$

Minimizing this with respect to α requires that we set the partial derivative of E_β with respect to α equal to zero. This gives

$$
\alpha = \frac{\begin{gathered}(\sum d_n Y_n)(\sum d_n \cos^2(\omega_n - \omega_0)\tau) - \\ (\sum d_n \cos(\omega_n - \omega_0)\tau)(\sum d_n Y_n \cos(\omega_n - \omega_0)\tau)\end{gathered}}{\sum d_n \cos^2(\omega_n - \omega_0)\tau - (\sum d_n \cos(\omega_n - \omega_0)\tau)^2} . \tag{33}
$$

Substituting (33) into (32) gives $E_{\alpha\beta}$, the error minimized with respect to both α and β, as

$$
\begin{aligned}
E_{\beta\alpha} = \sum d_n Y_n^2 - \bar{Y}^2 \\
- \frac{(\sum d_n (Y_n - \bar{Y}) \cos(\omega_n - \omega_0)\tau)^2}{\sum d_n \cos^2(\omega_n - \omega_0)\tau - (\sum d_n \cos(\omega_n - \omega_0)\tau)^2} ,
\end{aligned}
\tag{34}
$$

where

$$
\bar{Y} = \sum d_n Y_n . \tag{35}
$$

We note that we could have obtained this same expression by first minimizing with respect to α and then with respect to β; however, one obtains different but equivalent expressions for α and β, depending on the order of differentiation. We develop the alternative expressions for α and β in the following paragraphs.

Let us define some new quantities to simplify these expressions. Let the difference between the observed power and the weighted mean power in the band be designated by X_n; then

$$X_n = Y_n - \sum d_n Y_n = Y_n - \bar{Y}. \tag{36}$$

If we also define the quantities

$$X_c = \sum d_n X_n \cos \omega_n \tau, \tag{37}$$

$$X_s = \sum d_n X_n \sin \omega_n \tau, \tag{38}$$

$$D_a = \sum d_n \cos^2(\omega_n - \omega_0)\tau, \tag{39}$$

$$D_b = \sum d_n \cos(\omega_n - \omega_0)\tau, \tag{40}$$

we may rewrite α and β from eqs. (31) and (33) as

$$\alpha = \bar{Y} - \frac{[X_c \cos \omega_0\tau + X_s \sin \omega_0\tau]D_b}{D_a - D_b^2} \tag{41}$$

and

$$\beta = \frac{1}{D_a}\{(\alpha - \bar{Y})D_b - (X_c \cos \omega_0\tau + X_s \sin \omega_0\tau)\}. \tag{42}$$

Using (41) to eliminate α from (42), we obtain

$$\beta = -\frac{X_c \cos \omega_0\tau + X_s \sin \omega_0\tau}{D_a - D_b^2}. \tag{43}$$

We may use (43) in (41) to obtain

$$\alpha = \bar{Y} + \beta D_b. \tag{44}$$

Equations (43) and (44) are the estimators that would have been obtained if the order of taking partial derivatives in the preceding development had been reversed. It is apparent that, after one has estimated ω_0, one may estimate α and β by using either eqs. (41) and (42), (43) and (44), or eqs. (41) and (43).

The estimate of ω_0 that minimizes the weighted error is obtained by minimizing $E_{\beta\alpha}$ with respect to ω_0. Using eqs. (35) to (40) in eq. (34), we write

$$E_{\beta\alpha} = \sum d_n X_n^2 - \frac{[X_c \cos \omega_0\tau + X_s \sin \omega_0\tau]^2}{D_a - D_b^2}. \tag{45}$$

To see the explicit dependence of $E_{\beta\alpha}$ on ω_0, we define the following quantities

$$d_c = \sum d_n \cos^2 \omega_n\tau - \left(\sum d_n \cos \omega_n\tau\right)^2, \tag{46}$$

$$d_s = \sum d_n \sin^2 \omega_n \tau - \left(\sum d_n \sin \omega_n \tau\right)^2, \tag{47}$$

$$d_{cs} = \sum d_n \cos \omega_n \tau \sin \omega_n \tau - \left(\sum d_n \cos \omega_n \tau\right)\left(\sum d_n \sin \omega_n \tau\right). \tag{48}$$

Substituting these into (45) gives

$$E_{\beta\alpha} = \sum d_n X_n^2 - \frac{[X_c \cos \omega_n \tau + X_s \sin \omega_0 \tau]^2}{d_c \cos^2 \omega_0 \tau + 2 d_{cs} \cos \omega_0 \tau \sin \omega_0 \tau + d_s \sin^2 \omega_0 \tau}. \tag{49}$$

Setting the partial derivative of $E_{\beta\alpha}$, as given by (49), equal to zero gives the estimator for ω_0 as

$$\omega_0 \tau = \mathrm{Tan}^{-1}\left[\frac{d_c X_s - d_{cs} X_c}{d_s X_c - d_{cs} X_s}\right]. \tag{50}$$

Obviously, two values of $\omega_0 \tau$ in the interval $(-\pi, \pi]$ will satisfy eq. (50). One of these, the principal value, lies in the interval $(-\pi/2, \pi/2]$, the other differs from the first by $\pm\pi$. We shall show that the two solutions are equivalent, but that our chosen solution is unique.

If we replace $\omega_0 \tau$ by $\omega_0 \tau \pm \pi$ in eqs. (39), (40), (43), (44), and (45), we see that D_b and β change sign and α and $E_{\beta\alpha}$ are unchanged. Since we want the solution with β greater than zero, we take the principal value solution to (50) if the resulting estimate of β is positive. Otherwise we add or subtract π to obtain a positive value for β and a value of $\omega_0 \tau$ in the appropriate interval.

While we could substitute the result of eq. (50) into (49) to obtain the minimum error, $E_{\alpha B \omega_0}$, it is more generally useful to evaluate $E_{\alpha\beta}$ for the optimum ω_0. This is especially true when we do not use the optimum ω_0, as given by eq. (50). The simplest form for $E_{\alpha\beta}$ is obtained by substituting (43) into (45) to give

$$E_{\alpha\beta} = \sum d_n X_n^2 - (D_a - D_b^2)\beta^2. \tag{51}$$

These equations were implemented, with the modifications described in Section 3.2, to obtain all the fits described in this paper.

REFERENCES

1. G. M. Babler, "A Study of Frequency Selective Fading for a Microwave Line-of-Sight Narrowband Radio Channel," B.S.T.J., *51*, No. 3 (March 1972), pp. 731–757.
2. G. M. Babler, "Selectively Faded Nondiversity and Space Diversity Narrowband Microwave Radio Channels," B.S.T.J., *52*, No. 2 (February 1973), pp. 239–261.
3. L. J. Greenstein, "A Multipath Fading Channel Model for Terrestrial Digital Radio," IEEE Trans. Commun. Tech., *COM-26*, No. 8 (August 1978), pp. 1247–1250.
4. R. L. Kaylor, "A Statistical Study of Selective Fading of Super-High Frequency Radio Signals," B.S.T.J., *32*, No. 5 (September 1953), pp. 1187–1202.
5. G. M. Babler, unpublished work.
6. W. C. Jakes, Jr., "An Approximate Method to Estimate An Upper Bound on the Effect of Multipath Delay Distortion on Digital Transmission," ICC '78 Conference Record, June 1978, *3*, pp. 47.1.1–5.
7. W. D. Rummler, "A Multipath Channel Model for Line-of-Sight Digital Radio Systems," ICC '78 Conference Record, June 1978, *3*, pp. 47.5.1–4.
8. C. W. Lundgren and W. D. Rummler, "Digital Radio Outage Due to Selective Fading—Observation vs Prediction from Laboratory Simulation," B.S.T.J., this issue, pp. 1073–1100.

Copyright © 1979 American Telephone and Telegraph Company
THE BELL SYSTEM TECHNICAL JOURNAL
Vol. 58, No. 5, May–June 1979
Printed in U.S.A.

Digital Radio Outage Due to Selective Fading—Observation vs Prediction From Laboratory Simulation

By C. W. LUNDGREN and W. D. RUMMLER

(Manuscript received July 7, 1978)

A statistical model (introduced in a companion paper) of fading on a radio path is used with laboratory measurements on a digital radio system to estimate the outage due to multipath fading, where outage is the time that the bit error rate (BER) exceeds a threshold. Over the range of BER of interest (10^{-6} to 10^{-3}), the calculated outage agrees favorably with the outage observed during the period for which the fading model was developed. It is further shown that the calculated outage, when scaled to a heavy fading month on the basis of single-frequency, time-faded statistics, agrees equally well with the outage observed on the same path during a heavy fading month. The agreement between measured and predicted outage substantiates the selective fading model. The prescribed laboratory measurements characterize the sensitivity of the radio system to selective fading. Thus, the methodology provides a useful basis for comparing the outage of alternative realizations of digital radio systems.

I. INTRODUCTION

Present interest in using high-speed common carrier digital radio[1-5] has precipitated a need for estimating the performance of such systems during periods of selective (multipath) fading. This paper describes a method of characterizing a digital radio system in the laboratory which allows the outage to be accurately estimated. For a digital radio system, outage requirements are stated in terms of the number of seconds in a time period (usually a heavy fading month) during which the bit error rate (BER) may exceed a specified level; typically, 10^{-3} or 10^{-4} is appropriate to voice circuit application.

The method is based upon a statistical channel model[6] developed from measurements on an unprotected 26.4-mile hop in the 6-GHz band in Palmetto, Georgia in 1977 using a general trade 8-PSK digital radio system as a channel measuring probe. The modeled fading occurrences were scaled to the basis of a heavy fading month using the occurrence of time faded below a level at a single frequency as the means of calibration. The bit error rate performance of the digital radio system was measured during the time period used for channel modeling and for an extended period corresponding to a heavy fading month. This same radio system was later subjected to a measurement program in the laboratory using a multipath simulator which provides a circuit realization of the fading model. The measured results are used with the channel model to determine the occurrence of channel conditions which will cause the BER to exceed a given threshold. Comparisons on the basis of the modeling period and a heavy fading month show good agreement between calculated and observed outages for BERs between 10^{-6} and 10^{-3}.

The properties of the fixed-delay channel model are reviewed briefly in Section II as a basis for describing the measurements and for the subsequent outage calculations. This three-parameter channel model is realized in the laboratory by an IF fade simulator. The simulator and its use in obtaining the necessary laboratory data are described in Section III. The procedures to be followed in calculating outage times for a given BER are described in Section IV. Calculated and observed outage times are compared in Section V. Conclusions are provided in Section VI.

II. MODEL DESCRIPTION—METHODOLOGY

It has been demonstrated[6] that the complex voltage transfer function of a line-of-sight microwave radio channel is well modeled by the function

$$H(\omega) = a\,[1 - be^{-j(\omega-\omega_0)\tau}] \tag{1}$$

with τ fixed. A 6-GHz channel (30-MHz bandwidth) has been characterized statistically by the model with $\tau = 6.3$ ns. Such a channel has a power transfer function given by

$$|H(\omega)|^2 = a^2[1 + b^2 - 2b\cos(\omega - \omega_0)\tau] \tag{2}$$

and an envelope delay distortion function, i.e., the derivative of the phase of $H(\omega)$ with respect to ω, given by

$$D(\omega) = \frac{b\tau(\cos(\omega-\omega_0)\tau - b)}{1 + b^2 - 2b\cos(\omega-\omega_0)\tau}. \tag{3}$$

In the following paragraphs, we summarize the properties of the model, the statistics of the model parameters, and the measurement objectives.

2.1 Fixed delay model

A plot of the attenuation produced by the fixed delay model of eq. (1) is shown in Fig. 1. Since the delay is fixed at 6.3 ns, the spacing between nulls of the response, 158.4 MHz, is much larger than the channel bandwidth. The parameters a and b control the depth and shape of the simulated fade, respectively. The parameter $f_o(=\omega_0/2\pi)$ determines the position of the fade minimum or notch. Both the notch frequency, f_o, and the response frequency, f, are measured from the center of the 30-MHz channel for convenience.

The model function of eq. (1) may be interpreted as the response of a channel which provides a direct transmission path with amplitude a and a second path providing a relative amplitude b at a delay of 6.3 ns and with a phase of $\omega_0\tau + \pi$ (independently controllable) at the center frequency of the channel. This interpretation is represented in Fig. 2 by a phasor diagram at $\omega = 0$, the center frequency of the channel. Varying the frequency, ω, over the channel bandwidth (30 MHz) moves the angle of the interfering ray through an arc of about 60 degrees ($2\pi \times 30$ MHz $\times$ 6.3 ns $\approx \pi/3$), centered at the position shown. This diagram is useful for understanding the fade simulation; it also provides an alternate means of describing the position of the notch. The notch position may be specified by its frequency, f_o, or by ϕ, the angle of the interfering path at the center of the channel.

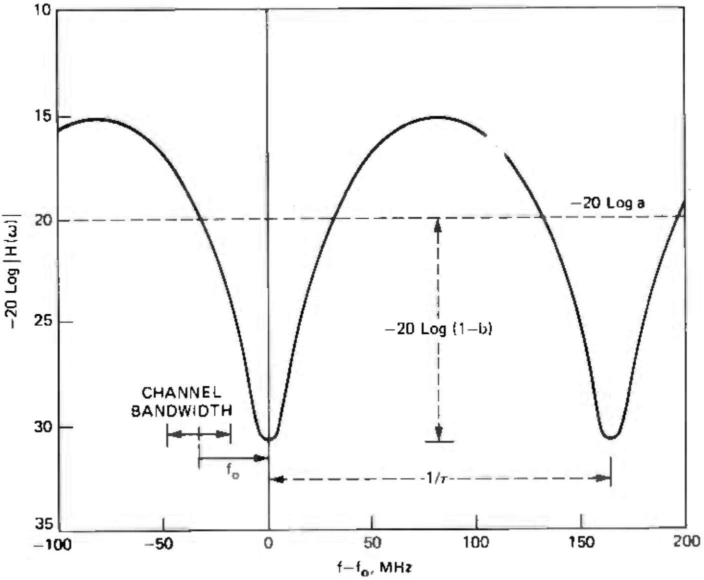

Fig. 1—Attenuation of channel model function, $H(\omega) = a[1 - b\exp(-j(\omega - \omega_0)\tau)]$, for $\tau = 6.3$ ns, $a = 0.1$, $b = 0.7$.

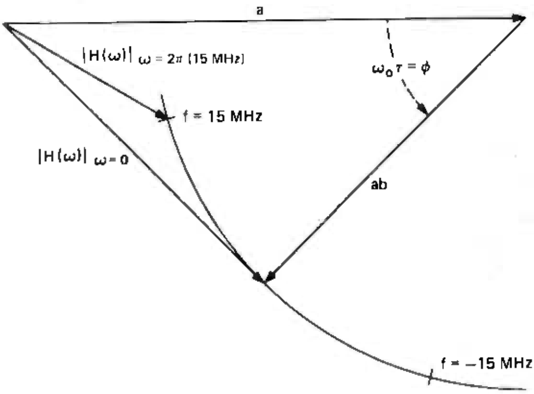

Fig. 2—Phasor diagram of a modeled fade, $\phi = 45°$, $b = 0.7$.

From Figs. 1 and 2, or eq. (1), it may be seen that varying a changes the overall level and varying b changes the shapeliness of the modeled fade. Furthermore, if the minimum is within the 30-MHz channel bandwidth ($|\phi| < 30°$), the fixed delay model can generate notches with a wide range of levels and notch widths. With the minimum out of band, it can generate a wide range of combinations of levels, slopes, and curvatures within the channel bandwidth.

2.2 Model statistics

The statistics of the model parameters were obtained from a selected data base during which heavy fading activity was observed.[6] The distribution of b is best described in terms of $B = -20 \log(1 - b)$. Figure 3 shows the distribution of B and the least-squares straight line fit to the distribution over the region where it best represents selective fading—between B values of 3 and 23 dB. The channel is described by B greater than 23 dB for less than 0.15 percent of the observed time which makes the distribution less certain beyond this point. At the other extreme, during the periods of time when there is little or no selective fading, the channel is characterized by values of B less than 3 dB. Thus, the fitted line represents a lower bound on the distribution for B less than 3 dB. Since the fitted line has an intercept of 5400 seconds, we may model the fraction of 5400 seconds during which B exceeded a value X by the probability distribution

$$P(B > X) = e^{-X/3.8}. \tag{4}$$

Thus the probability of finding a value of B between X and $X + dX$ is

$$p_B(X)\ dX = \frac{dX}{3.8} e^{-X/3.8}. \tag{5}$$

The distribution of a is lognormal with a standard deviation of 5 dB and a mean that is dependent on B (or b). Hence, the probability that

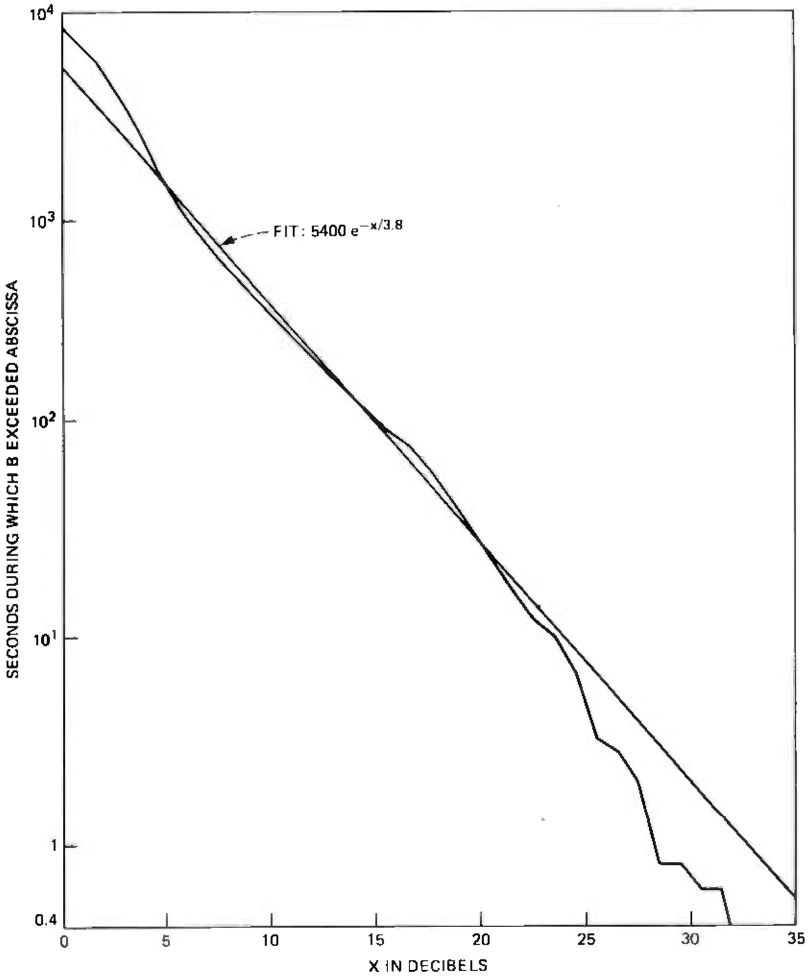

Fig. 3—Distribution of B for model data base period.

$A = -20 \log a$ has a value between Y and $Y + dY$ is given by

$$p_A(Y)\, dY = \frac{dY}{5\sqrt{2\pi}}\, e^{-[Y - A_0(B)]^2/50}. \tag{6}$$

The relationship between A_0, the mean of the distribution, and B is given in Fig. 4.

The distribution of f_o is found to be independent of A and B. It is usually simpler to work with ϕ rather than f_o. The two variables are simply related in that ϕ is defined on the interval $(-\pi, \pi)$ and a 2.5-degree change in ϕ corresponds to a 1.1-MHz change in f_o. For the fixed delay model, the variable ϕ has been found to have a probability density function that can be described as uniform at two levels, with

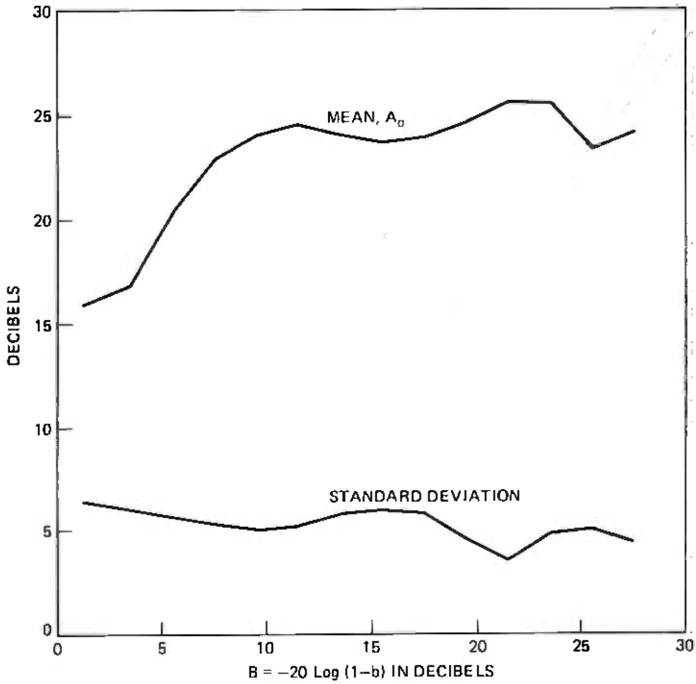

Fig. 4—Mean and standard deviation of the distribution of $A = -20 \log a$ as a function of B.

values less than $\pi/2$ being five times more likely than values greater than $\pi/2$. Thus, we have the probability density function per degree as:

$$p_\phi(\phi) = \begin{cases} \dfrac{1}{216} & |\phi| < 90^\circ \\ \\ \dfrac{1}{1080} & 90^\circ \le |\phi| \le 180. \end{cases} \tag{7}$$

The functions in eqs. (5) to (7) can be used to determine the probability of finding a, b, and f_o in some region of a-b-f_o space. This probability can be converted to number of seconds in the observation period by multiplying by 5400 seconds. To convert this probability to the number of seconds in a month requires scaling the data base. The scaling may be obtained from Fig. 5 which shows, for several frequencies in the band, the time during the model data base period that the channel was faded below a given level. Distributions are shown for average power in the band and for power at selected frequencies at the center and near the edges of the radio channel. (Frequencies indicated are at IF where the center frequency is at 70 MHz.) For the path used,

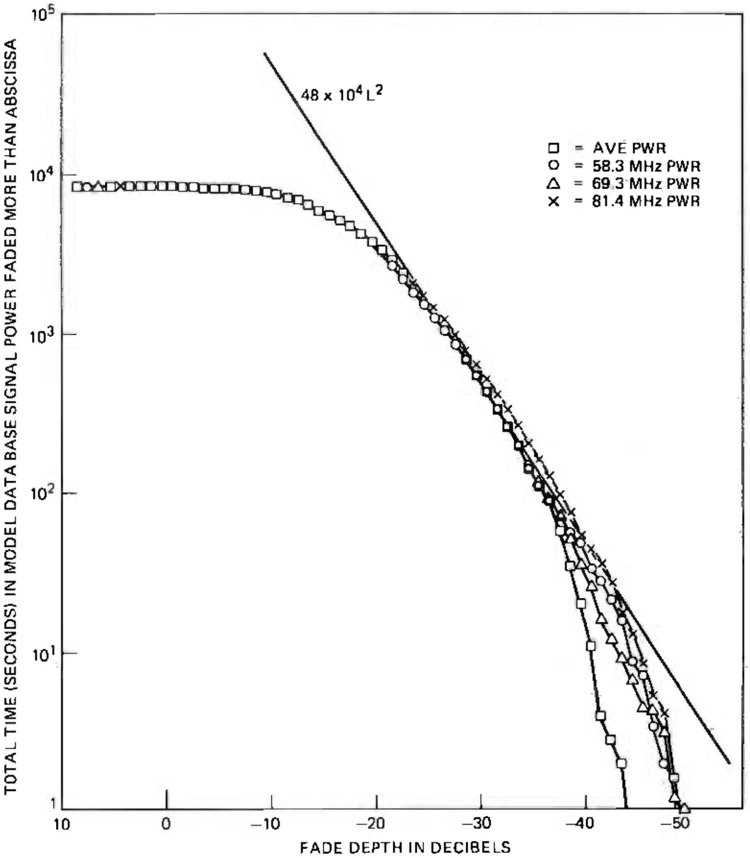

Fig. 5—Amplitude distributions for model data base period.

one expects the received voltage (single frequency) relative to midday average to be less than L for $72.5 \times 10^4\ L^2$ seconds in a month.[7] For the data base used, the fading is best described by $48 \times 10^4\ L^2$ hence, the data represent ⅔ of a fading month. To obtain outage on a seconds-per-heavy-fading-month basis, the probabilities calculated with eqs. (5) to (7) must be multiplied by 5400×1.5 or 8100 seconds.

2.3 Outage estimation

The fixed delay model described above can be simulated with an equivalent circuit laboratory measurement to determine the equipment response to multipath fading. Conceptually, one determines critical values of A and B for which a specified error rate is achieved for each fade notch position. In practice, it is difficult to maintain a constant BER; it is more expedient to fix b and vary the carrier-to-noise ratio (a) while plotting the BER. From the resulting curves, one may compute critical contours of A and B for each prescribed notch location and BER. Using eqs. (5) and (6), the probability that A and B lie on the high error rate side of a given critical contour may be calculated.

By repeating this calculation for a uniform set of notch positions and using (7) to determine the probability weighting given to each and summing, one may estimate the probability of all selective fades that produce a BER exceeding the prescribed one. Multiplying this probability by 5400 gives the outage time expected over the data base period; multiplying by 8100 gives the expected outage time per heavy fading month.

The following section describes the laboratory measurement; Section IV describes the reduction of the measured curves and parameters to outage times.

III. LABORATORY MEASUREMENTS

Figure 6 illustrates stressing of a digital radio system by means of an IF fade simulator. The simulator, which is inserted after linear IF preamplification but before any high-gain amplification, shapes both the desired signal and the effective received noise. It is necessary to operate the simulator at a sufficiently large input carrier-to-noise ratio that the concomitantly shaped noise at its output remains a negligible contributor to degraded system performance throughout the operating range of interest.

Within its restricted frequency range of operation, the IF simulator is adjusted to achieve those specific shapes implied by Fig. 2. Although the measurements could have been made using an RF fade simulator, the choice of an IF simulator was based primarily upon considerations of signal and noise levels, and the repeatability of adjustments. The following section describes an IF shape-stressing measurement in the minimum detail necessary to qualify the data collected.

3.1 Representative IF two-path fade stressing measurement

The block diagram of Fig. 7 illustrates an arrangement employing an IF fade simulator and an IF flat noise source. A pseudo-random test

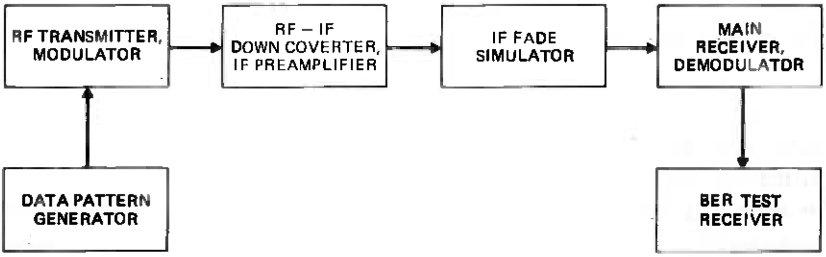

Fig. 6—IF fade stressing.

pattern modulates the 6-GHz radio transmitter whose output is nominally 5 watts (ⓐ, in Fig. 7). The output spectrum is usually shaped by a bandpass filter following the microwave power amplifier to comply with FCC regulations.

To enable back-to-back operation of the transmitter and receiver of a single repeater which normally operate on different radio channels, a radio test translator was employed. The translator output power was approximately −30 dBm (adjustable, at ⓑ) to simulate the unfaded received signal level (RSL) observed typically in the field.

Assuming a linear RF-IF conversion gain of 20 dB, the signal power at the input (ⓒ) to the IF fade simulator is −10 dBm. The simulator incorporates low-noise linear amplification. A reference insertion loss for the main unfaded ray is 10 dB, including the output power summer. Hence the maximum desired signal power at the input to the main IF amplifier (ⓔ) is −20 dBm.

Assuming a 30-MHz receiver noise bandwidth and a current-art receiving system noise figure of 5 dB, the total system noise power is approximately −95 dBm, referred to the receiver's input port. This results in a flat receiver noise contribution of −85 dBm at input ⓔ to the main IF amplifier. Consequently, the maximum attainable carrier to simulator-shaped RF noise ratio is 10 log (C_0/N_{rf}) = −20 − (−85) = 65 dB. The noise contributed by the fade simulator amplifiers must not exceed −100 dBm, to be negligible.

Flat IF noise much larger than the unwanted and shaped system noise is added artificially at ⓔ and is adjusted in magnitude by a calibrated attenuator ⓓ to superpose thermal noise degradations upon the simulated selective fading degradations of the desired signal. One would ideally measure the added IF noise power in the final predetection bandwidth of the digital radio system, or twice the Nyquist bandwidth. It is more convenient in the laboratory to reference carrier-to-noise ratios to the output of the main IF amplifier by using the precalibrated AGC voltage (assuming that wideband AGC detection is employed), to measure both the unshaped signal and noise powers. The carrier-to-noise ratio at the detector would be higher—by the ratio of the system noise bandwidths that would be measured at the respective points.

The noise source output in Fig. 7 may be adjusted so that an attenuator setting of 0 dB ⓓ results in a noise power equivalent to that of the unfaded signal power (the attenuator is then calibrated directly in uncorrected C_0/N_{if}, in dB). As the IF fade simulator is readjusted to achieve different prescribed fade shapes, its mean insertion loss may also change. The change in insertion loss is determined by monitoring the change in signal power at ⓔ; the same loss increment (dB) must be added to the noise attenuator ⓓ to reestablish the 0 dB reference.

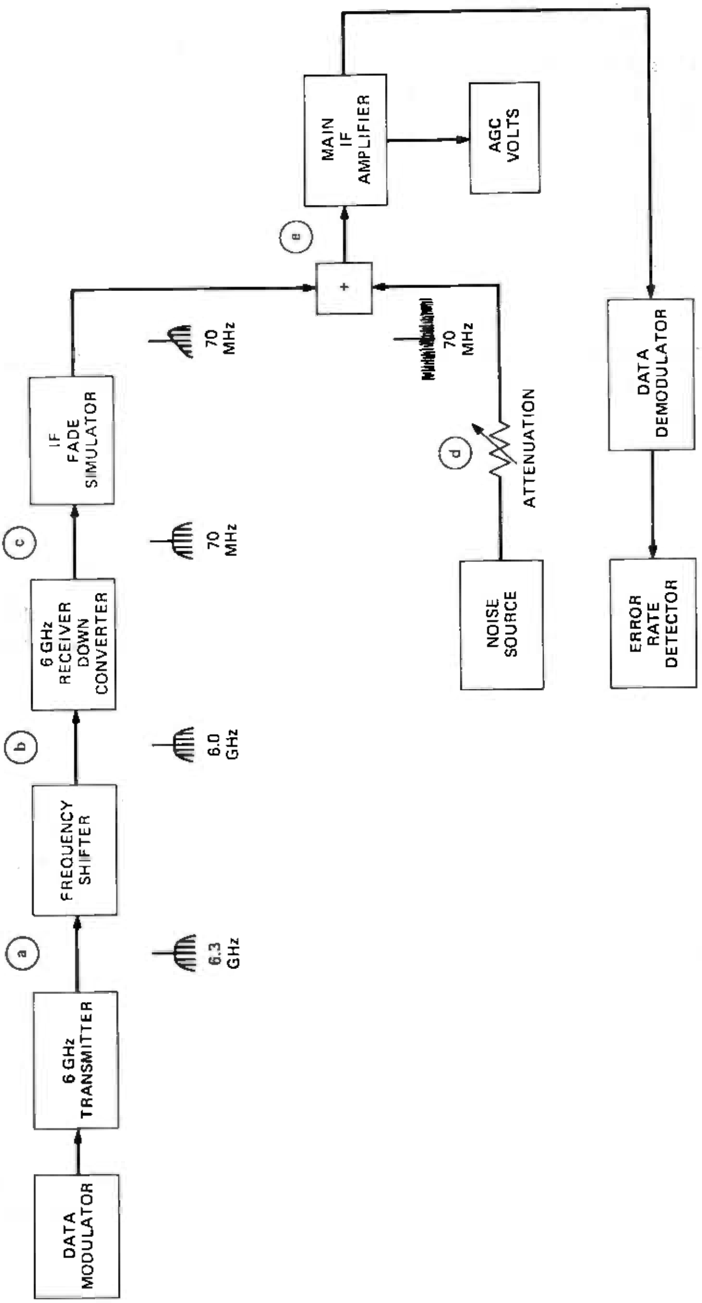

Fig. 7—Laboratory test arrangement.

3.2 IF two-path fade simulator

Figure 8 illustrates splitting the desired IF signal into an arbitrarily phased, adjustable "main" component and a "delayed" component fixed in delay (τ ns) but adjustable in magnitude. The main component is further resolved into orthogonal components (inset to Fig. 8) using wideband networks exhibiting flat gain and well-behaved delay. A particular sum vector is constructed by adjusting the orthogonal components to establish a simulated fade notch frequency; in practice, the phase sense of 0- and 90-degree components are independently reversible, as indicated by the switches in the figure, for complete flexibility in notch frequency selection.

The 6.3-ns fixed delay added to the delayed path imparts a phase shift of 159 degrees at the 70-MHz IF center frequency. This is shown built out to 225 degrees, relative to the 0-degree transmission path, using a 66-degree wideband network of the same type. The delayed vector is fixed in direction opposite the midrange position of the adjustable main vector, corresponding to a channel-centered fade (ϕ = 0 degrees).

Since $1/\tau = 158.4$ MHz, a change of 1 degree in direction of the main vector corresponds to a frequency displacement of the fade notch location of 0.44 MHz. For $\phi = -45$ degrees, the notch location is displaced 19.8 MHz below the channel center ($f_o = -19.8$ MHz). The magnitude of the delayed component is then adjusted to achieve the desired notch depth.

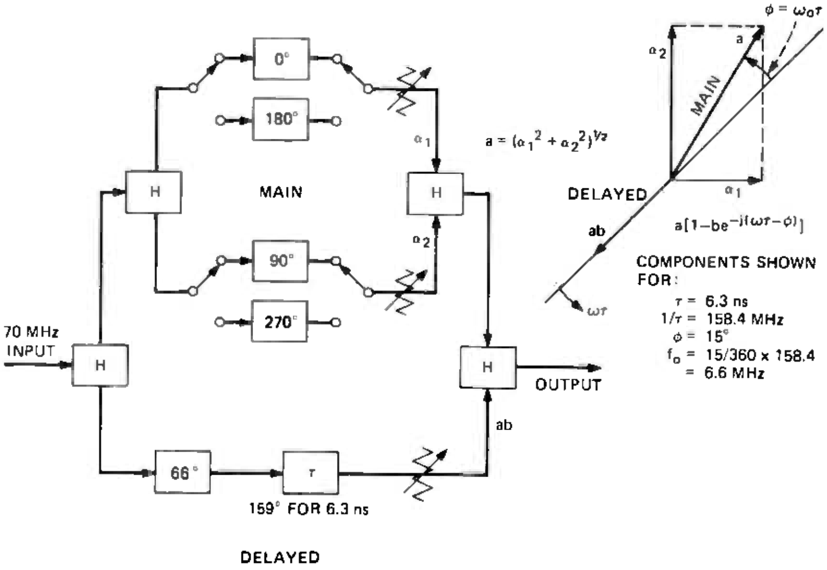

Fig. 8—IF fade simulator—conceptual block diagram.

3.3 Digital radio performance stressed by in-band selectivity and thermal noise

The radio equipment was measured at uniformly spaced notch frequencies separated by 4.4 MHz ($\Delta\phi = 10$ degrees). To fully characterize a period of variation in ϕ, or f_o, one would need to make 36 sets of measurements. *Ideally,* half may be omitted because of symmetry. For given values of A and B, the same error rate should obtain for a notch at a given frequency displacement above or below the channel band center. Variations in B ought not to have a significant effect for $|\phi|$ greater than 90 degrees. It was determined that detailed measurements were required for nine different values of f_o to characterize the digital radio tested.

Using a wideband RF fade simulator in the field, the digital radio performance for out-of-channel notch locations was relatively independent of whether minimum or nonminimum-phase fade simulations were employed. The nonminimum phase fade is modeled by eq. (1) with the sign of the phase term reversed. This leaves the amplitude [eq. (2)] unchanged, but reverses the sign of the envelope delay distortion [eq. (3)]. We conclude that the minimum phase channel model is sufficiently general for use in simulating the channel and in estimating performance.

The IF fade simulator was adjusted for each notch frequency, and the depth of notch was varied by adjusting the magnitude of the delayed component. Then various amounts of IF thermal noise were added. Figure 9 typifies the performance data collected. BERs are plotted *versus* the uncorrected IF carrier-to-noise ratio (C/N_{if}), for a constant fade notch offset from midchannel ($f_o = -19.8$ MHz, $\tau = 6.3$ ns). Each curve corresponds to a different notch depth ($B = -20 \log(1-b)$ dB), and hence a different amplitude and delay shape in the radio channel. Each curve is also identified with an in-band selectivity, defined as the difference between the maximum and minimum attenuation present in the (25.3-MHz) channel bandwidth. The lower-left "baseline" curve presents the unshaped signal, flat fading performance obtained by adding only IF thermal noise. This curve was verified (without the added IF noise) by attenuating the received RF input signal in the back-to-back configuration.

Consideration was given to matching the order of measurements to characteristics of the particular digital radio tested. For example, considerable scattering of data at low error rates can result from synchronizations involving different reference carrier phases. The authors elected to perform several synchronizations while observing the BER for each phase, and then chose that phase giving the worst performance.* Synchronization was accomplished at the low error rate

---

* Because the phase information in the measured system was Gray coded and digital access was on a per-rail basis, one rail had twice the BER of the other two. All measurements in the field and in the laboratory were made on this worst-case rail.

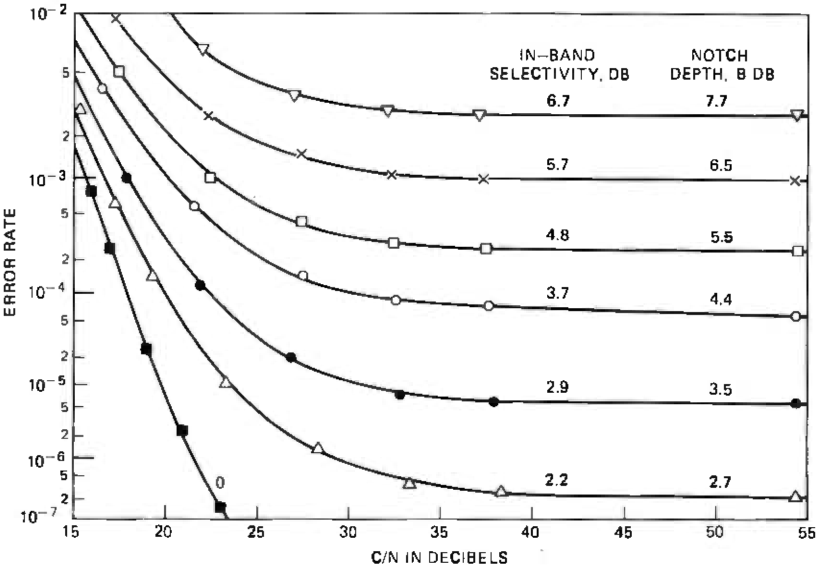

Fig. 9—High-speed digital radio IF dispersive fade simulations, $\tau = 6.3$ *ns*, $f_0 = -19.8$ MHz.

(bottom) of each curve, and this phase relationship was maintained for all data points obtained for each curve.

From the baseline curve of Fig. 9, a BER $= 1 \times 10^{-6}$ obtains for 10 $\log(C/N_{if}) \doteq 21.5$ dB. For the digital radio system installed on the instrumented hop and reported in the figure, the measured flat fade margin for a threshold BER $= 1 \times 10^{-6}$ was 40.5 dB This leads to an unfaded IF carrier-to-noise ratio 10 $\log(C_0/N_{if}) \doteq 21.5 + 40.5 = 62$ dB.

From the baseline curve for a BER $= 1 \times 10^{-7}$, note that insertion of a fade whose notch depth is 6.5 dB results in four orders of magnitude degradation in BER performance; equivalently, an in-band selectivity of only 5.7 dB in 25.3 MHz results in a BER $> 1 \times 10^{-3}$.

The asymptotic regions in Fig. 9, corresponding to high values of C/N_{if}, are not normally presented in characterizations of this type; however, system outage depends primarily upon the performance in these asymptotic regions. Thus, under typical fading conditions, the transmitted carrier power might be increased at will without improving the BER significantly. The effects of decreasing the carrier power are discussed in Section 4.4.

A family of curves like those shown in Fig. 9 was obtained (but are not given here) for each of nine uniformly spaced frequency offsets below midchannel to characterize the digital radio system sufficiently for the prediction of outage. A number of spot checks were also made using both RF and IF fade simulators at symmetrical positive and negative offset frequencies, to establish that acceptable symmetry existed.

IV. CALCULATION OF OUTAGE

This section describes four methods of calculating outage. The derivation of the critical curves of A and B, which provide the basis for making and understanding these calculations, is given in Section 4.1. In Section 4.2 the detailed calculation of outage from the critical A-B curves is described. It is shown in Section 4.3 that for the present system this method may be greatly simplified by calculating only selectivity-caused outage (i.e., neglecting thermal noise). Section 4.4 presents an approximate method of accounting for the effects of thermal noise. Section 4.5 provides a basis for estimating the selectivity-caused outage from a single measurement.

4.1 Derivation of critical characteristics

To calculate the outage for a fixed bit error rate, one must first obtain the critical curves of A and B at each simulated value of f_o, the notch position. Thus, from Fig. 9 which corresponds to $f_o = -19.8$ MHz (or $\phi = -45°$), we obtain six points on the critical curve of A and B for a BER of 10^{-3}, one point from each of the six curves which cross the critical BER. The value of B is obtained from the value of b since

$$B = -20 \log(1 - b). \tag{8}$$

For the curve in Fig. 9 corresponding to $B = 4.4$ dB, we obtain the corresponding critical value of A for a BER of 10^{-3} from the value of carrier-to-noise ratio, which is 20.2 dB where this curve crosses the 10^{-3} BER line. Since the carrier-to-noise ratio is 62 dB when the channel is unfaded, the 20.2 dB value corresponds to a relative average power loss of 41.8 dB,

$$L_s = 62 - 20.2 = 41.8 \text{ dB}. \tag{9}$$

Without loss of generality, we assume that the PSK signal has a rectangular spectrum of width f_b; consequently, the relative power transmitted by the model is obtained from eq. (2) as*

$$\begin{aligned} P_{av} &= \frac{1}{2\pi f_b} \int_{-\pi f_b}^{\pi f_b} |H(\omega)|^2 \, d\omega \\ &= a^2 \left\{ 1 + b^2 - 2b \cos 2\pi f_o \tau \left(\frac{\sin \pi f_b \tau}{\pi f_b \tau} \right) \right\}. \end{aligned} \tag{10}$$

---

* The calculated result is not critically dependent on the flatness of the signal spectrum or the spectral width chosen. We have used for f_b a value of 25.3 MHz as representing the effective width of the signal.

Defining a correction term by

$$C = -10 \log\left\{1 + b^2 - 2b \cos 2\pi f_o\tau\left(\frac{\sin \pi f_b\tau}{\pi f_b\tau}\right)\right\}, \tag{11}$$

we may express the signal loss as

$$L_s = -10 \log P_{av} = A + C. \tag{12}$$

Thus, we obtain the critical value of A as

$$A = L_s - C. \tag{13}$$

For $B = 4.4$ dB ($b = 0.4$) and $f_o = -19.8$ MHz, we find $C = 2.06$ dB and the critical value of A is $41.8 - 2.1 = 39.7$ dB.

Carrying out these calculations for the six curves in Fig. 9, one can generate the critical curve of A and B for $f_o = -19.8$ MHz and a BER of 10^{-3}. The curve is shown in Fig. 10 along with the critical curves for several other values of the BER. A complete set of curves must be generated for all values of f_o.

The curves in Fig. 10 are typical of the critical curves obtained for $|f_o| \leq 33$ MHz. The intercept with the A-axis represents the flat fade margin for the given BER; this margin is independent of notch position. The intercept of a critical contour with the B-axis represents the shape, or relative fade depth, margin for the given notch position. For values of B to the right of this intercept, the critical value of BER cannot be obtained at any carrier-to-noise ratio for the given notch position.

4.2 Outage calculation—detailed method

The probability, P_o, of finding A and B outside all critical contours may be written with eqs. (5), (6), and (7) as

$$P_o = \int_{-\pi}^{\pi} p_\phi(\phi) P_c(\phi)\, d\phi, \tag{14}$$

where

$$P_c(\phi) = \int_0^\infty \int_{A_c(X)}^\infty p_A(Y) p_B(X)\, dY\, dX, \tag{15}$$

and $A_c(X)$ is the functional relation of the critical values of A to B (or X), for B less than B_c, the B-axis intercept, and for a given BER and ϕ value.* Since measurements were made for a uniformly spaced set of notch positions with spacing $\Delta\phi = 10°$, we may approximate (14) by

---

* The dependence of the function $A_c(X)$ and the asymptote B_c on BER and ϕ is not explicitly denoted to keep notation simple.

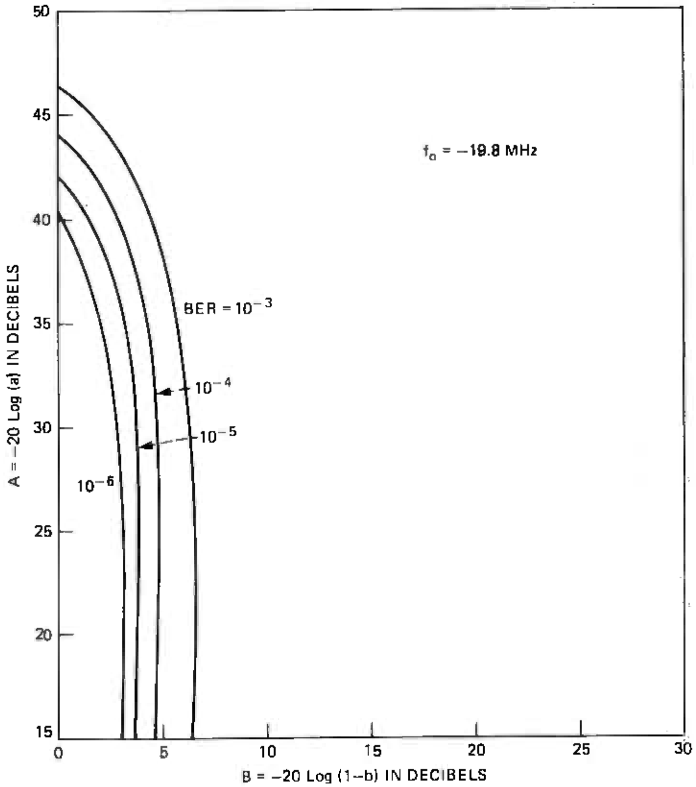

Fig. 10—Critical curves of A and B for $f_o = -19.8$ MHz.

$$P_o = \Delta\phi \sum_{\text{All } \phi_i} p_\phi(\phi_i) P_c(\phi_i). \tag{16}$$

To illustrate the calculation of outage probability with eqs. (15) and (16), we shall calculate the term in the summation of eq. (16) corresponding to a BER of 10^{-3} and $\phi_i = -45°$ (or $f_o = -19.8$ MHz). From Fig. 11, which is taken from Fig. 10, we note that the double integral in eq. (15) may be broken into integrations over two regions. Thus

$$P_c(\phi_i) = \int_{B_c}^{\infty}\int_{-\infty}^{\infty} p_A(Y)p_B(X)\,dY\,dX + \int_{0}^{B_c}\int_{A_c(X)}^{\infty} p_A(Y)p_B(X)\,dY\,dX, \tag{17}$$

where the two double integrals correspond to integrations over Regions 1 and 2, respectively, in Fig. 11. Outage due to the occurrence of A and B in Region 1 may be described as outage due only to shape or selectivity. In Region 2, outage is due to the combined effects of signal loss and selectivity.

Using eqs. (5) and (6), the integral over Region 1 is obtained as $e^{-B_c/3.8}$. The contribution due to thermal noise and shape (Region 2) is slightly more complicated. Dividing the interval 0 to B_c in Fig. 11 into N subintervals, as shown in Fig. 12, the probability of being in Region 2 is the sum of the probabilities for each subinterval. Thus eq. (17) becomes

$$P_c(\phi_i) = e^{-B_c/3.8} + \sum_{k=1}^{N} [e^{-B_{k-1}/3.8} - e^{-B_k/3.8}] P_g\left(\frac{A_k - A_0(B_k)}{5}\right), \quad (18)$$

where

$$P_g(X) = \frac{1}{\sqrt{2\pi}} \int_X^{\infty} e^{-x^2/2}\, dx. \quad (19)$$

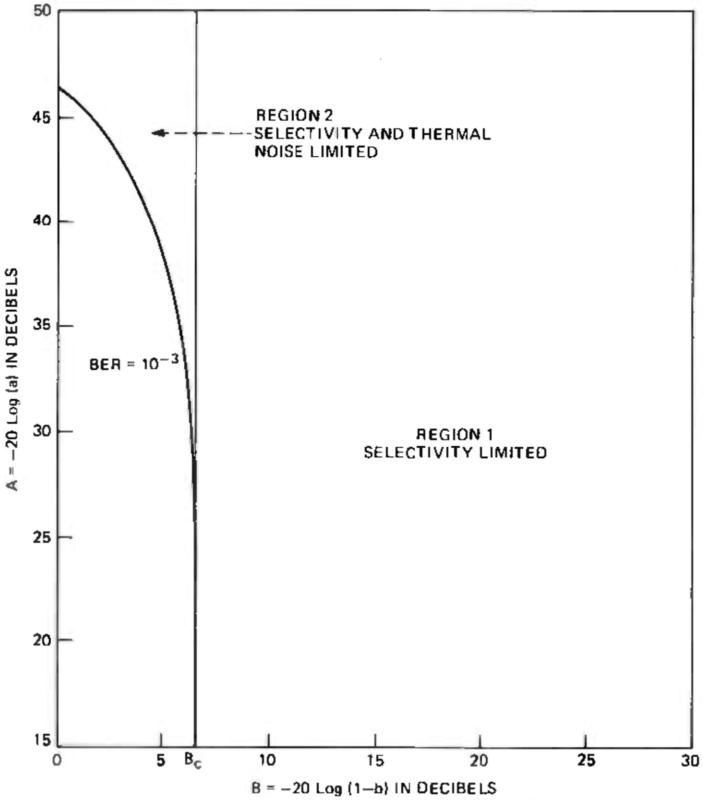

Fig. 11—Classification of outage with respect to critical curve for BER = 10^{-3}, f_0 = 19.8 MHz.

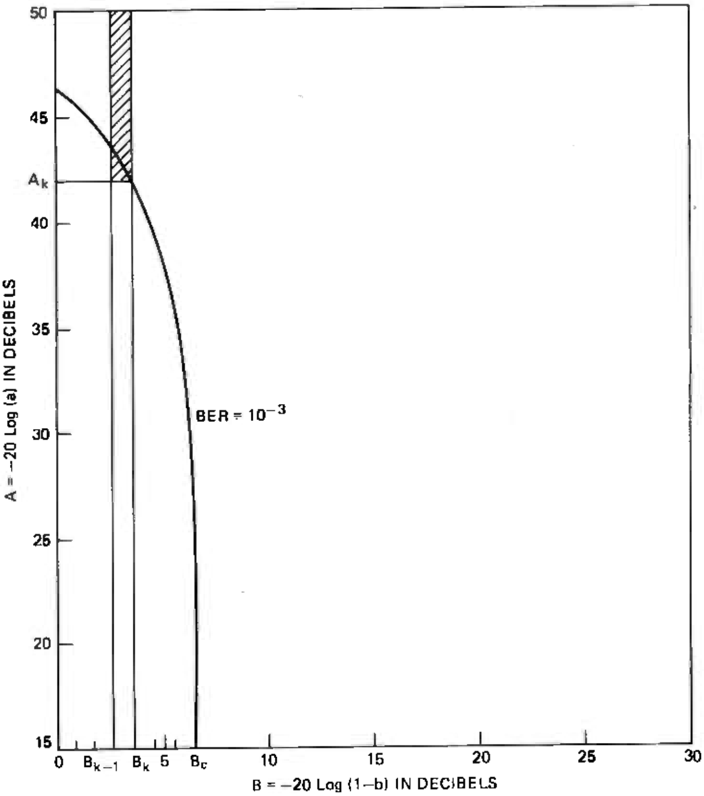

Fig. 12—Outage calculation for an incremental interval.

Evaluating the two components of eq. (18) from Fig. 11, we find

$$P_c(-45°) = 0.181 + 0.003 = 0.184. \tag{20}$$

This calculation was performed for 10 values of ϕ_i from −5 to −85 degrees in 10-degree steps. Using these results in eq. (16) and multiplying by two to account for positive values of ϕ_i which are assumed to contribute equally, we find the probability, P_o for a BER of 10^{-3} as

$$P_o = 0.0996.$$

The expected outage for the data base period is, then,

$$T_o = 5400 \times 0.0996 = 538 \text{ seconds}. \tag{21}$$

4.3 Outage calculation—selectivity only

It is apparent from eq. (20) that most of the outage for the system under study is caused by selectivity, fades characterized by A and B values in Region 1. From eqs. (14) and (17), we may express P_{os}, the probability of outage due to selectivity, as

$$P_{os} = \int_{-\pi}^{\pi} \int_{B_c}^{\infty} p_\phi(\phi) p_B(X)\, dX\, d\phi. \tag{22}$$

For the system studied for a BER of 10^{-3}, a finite B_c is obtained only for $|\phi_i| < 90$ degrees. Hence, we may use eq. (7) to simplify (22)*

$$P_{os} = \frac{2\Delta\phi}{216} \sum_{i=1}^{10} e^{-B_c(\phi_i)/3.8}. \tag{23}$$

From eq. (23) we see that the outage due only to selectivity depends on the relationship between B_c, the asymptote of critical B values, and the notch angle or notch frequency. Figure 13 shows the relationship between B_c and the notch frequency for four values of BER. It is apparent from eq. (22) that the outage probability is the probability of finding B and f_o values in the region above this curve. Such curves, therefore, provide a useful basis for evaluating the selectivity outage of a digital radio system.

4.4 Outage calculation— approximate method

For a radio system sensitive to both thermal noise and selectivity, the calculation of Section 4.3 is inadequate and that of Section 4.2 is unduly cumbersome.

To illustrate a simpler, but generally applicable, method and at the same time to provide a useful incidental result, let us evaluate the effect of reducing the transmitted power by 10 dB. For the reduced power system, the carrier-to-noise ratio would be 52 dB for the unfaded channel, and the critical curves of A and B would be shifted by 10 dB. Figure 14 shows the critical curve of A and B for a 10^{-3} BER and $f_o = -19.8$ MHz with an overplot of the conditional mean of the distribution of A. The dotted curves on Fig. 14 represent 2-sigma intervals on either side of the mean. From the properties of the Gaussian distribution, one may determine that more than 95 percent of the values of A and B will lie between these two dotted curves. We designate as A_m and B_m the coordinates of the intersection of two curves: the critical $A - B$ curve and the conditional mean curve. Then approximating the critical curve of A and B with a straight line segment tangent at (A_m, B_m), with slope s, we may approximate the probability of outage by integrating the probabilities over the region to the right of the tangent line. Using eqs. (15) and (16), we obtain

$$P_o = \Delta\phi \sum_{\text{All } \phi_i} p_\phi(\phi_i) \int_0^{\infty} \int_{A_m+s(B-B_m)}^{\infty} p_A(Y) p_B(X) dY\, dX. \tag{24}$$

---

* The factor of two is required in eq. (23) because the indicated summation corresponds to an integration only over negative notch frequencies ($\phi_i < 0$).

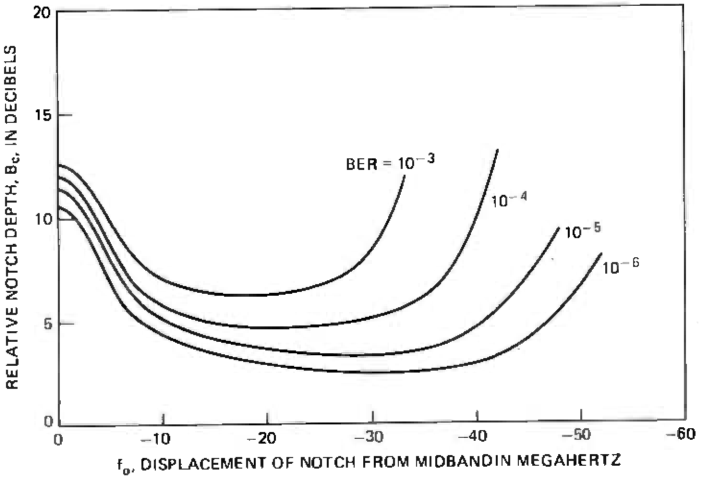

Fig. 13—Asymptotic performance curves. Locus of values of f_0 and B that produce a fixed BER at high carrier-to-noise ratio.

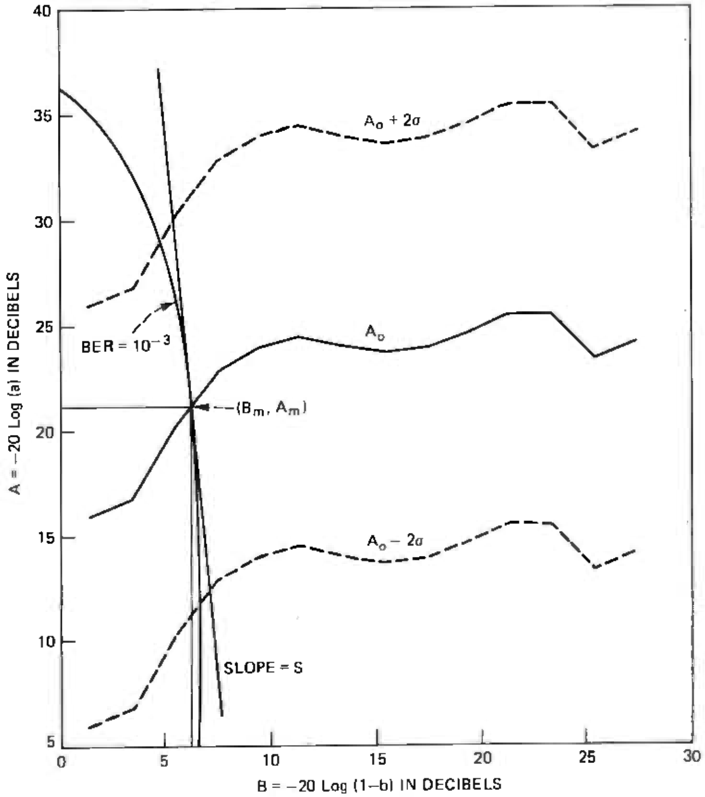

Fig. 14—Approximate outage calculation for 10 dB less transmitted signal.

Interchanging the order of integration and ignoring* the B dependence of $A_0(B)$, this becomes

$$P_o = \Delta\phi \sum_{\text{All } \phi_i} p_\phi(\phi_i) e^{-B_m/3.8} e^{0.866/s^2}. \tag{25}$$

Evaluating eq. (25) for a 10^{-3} BER and multiplying the result by 5400 gives an outage estimate for the data base period of 602 seconds. Recalculating the total outage time at a 10^{-3} BER using the method of Section 4.2 [eqs. (16) and (18)] gives 636 seconds, which verifies the accuracy of the approximate method. The estimate of 636 seconds was calculated as an upper bound; the 602 seconds calculated using (25) tend to be a lower bound. We conclude that backing off transmitted power by 10 dB would increase the outage by about 12 percent (538 to 602).

4.5 A further simplification

In this section, we show that the outage due to selectivity can be estimated approximately for a given BER from a determination of the in-band selectivity required (with the notch out-of-band) to produce that BER. Such a measurement may provide a useful approximation for any digital system using quadrature modulation components;[9] however, we provide a justification based on the performance of the system at hand. In-band selectivity is defined as the difference between the maximum and minimum attenuation present in the (25.3-MHz) channel bandwidth.

Since the in-band selectivity is a constant for any of the curves shown in Fig. 9, one can use Fig. 9 to plot the asymptotic BER against in-band selectivity for $f_o = -19.8$ MHz. Such a plot was generated for each notch position measured to produce the family of curves shown in Fig. 15. Note that, except for notch positions near the band center, the BER is uniquely related to the in-band selectivity. Neglecting the in-band notches, we find that a 10^{-3} BER corresponds to an in-band selectivity of 5.5 dB.

If we use the original model of eq. (2) to determine the values of B that will produce an in-band selectivity of 5.5 dB for a number of different notch positions, we would generate Fig. 16. It is apparent that for this system there is a good correspondence between the curves of asymptotic performance (Fig. 13) and the curves of constant in-band selectivity (Fig. 16).

To reinforce this conclusion, we provide Figs. 17, 18, and 19. Figure 17 shows the locus of in-band selectivity in a 25.3-MHz band corre-

---

* Including the effect of the slope of $A_0(B)$ at $B = B_m$ gives the same symbolic result with s interpreted as the algebraic sum of the slope of the tangent and dA_0/dB evaluated at $B = B_m$.

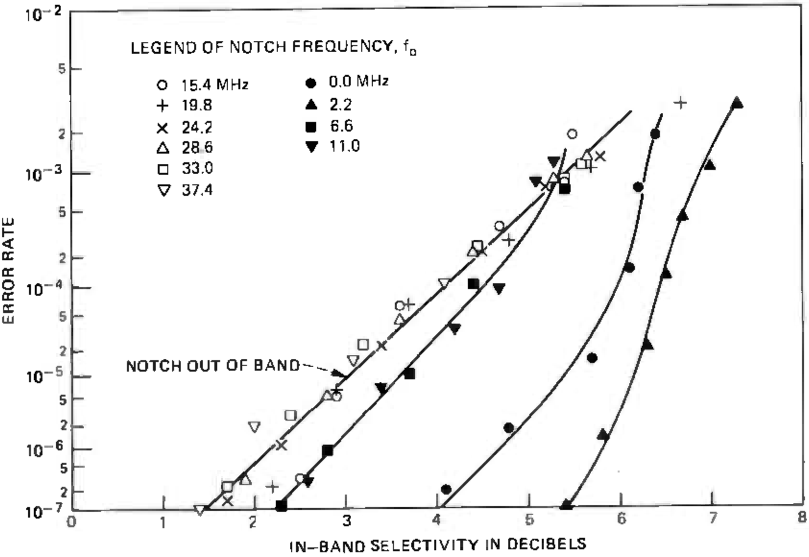

Fig. 15—Measured asymptotic bit error rate vs peak-to-peak amplitude difference in a 25.3-MHz band.

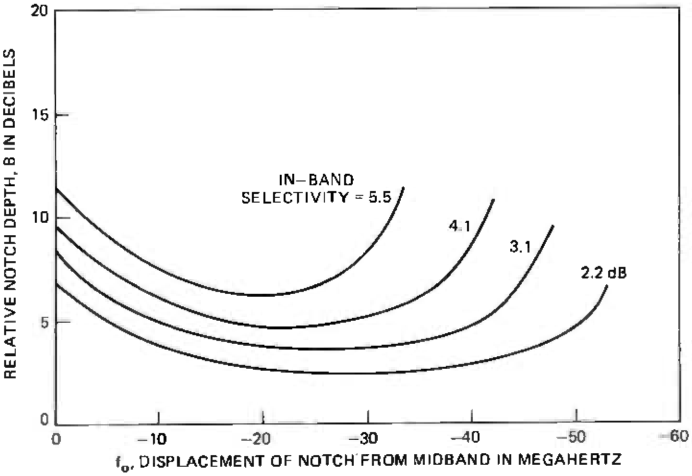

Fig. 16—Locus of B and f_o for modeled fades that have fixed peak-to-peak amplitude in a 25.3-MHz band.

sponding to each of the curves of constant BER in Fig. 13. That is, for each BER and each value of notch position, f_o, we have plotted the peak-to-peak amplitude difference in the band for the corresponding value of B_c, the asymptotic critical value of B. Figure 18 shows a similar set of curves with the peak-to-peak delay distortion in a 25.3-

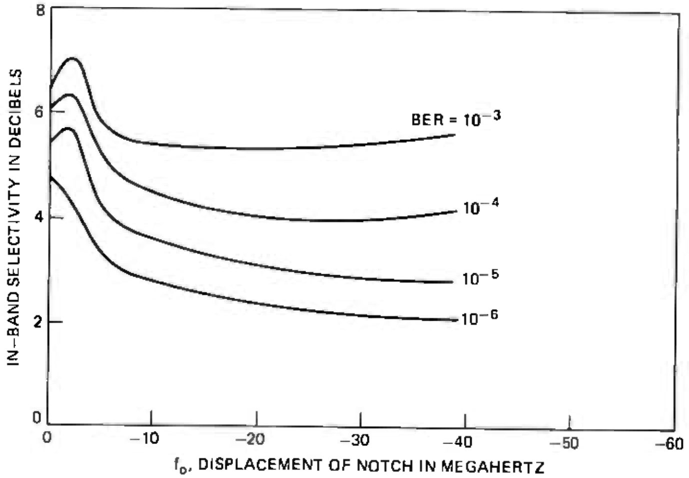

Fig. 17—In-band selectivity (in 25.3-MHz bandwidth) corresponding to asymptotic critical values of notch depth (B_c) for several values of BER.

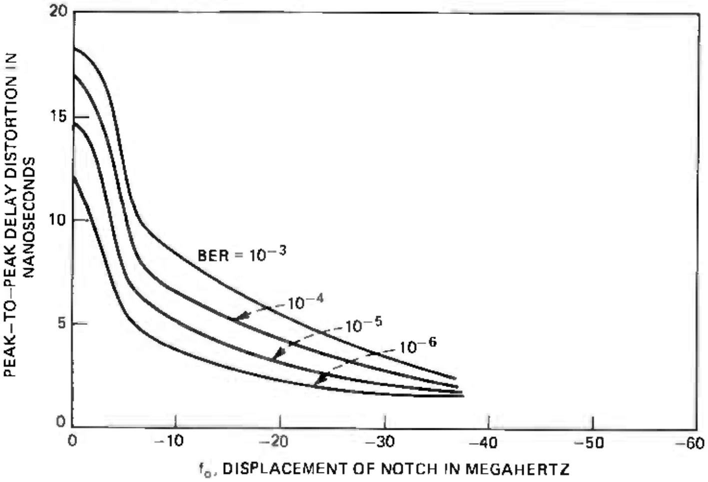

Fig. 18—Peak-to-peak envelope delay distortion in 25.3-MHz bandwidth corresponding to asymptotic critical values of notch depth (B_c) for several values of BER.

MHz band as the ordinate. Similarly, Fig. 19 has as the ordinate the "slope," or amplitude difference at a separation of 25.3 MHz. It is again clear from these three figures that the in-band selectivity is the relevant channel impairment giving rise to errors. We see from Fig. 18 that, for out-of-band notches, high BERs are obtained with very small values of peak-to-peak delay distortion, and from Fig. 19 that for in-band notches high BERs are obtained for very small values (zero at mid-band) of slope.

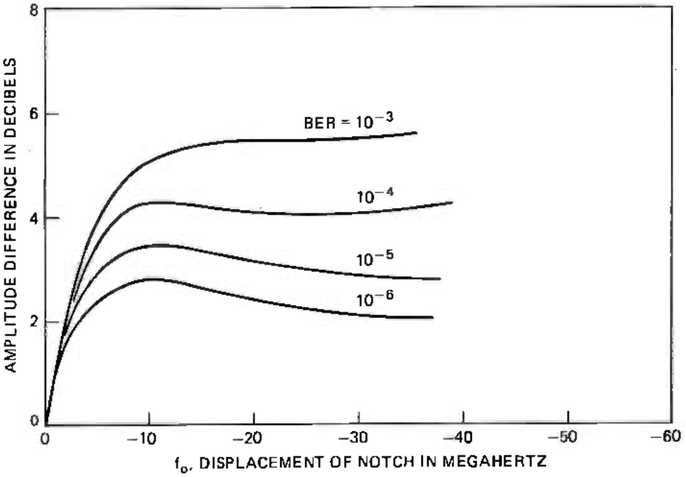

Fig. 19—Amplitude difference at a 25.3-MHz frequency separation corresponding to asymptotic critical values of notch depth (B_c) for several values of BER.

The model data base was analyzed to determine the time during which the in-band selectivity in a band of 25.3 MHz exceeded a given value. Figure 20 presents this distribution for in-band selectivity as calculated from the modeled fits. Figure 20 can be used directly in conjunction with Fig. 15 to calculate the outage times for the model data base.* For instance, from Fig. 15 we note that 5.5 dB of selectivity corresponds to a 10^{-3} BER. We use Fig. 20 to determine that 5.5 dB was exceeded for 520 seconds.

V. COMPARISONS OF CALCULATED AND OBSERVED OUTAGES

Using the methods of Sections 4.2 to 4.5, outage times were calculated for bit error rates of 10^{-3} to 10^{-6} for both the model data base period and for a heavy fading month, by multiplying the outage probabilities by 5400 and 8100, respectively.

5.1 Model data base period

Calculated and observed† outages for the model data base period are shown in Table I. In general, comparing the calculated results with observed results, we see that the outage is underestimated at high BERs and overestimated at low BERs. Any estimation procedure based on the current modeled state of the channel will tend to underestimate

---

* In practice, one would use a single measurement of in-band selectivity. For instance, in Fig. 9 one would take the 5.7-dB value corresponding to the curve asymptotic at a 10^{-3} BER.

† Because of quantization, the outage times observed from the field experiment correspond to bit error rates of 1.26×10^{-3}, 1.57×10^{-4}, 0.981×10^{-5}, and 1.19×10^{-6}.

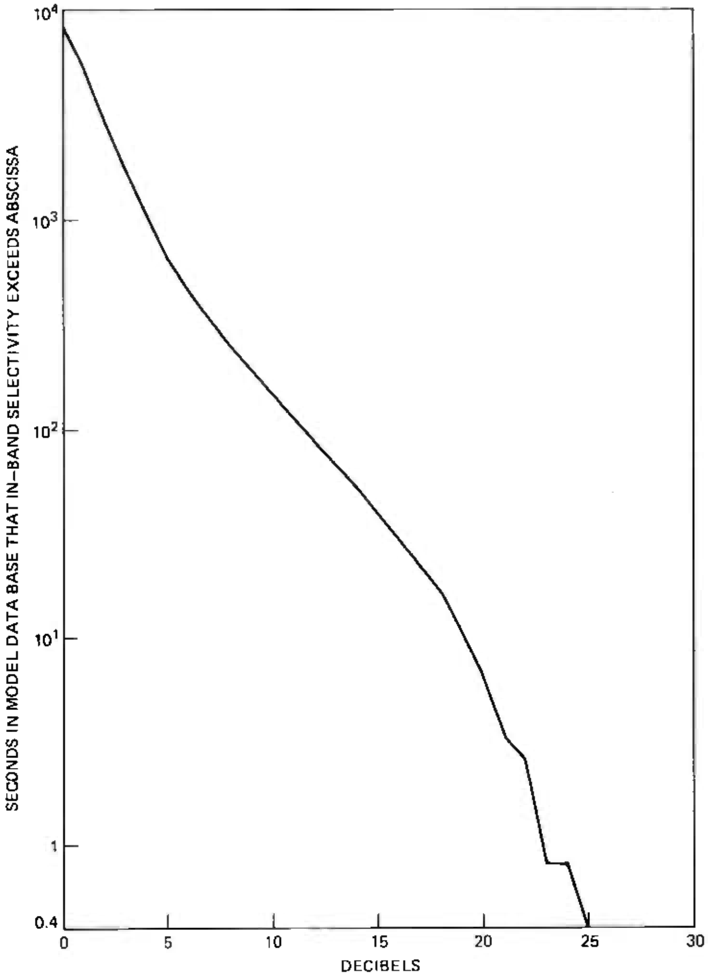

Fig. 20—Distribution of in-band selectivity (25.3-MHz bandwidth) for model data base.

Table I—Outage in modeling data base period (seconds)

BER =	10^{-3}	10^{-4}	10^{-5}	10^{-6}
Observed	636	903	1191	1487
Detailed calculation (Section 4.2)	538	960	1430	1860
Approximate calculation (Section 4.4)	527	950	1420	1830
Asymptotic calculation (Section 4.3)	527	950	1420	1830
Selectivity calculation (Section 4.5)	510	900	1570	2730

outage at high BERs because of hysteresis effects in the radio receiving equipment. That is, when the channel condition becomes sufficiently severe, the bit error rate becomes high enough (on the order of 10^{-3}) that the timing and/or phase of the radio system breaks lock. If the channel impairment becomes less severe, the BER will not improve until the system resynchronizes. The hysteresis is important at the 10^{-3} BER, since a significant fraction of the events that cause 10^{-3} BER will cause the system to break lock.

One would expect to overestimate the outage at low BERs because of the method of taking data. Recall that, in measuring the curves in Fig. 9, it was found that the BER depended on the phase to which the system had locked. The recorded performance represented the worst-phase condition. At a 10^{-6} BER, the best phase produces a BER that is about ⅓ that produced by the worst phase; the difference in BER from worst to best phase at a 10^{-3} BER is negligible. Hence, one would expect outage to be overestimated significantly at low bit error rates.

In comparing the outage calculated from in-band selectivity (Section 4.5) to the outage observed, we find that the overestimation of outage at low BERs is more severe than with the other methods. This is due to the greater sensitivity of the differential selectivity method to the bias induced by choosing the worst-case phase. For instance, comparing calculations at a 10^{-6} BER, we find that Fig. 20 is steeper for amplitude differences near 2 dB than is Fig. 3 near B values of 3.5 dB. (Figure 9 verifies the appropriateness of this comparison). More generally, one expects the method based on in-band selectivity to overestimate the outage because the method is based on notches out of band. From Fig. 15, it is apparent that, for a given ΔA, some scans will not have the BER specified.

We conclude that, although calculation of outage from sensitivity to in-band selectivity provides quick estimates, they are less accurate. The calculation requires knowledge of the distribution of in-band selectivity over a specified bandwidth. These statistics are neither simple nor generally available. It has been shown,[10] for instance, that slope statistics have a nontrivial dependence upon the measurement bandwidth.

It is clear that the calculations based on selectivity (Sections 4.3 and 4.5) agree for the system studied here because that system has very little outage due to thermal noise limitations, and because it is sensitive primarily to in-band amplitude excursions. The extent to which these statements are true for other systems is currently unknown.

5.2 Outage on a monthly basis

The results in Table I may be put on the basis of a heavy fading month by increasing them by a factor of 1.5, as discussed in Section 2.2. The resulting outages (including the scaled observed outage) are compared with the outage observed in a one-month period[8] in Table II. We see that the outage times observed in the total one-month period agree well with the values obtained by scaling the observed

Table II—Outage in a heavy fading month (seconds)

BER =	10^{-3}	10^{-4}	10^{-5}	10^{-6}
Observed (Ref. 8)	1000	1320	2100	2900
Scaled observation from Table I	955	1350	1790	2230
Calculation (Section 4.2–4.4)	800	1430	2140	2760
Selectivity calculation (Section 4.5)	770	1350	2350	4100

outage for the data base period used in modeling, except for the slight divergence appearing at low BERs. This divergence should not be unexpected for this equipment. As may be seen in Fig. 15, a 10^{-6} BER may be caused by differential amplitude selectivity in band of 2 dB. Such modest amounts of selectivity may be expected to occur sometimes in the presence of very moderate selective fading. The modeling data base was constructed by selecting only periods of significant selective fading. This reinforces the comments made in conjunction with Fig. 3, namely, that the model distribution of B represents a lower bound for small values of B which can contribute to outage at the 10^{-6} BER level.

VI. CONCLUSIONS

We have demonstrated the validity of a technique for estimating the unprotected outage of a digital radio system due to selective fading on a particular hop in the 6-GHz common carrier band. The technique required field measurements to statistically characterize the parameters of a model of propagation on the hop. It also requires performance data obtained in the laboratory for the radio system by stressing it with a two-path fade simulator with a differential path delay of 6.3 ns, corresponding to the fixed delay channel model. Since the radio path on which these measurements were made has a length close to the average for the Bell System long haul radio network and has an average incidence of fading activity, the channel model is representative of a typical path. At the very least, the technique provides a basis for determining the relative merits of various digital radio systems operating without benefit of space diversity.

For the system under test, outage was calculated by four different methods. Because this system was selectivity-limited rather than noise-limited, all four methods predicted approximately the same outage as that summarized in Table I; however, the method based on in-band selectivity is more severely biased at low BERs. The method based on asymptotic performance and that based on in-band selectivity can only be used to estimate outage due to selectivity. If the transmitted power of the system under test were reduced by 10 dB, both of the other two methods, the detailed and the approximate method, would predict an increase in outage time of about 12 percent.

VII. ACKNOWLEDGMENTS

The conclusions of this effort depend upon data collected on a 6-GHz digital radio hop installed by R. A. Hohmann and L. J. Morris, using instrumentation designed by G. A. Zimmerman. M. V. Pursley's assistance in processing the data was invaluable. Consistent laboratory data used to close the loop reflect contributions by T. J. West and G. B. Thomas to the methodology of selective fade simulation at IF, and A. E. Resch who performed the measurements.

REFERENCES

1. E. Takeuchi and P. Tobey, "A 6 GHz Radio for Telephony Applications," Conference Record ICC 1976, Vol. II, June 1976, p. 18–27.
2. P. R. Hartman and J. A. Crossett, "A 90 MBS Digital Transmission System at 11 GHz using 8 PSK Modulation," Conference Record ICC 1976, Vol. II, June 1976, p. 18–8.
3. A. J. Giger and T. L. Osborne, "3A-RDS 11 GHz Digital Radio System," Conference Record ICC 1976, Vol. II, June 1976, p. 18–1.
4. I. Godier, "DRS-8 Digital Radio for Long-Haul Transmission," Convention Record ICC 1977, Vol. 1, June 1977, p. 102.
5. W. A. H. Wood, "Modulation and Filtering Techniques for 3 Bits/Hertz Operation in the 6 GHz Frequency Band," Convention Record ICC 1977, Vol I, June 1977, p. 97.
6. W. D. Rummler, "A New Selective Fading Model: Application to Propagation Data," B.S.T.J, this issue, pp. 1037–1071.
7. W. T. Barnett, "Multipath Propagation at 4, 6, and 11 GHz," B.S.T.J., *51,* No. 2 (February 1972), pp. 321–361.
8. W. T. Barnett, "Measured Performance of a High Capacity 6 GHz Digital Radio System," Conference Record ICC 1978, Vol. III, June 1978, pp 47.4.1–47.4.6.
9. J. R. Gray and T. J. West, private communication.
10. G. M. Babler, "A Study of Frequency Selective Fading for a Microwave Line-of-Sight Narrowband Radio Channel," B.S.T.J., *51,* No. 3 (March 1972), pp. 731–757.

Contributors to This Issue

Carl W. Lundgren, E.E., 1957, M.S., 1959, and Ph.D., 1961, University of Cincinnati; U.S. Army Electronics Research and Development Laboratory, 1962–1963; Bell Laboratories, 1961—. Mr. Lundgren's early work in electrodynamics and gyro mechanics led to magnetic navigation techniques. Past work includes contributions on launch timing for optimum spin-axis orientation of Telstar, system designs for the Comstar and Iranian domestic satellite systems, millimeter-wave transmission through heavy rain, improvements to Cassegrainian earth antennas to reduce echo distortion, and frequency sharing between satellite and terrestrial systems. At present, he is studying multipath microwave transmission and interference phenomena associated with high-capacity digital radio systems. Member, Phi Eta Sigma, Eta Kappa Nu, Tau Beta Pi, Omicron Delta Kappa, AAAS, IEEE, AIAA, New York Academy of Sciences.

Dan Maydan, B.Sc. (E.E.), 1957, and M.Sc. (E.E.), 1962, Israel Institute of Technology; Ph.D. (Physics), 1965, Edinburgh University; Bell Laboratories, 1967—. Mr. Maydan has worked on acousto-optical interaction for modulating laser beams. He currently supervises a group working on X-ray lithography for the fabrication of VLSI devices and dry processing techniques. Senior Member, IEEE.

J. E. Mazo, B.S. (Physics), 1958, Massachusetts Institute of Technology; M.S. (Physics), 1960, Ph.D. (Physics), 1963, Syracuse University; Research Associate, Department of Physics, University of Indiana, 1963–1964; Bell Laboratories, 1964—. At the University of Indiana, Mr. Mazo worked on studies of scattering theory. At Bell Laboratories, he has been concerned with problems in data transmission and is now working in the Mathematical Research Center. Member, American Physical Society, IEEE.

Joseph M. Moran, B.E.E., 1965, City College of New York; M.S.E.E., 1967, and Ph.D., 1968, University of Pennsylvania; Bell Laboratories, 1968—. Mr. Moran is currently engaged in research and development of microlithography, plasma processing and device processing technologies. Member, Eta Kappa Nu, Tau Beta Pi, IEEE.

Attilio J. Rainal, University of Alaska; University of Dayton, 1950–52; B.S.E.Sc., 1956, Pennsylvania State University; M.S.E.E., 1959, Drexel University; D. Eng., 1963, Johns Hopkins University; Bell Laboratories, 1964—. Mr. Rainal's early work involved research on noise theory with application to detection, estimation, radiometry, and radar theory. He has also been engaged in the analysis of FM communication systems. His more recent work includes studies of crosstalk on multilayer boards, voltage breakdown and current-carrying capacity of printed wiring, and electromagnetic compatibility. Member, Tau Beta Pi, Eta Kappa Nu, Sigma Tau, Pi Mu Epsilon, Sigma Xi, IEEE.

William D. Rummler, B.S. in E.E., 1959, Drexel University; S.M., 1960, E.E., 1961, Sc.D., 1963, Massachusetts Institute of Technology; Bell Laboratories, 1963—. Mr. Rummler was initially concerned with radar signal design and signal processing and associated measurement and estimation problems. He has also worked on single-sideband, long-haul radio systems. More recently, he has been involved with the problems of channel and performance characterization for high-speed digital radio systems. Member, IEEE, Tau Beta Pi, Eta Kappa Nu, Sigma Xi, Phi Kappa Phi.

Papers by Bell Laboratories Authors

CHEMISTRY

Impact Strength of Polymers 2: The Effect of Cold Working and Residual Stresses in Polycarbonates. B.S. Thakkar, L.J. Broutman and S. Kalpakjian, Conference Proceedings: Society of Plastics Engineers, 36th Annual Technical Conference, *24* (April 24, 1978), pp. 295–303.

Ionizing Radiation. G.M. Wilkening, Patty's Industrial Hygiene and Toxicology General Principles, *1* (1978) pp. 441–512.

Noble Gas Compounds, 1962–1976. D.T. Hawkins, W.E. Falconer, and N. Bartlett, Plenum Press, N.Y., (1978), p. 179.

Nonionizing Radiation. G.M. Wilkening, Patty's Industrial Hygiene and Toxicology General Principles, *1* (1978), pp. 359–440.

COMPUTING

An Approach to the Selection and Control of Program Modules in Transaction Processing. A.Z. Lieberman, Proc. Natl. Conf. Info. Syst. Inform. Develop. (February, 1978), pp. 138.

Architecture of a Modular Network—The Bancs Network. K.L. Leung, Proceedings of the 17th IEEE Computer Society International Conference, (September 1978), pp. 212–220.

Data Base Subject Index. H.H. Teitelbaum and D.T. Hawkins, On Line, *2*, No. 2, (April 1978), pp. 16–21.

An Error Analysis for a Rolling Year Traffic Data Base. C.E. Johnson, IEEE Int. Conf. Commun. Conf. Rel., *1*, (June 4, 1978), pp. 5.1.1–5.1.5.

File Format for Data Exchange Between Graphic Data Bases. A.G. Gross, Proc. Fifteenth Des Automation Conf., (June 1978), pp. 54–59.

Multiple Data Base Searching: Techniques and Pitfalls. D.T. Hawkins, On Line, *2*, No. 2, (April 1978), pp. 9–15.

PL/I Language Summary. R.F. Rosin, ACM SIGPLAN History of Programming Languages Conf., (June 1, 1978), pp. 225–226.

Unconventional Uses of On-Line Retrieval Systems. D.T. Hawkins, J. Amer. Soc. Inform. Sci., *29*, No. 4, (July 1978), p. 209.

Verification and Design Aspects of True Concurrency. D.W. Mizell, Fifth Ann. ACM Symp. Princ. Prog. Lang., (Jan. 1978), pp. 171–175.

Workshop Report: The New and the Not So New. M.F. Slana and G.G. Dumas, Computer, *11*, No. 3, (March 1978) pp. 47–51.

ELECTRICAL AND ELECTRONIC ENGINEERING

An Approximate Method to Estimate an Upper Bound on the Effect of Multipath Delay Distortion on Digital Transmission. W.C. Jakes, Jr., IEEE Int. Commun. Conf. Rec., *3* (1978), pp. 47.1.1–47.1.5.

The D4 Channel Bank Codec. D.A. Spires, IEEE Trans. Circuits and Syst., *CAS-25*, (July 1978), pp. 468–475.

On the Design of Quantizers for DPCM Coders: Influence of the Subjective Testing Methodology. C.B. Rubinstein and J.O. Limb, IEEE Trans. Commun., *26*, No. 5, (May 1978), pp. 565–572.

A Digital Codec Simulation Facility. W.R. Daumer, IEEE Trans. Commun., *COM-26*, (May 1978), pp. 665–669.

Direct Polar Display of Subnanosecond Millimeter-Wave Switching Transients at 300 Mbit/s. F. Bosch and S. Cheng, IEEE Trans. Microw. Theory Tech., *MTT-26*, No. 1, (January 1978), pp. 24–27.

The Evolution of Techniques for Data Communication Over Voice-Band Channels. E.R. Kretzmer, IEEE Commun. Soc. Mag., *16*, No. 1, pp. 10–14.

A Fault Tolerant Memory for Duplex Systems. W.T. Hartwell, C.W. Hoffner, W.N. Toy, IEEE Trans. Rel., *R-27,* (June 1978), pp. 134–138.

Gaussian Power Model for Optical Fiber Splices. C.M. Miller and S.C. Mettler, Proceedings of Conference on Laser and Electrooptical Systems, (February 7, 1978), pp. 36–37.

Heat Conduction in the Cable Insulation of Force-Cooled Underground Transmission Lines. J.V. Sanders, L.R. Glicksman, W.M. Rohsenow, P. Koci, and M. Buckwcitz, PAS-97, (January–February 1978), pp. 134–139.

An Implicit Enumeration Algorithm for Sequencing Polices Applied to Telephone Switching. L.J. Ackerman, H. Luss, and R.S. Berkowitz, IEEE Trans. Syst. Man. Cybern., *8* (April 1978), pp. 296–300.

LAMPAC-A High Density Printed Wiring Board for General Application. V. L. Brown, Proc. First Printed World Conv. Ckt., London, England, *1* (June 5, 1978), pp. 24.1–24.15.

Microprocessors in Telecommunication Systems. D.C. Stanzione, Proc. IEEE, *66,* No. 2, (February 1978), pp. 192–199.

Multiparameter Multiport Sensitivity Measure. M.J. Chien, 1978 IEEE Int. Symp. Ckts. Syst., New York, (May 17, 1978), pp. 1040–1045.

Statistical Modeling for Circuit Design. E.M. Butler, Conference Record of Electro/78, *5* (May 23, 1978), pp. 1–5.

Sufficient Criteria for PCIR Stability in Linear 2-Port Networks in Terms of Qualitative Data. J.D. Williams and N.N. Puni, 1978 IEEE International Symposium on Circuits and Systems Proceedings, *78CH135-1, CAS* (May 1978), pp. 638–641.

MECHANICAL AND CIVIL ENGINEERING

Experimental and Analytical Investigation of Self-Excited Chatter Vibrations in Metal Cutting. N. Saravanja-Fabris and A.F. D'Souza, J. Mech. Des., *100* (January 1978), pp. 92–99.

PHYSICS

Calculation of Per-Unit-Volume RF Scattering Cross Sections in the Radar Aurora. J. Minkoff, Can. J. Phys., *56* (February 1978), pp. 280–287.

Calorimetric Measurements of Absorption and Scattering Losses in Optical Fibers. F.T. Stone, W.B. Gardner, and C.R. Lovelace, Opt. Lett., *2* (Feburary 1978), pp. 48–50.

CCITT No. 6 (And Other) Common Channel Signaling Systems. Network Management Signals. J.S. Ryan, Conference Record Sem. Tele. Switch. Signal. Tech., Singapore, (April 17–28 1978), pp. 9-1–9-13.

Comparison of Cyclofusion in Central and Peripheral Vision. M.T. Sullivan and A.E. Kertesz, Proc. Ann. Conf. Assn. Res. Vision Opthal. Mol., Sarasota, Florida, (April 1978), p. 140.

Digital Transmission Network Maintenance Aspects. W. Bleickardt, Proc. Ann. Rel. Maintain. Symp., Los Angeles, Calif., IEEE Catalog No. *77CH1308-6R,* (January 17–19, 1978), pp. 460–464.

A Guide to Conduit Selection. J.W. Peters, Tel. Eng. Manage., (September 1, 1978), pp. 116–121.

Measured Performance of a High Capacity 6GHz Digital Radio System. W.T. Barnett, ICC '78 Conference Record, *3* (June 4–7, 1978), pp. 47.4.1–47.4.6.

Mechanized Activity Tracking and Fill Monitoring in the Loop Plant. G.W. Aughenbaugh and N.H. Noe, The International Symposium on Subscriber Loops and Services, (1978), pp. 85–89.

On-Line Information Retrieval Bibliography. D.T. Hawkins, On-Line Review, *2* (1978), pp. 63–106.

Plant Engineering in a Phone Center Environment. R. Sherman, Proceedings of International Symposium on Subscriber Loops and Services, (March 1978), pp. 90–93.

The Reflections of a Former High Energy Physicist Doing Industrial Applied Mathematics. R.A. Mercer, Proc. 39th A.I.P. Conference, American Institute of Physics, New York, N.Y., (1978), pp. 193–196.

Results of an Experiment to Detect for Field-Normal Plasma Line Scattering in the Auroral Ionsphere. J. Minkoff, M. Laviola, R. Tsunoda, and R. Presnell, Radio Sci., *13,* No. 3, (1978), pp. 577–580.

The Role of the ITU and CCITT in Telecommunications. J.S. Ryan, Commun. Trans. Tech. Switch. Syst. Sem, Princeton, Univ., (March 20, 1978), pp. 2-1–2-6.

Spectrum Management in the Loop Plant. R.K. Even, J. Kreutzberg, G. Miller, and L.M. Smith, The International Symposium on Subscriber Loops and Services, (February 1978), pp. 234–238.

A Study of the Effects of Mobile Telephone Use on Driving Behavior. A.J. Kames, 28th IEEE Veh. Technol. Conf., Denver, Colorado, *78CH1297-IVT,* (March 22–24, 1978), p. 537.

Two Conferences Address Local Digital Switching and Transmission in Zurich and Atlanta. R.W. Wyndrum, Jr., Communications Society Magazine, *16* (July 1978), p. 23–24.

Underwater Sound Arrival Angle Estimation by Multiple Cross Correlation Measurements. H.J. Young, IEEE International Conference on Acoustics, Speech & Signal Processing Record, (April 10–12, 1978), pp. 659–664.

SYSTEMS ENGINEERING AND OPERATIONS RESEARCH

The Output of Multiserver Queuing Systems. C.D. Pack, Oper. Res. *26* (May–June 1978), pp. 492–509.

Copyright © 1979 American Telephone and Telegraph Company
THE BELL SYSTEM TECHNICAL JOURNAL
Vol. 58, No. 5, May–June 1979
Printed in U.S.A.

B.S.T.J. BRIEF

A Counterexample to a Conjecture on the Blocking Probabilities of Linear Graphs

by H.W. BERKOWITZ

(Manuscript received November 21, 1978)

It was conjectured by Chung and Hwang that a series-parallel regular linear graph is superior to another if its degree sequence majorizes the degree sequence of the other. A counterexample to this conjecture is given.

The following definitions are taken from Refs. 1 and 2. Consider a t-stage linear graph with a source (the vertex of the first stage) and a sink (the vertex of the last stage). All the vertices are arranged in a sequence of stages such that, for each edge, one vertex is in stage i and the other vertex is in stage $i + 1$, for some i. Each edge is in one of two states, *busy* or *idle.* A linear graph is *blocked* if every path joining the source and the sink contains a busy edge. Assume that any edge connecting a vertex in stage i with a vertex in stage $i + 1$ has probability p_i of being busy for $1 \leq i \leq t - 1$. For a t-stage linear graph, the sequence $(p_1, p_2, \cdots, p_{t-1})$ is called the *link occupancies* for that graph. One t-stage linear graph is *superior* to another if, for any given link occupancies, the blocking probability of the first graph does not exceed that of the second.

Let e be an edge from a vertex a in stage i to a vertex b in stage $i + 1$. Define $\lambda(e)$ to be the ratio of the outdegree of a to the indegree of b. A t-stage linear graph is *regular* if, for each i, $1 \leq i \leq t - 1$, if e and f are any two edges between stage i and stage $i + 1$, than $\lambda(e) = \lambda(f)$. In this case, let $\lambda_i = \lambda(e)$. Thus a regular linear graph is associated with a unique degree sequence $(\lambda_1, \lambda_2, \cdots, \lambda_{t-1})$.

A degree sequence $(\lambda_1, \lambda_2, \cdots, \lambda_{t-1})$ *majorizes* another degree sequence $(\lambda_1', \lambda_2', \cdots, \lambda_{t-1}')$ if and only if $\lambda_1\lambda_2 \cdots \lambda_i \geq \lambda_1'\lambda_2' \cdots \lambda_i'$ for every i, $1 \leq i \leq t - 1$.

A *series-parallel* regular linear graph is a regular linear graph which is either a series combination or a parallel combination of two smaller series-parallel regular linear graphs with an edge being the smallest such graph.

I. A COUNTEREXAMPLE

In Ref. 2, Chung and Hwang conjectured that one series-parallel regular linear graph is superior to another if the degree sequence of the first majorizes the degree sequence of the second.

The graphs of Fig. 1 are a counterexample to this conjecture. The degree sequence of graph (a) is (2, 1, 1, 1/2), the degree sequence of graph (b) is (2, 1/2, 2, 1/2). Thus, the degree sequence of graph (a) majorizes the degree sequence of graph (b).

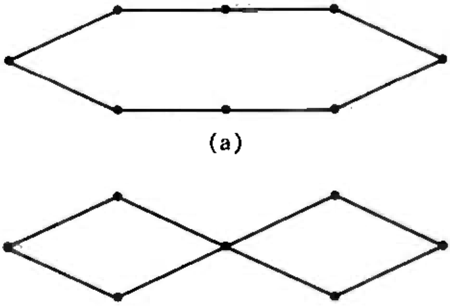

(a)

(b)

Fig. 1—Counterexample.

Let (p_1, p_2, p_3, p_4) be the link occupancies of the two graphs. Let $q_i = 1 - p_i$, for $1 \le i \le 4$. Then the blocking probability of graph (a) is $A = (1 - q_1q_2q_3q_4)^2$. The blocking probability of graph (b) is $B = (p_1 + p_2 - p_1p_2)^2 + (p_3 + p_4 - p_3p_4)^2 - (p_1 + p_2 - p_1p_2)^2(p_3 + p_4 - p_3p_4)^2$. Now let $p_i = 0.1$, for $1 \le i \le 4$. Then $A = (1 - (0.9)^4)^2 = (1 - 0.6551)^2 > (1 - 0.7)^2 = 0.09$. But $B = 2(0.19)^2 - (0.19)^4 < 2(0.2)^2 = 0.08$. Thus for this set of p_i's, the blocking probability of graph (b) is less than that of graph (a); so graph (a) is not superior to graph (b), contradicting the conjecture.

II. ACKNOWLEDGMENTS

The author would like to thank the referee for his helpful suggestions and for noting that graphs (a) and (b) permit 2 paths and 4 paths, respectively, between terminals. Because of this, they are not really alternative choices of linking patterns for a fixed network with given switch sites and number of stages. If the restriction "total paths = constant" is maintained, the original conjecture may well be true.

REFERENCES

1. F.R.K. Chung and F.K. Hwang, "A Generalization of Takkagi's Theorem on Optimal Channel Graphs," B.S.T.J., *57,* No. 1 (January 1978), pp. 171–178.
2. F.R.K. Chung and F.K. Hwang, "On Blocking Probabilities for a Class of Linear Graphs," B.S.T.J., *57,* No. 8 (October 1978), pp. 2915–2925.